Noise from a Rotor Ingesting Inhomogeneous Turbulence

David Martin Wisda

Thesis submitted to the faculty of the Virginia Polytechnic Institute and State University in partial fulfillment of the requirements for the degree of

Master of Science

In

Aerospace Engineering

William Devenport

Willam Nathan Alexander

Todd Lowe

April 21st, 2015

Blacksburg, Virginia

Keywords: Rotor, Acoustics, Boundary Layer, Ingestion Noise, Experimental, Microphone, Hot Wire Anemometry, Anechoic, Wind Tunnel, Virginia Tech

Noise from a Rotor Ingesting Inhomogeneous Turbulence

David Martin Wisda

On-blade hot wire anemometry measurements as well as far field sound measurements at several receiving angles have been previously made for a rotor partially embedded in a boundary layer. The inflow distortion effect on the rotor angle of attack distribution was determined directly from the on-blade measurements, and was found to minimally affect the angle of attack at the blade tips and lower the angle attack in the rotor disk plane as the radial location moves towards the hub. A narrow, sharp increase in angle of attack as the rotor blades approached the wall was also observed, indicating blade interaction with flow reversal. The haystacking pattern, or spectral humps that appear at multiples of the blade passage frequency, was studied for a wide range of advance ratios. At high advance ratios, evidence of vortex shedding from the blade trailing edges was observed. For low advance ratios, the haystacks narrowed, became more symmetric and increased in number. A method of determining the average acoustic signature of an eddy passage through a rotor was developed from time delay aligning multiple microphone signals and eddy passages detected using the continuous wavelet transform. It was found that the eddy passage signatures were similar to a cosine wave with a Gaussian window. It was also found that normalized timescales obtained directly from the eddy passage signatures remained somewhat constant with advance ratio, but increases slightly for fixed free stream velocities with increasing rotor RPM. For advance ratios less than 0.6, the eddy passage signatures were dominated by a tonal component due to rotor ingestion of misaligned flow caused by a boundary layer separation at the wall. This indicates that flow reversal known as the “Pirouette Effect” is interacting with the rotor blades.

Acknowledgements

I would like to thank my advisor Dr William Devenport for the guidance and support that he has offered towards this project. The analysis presented in this thesis would not have been possible had it not been for his continuous motivation and insight.

I would also like to thank Dr William Nathan Alexander for his assistance. Much of the analysis presented is based off of prior measurements and analysis done by him. He was the main person who brought me up to speed on the rotor project when I started graduate school at Virginia Tech and taught me the majority of the relevant physics studied in this analysis.

I would like to that the Office of Naval Research, in particular Dr Ki-Han Kim and Dr John Muench, for their insight and support under grants N00014-10-1-0908 and N00014-14-1-0141.

I would like to thank my fiancé, Kristen, for her constant support throughout my time here at Virginia Tech. She has made it possible to focus on my work and has put up with me spending most of my time at school instead of with her.

I would like to thank everyone in my research group and CREATe including Liselle Joseph, Manuj Awasthi, Ian Clark, Ken Brown, Henry Murray, Tyler Englerth, Alex Schneider, Tobias Ecker, Dan Cadel, and Brian Petrosky for helping me with my research and coursework, and also for creating a fun work environment to be a part of every day.

I finally would like to thank all of my friends for making graduate school as memorable as possible. I would have probably graduated much earlier and with better grades if it wasn't for all of you.

CONTENTS

1 Introduction 1
1.1 Motivation 1
1.2 Literature Review 1
1.3 Study Goals 7
2 The Experimental Setup of Alexander *et al.* 2013 and 2014 9
2.1 Wind Tunnel 9
2.1.1 Anechoic Test Section Configuration 10
2.2 Rotor System 13
2.2.1 Rotor Performance Analysis with JavaProp 17
2.3 Boundary Layer Characterization 18
2.4 On-Blade Hotwire Measurement System 19
2.5 Microphone Measurement System 20
2.6 Test Matrixes 23
2.6.1 Acoustic Measurements 23
2.6.2 Hotwire Measurements 24
3 Results and Discussion 26
3.1 Inflow Distortion As Seen by The Rotor Blades 26
3.1.1 Undistorted Angle of Attack Distribution Seen by the Rotor Blades 26
3.1.2 Measured Angle of Attack Distributions Seen by the Rotor Blades 29
3.2 Time Averaged Rotor Sound Field 35
3.3 Characteristics of the Turbulence as Revealed in the Sound Field 47
3.3.1 Identifying eddy ingestion events in the acoustic signals 50
3.3.2 Averaging the ingestion event acoustic signals 56
3.3.3 Determination of average eddy scales 70
4 Conclusions 72
References 75

List of Figures

Figure 1: Virginia Tech Stability Wind Tunnel layout 9
Figure 2: Virginia Tech Stability Wind Tunnel acoustic treatments 10
Figure 3: Semi-anechoic test section configuration 11
Figure 4: Diagram of the semi-anechoic test section configuration used for this study 11
Figure 5: Semi-anechoic configuration modified contraction 12
Figure 6: Top down view diagram of test section with contraction and trip strip modifications (Note coordinate system is defined centered on the rotor disk plane with +z being out of the page) 13
Figure 7: Rotor in its acoustic test configuration 15
Figure 8: Rotor mounting system 16
Figure 9: Rotor with blades removed in its background noise configuration 16
Figure 10: Laser-photodiode system 17
Figure 11: Rotor thrust coefficient curve 18
Figure 12: Close-up view of the quadwire used for boundary layer measurements 19
Figure 13: Blade-mounted hotwire probe locations 20
Figure 14: Test section with inflow microphone configuration 21
Figure 15: B&K inflow microphone with bullet nose cone 21
Figure 16: B&K port chamber microphones 22
Figure 17: Undistorted angle of attack distribution as seen by the rotor chord line (20 m/s, 2500 RPM, J=1.05) 27
Figure 18: Undistorted angle of attack distribution as seen by the rotor chord line (20 m/s, 1823 RPM, J=1.44) 28
Figure 19: The angle of attack as seen by the rotor blade distribution in the outer 20% of the blade radius obtained from A) measured hotwire data, and B) undistorted flow analysis (J = 1.05, 2500 RPM, U_∞ = 20 m/s) 30
Figure 20: The angle of attack as seen by the rotor blade distribution in the outer 20% of the blade radius obtained from A) measured hotwire data, and B) undistorted flow analysis (J = 1.44, 1823 RPM, U_∞ = 20 m/s) 30
Figure 21: Angle of attack distributions for the rotor at 20 m/s, 2500 RPM, and J = 1.05 at A) 80% blade radius, and B) 98.5% blade radius 31
Figure 22: Angle of attack distributions for the rotor at 20 m/s, 1823 RPM, and J = 1.44 at A) 80% blade radius, and B) 98.5% blade radius 32
Figure 23: Angle of attack distributions for the rotor at 15 m/s, 2500 RPM, and J = 0.79 at A) 80% blade radius, and B) 98.5% blade radius 34
Figure 24: Angle of attack distributions for the rotor at 10 m/s, 2500 RPM, and J = 0.53 at A) 80% blade radius, and B) 98.5% blade radius 34
Figure 25: Rotor noise at U_∞ = 20m/s for various advance ratios J a) compared to background noise b) and normalized on the tip velocity and BPF 36
Figure 26: Rotor noise at U_∞ = 20m/s for various advance ratios J normalized on the tip velocity and BPF and plotted on a linear x-axis to better view asymmetry about the 1st BPF. 37
Figure 27: Diagram of explanation of right-skewed haystack at high advance ratios 38

Figure 28: True dipole sound source directivity 39
Figure 29: Complex reflected dipole sound propagation diagram..... 39
Figure 30: Predicted wall included attenuations due to directivity at A) 15°, B) 29°, and C) 53°41
Figure 31: Directivity of noise at a) J=1.44, b) J=0.72, c) and J=0.44 42
Figure 32: Expected directivity attenuation of from a broadband 55 dB dipole source with wall effects 43
Figure 33: Contour of noise spectra over a range of advance ratios at fixed RPM of 2734 and varying inflow speed (measured at 53°) 44
Figure 34: Combined contours of noise spectra over a range of advance ratios at fixed inflow velocities and varying RPM normalized on tip velocity for the 101 mm boundary layer (measured at 53°)..... 45
Figure 35: Coherence of acoustic signal at a 53° receiving angle with the blade clocking signal at the BPF..... 46
Figure 36: Coherence of acoustic signal at a 53° receiving angle with the blade clocking signal at the BPF plotted against Sato *et al.* (1986)'s thrust parameter. 47
Figure 37: Time series of noise showing bursts as coherent structures are cut by successive blades (30 m/s, 4000 RPM, J = 0.98, $\theta m = 14o$) 48
Figure 38: Diagram of acoustic path change through a shear layer (Notation from Amiet (1978)) 49
Figure 39: Measured and predicted full signal time delays of microphones 3 and 4 with microphone 5 50
Figure 40: Short-Time Fourier Transform of acoustic signal ($U\infty = 30m/s$, 4000 RPM, BPF = 667 Hz)..... 51
Figure 41: Continuous Wavelet Transform of acoustic signal $U\infty = 30m/s$, 4000 RPM, BPF = 667 Hz)..... 52
Figure 42: BPF traces of continuous wavelet transform and short time Fourier transform of acoustic signal ($U\infty = 30m/s$ and 4000 RPM)..... 53
Figure 43: BPF trace of continuous wavelet transform and short time Fourier transform of acoustic signal with sources of non-smooth eddy quantification identified ($U\infty = 30m/s$ and 4000 RPM) 54
Figure 44: Effects of discrimination level on a) Number of eddies detected, b) Total time of eddy passage, and c) Elasticity of number of eddies detected with total time of eddy passage. (30 m/s, 4000 RPM)..... 55
Figure 45: Effects of discrimination level on a) Number of eddies detected, b) Total time of eddy passage, and c) Elasticity of number of eddies detected with total time of eddy passage. (20 m/s, 3500 RPM)..... 55
Figure 46: Typical deviation of differences in individual eddy arrival times of microphone 5 and microphone 8 for U=20 m/s and RPM = 4000 over a 4 second interval. 57
Figure 47: Phase averaged eddy passage acoustic signatures for 30, 20 and 10 m/s at advance ratios of 1.57 to 0.33. 58
Figure 48: Comparison of a cosine wave with a Gaussian decay to the average eddy passage signature for $U\infty = 30\ m/s$, $RPM = 4000$, and J = 0.98..... 58

Figure 49: Acoustic pressure time series for $U\infty = 10\ m/s$, $RPM = 2750$, J = 0.48, showing a dominant signal component at the BPF. (Taken at $\theta m = 14o$) 59
Figure 50: Diagram of turbulence as it is ingested by a non-thrusting rotor 60
Figure 51: Tuft flow visualization for a 30 *m/s* 2734 RPM, J=1.44 condition (Photo taken during study of Alexander *et al.* (2014)) 61
Figure 52: PIV Velocity vector field for a 20 *m/s*, 1823 RPM, J=1.44 condition (PIV measurement obtained in studies of Wisda *et al.* (2015) and Murray *et al.* (2015) 62
Figure 53: Phased average acoustic signature for a 30 *m/s*, 2734 RPM, J=1.44 condition..... 63
Figure 54: Diagram of turbulence as it is ingested by a lightly thrusting rotor 63
Figure 55: Tuft flow visualization for a 22 *m/s* 2734 RPM, J=1.05 condition (Photo taken during study of Alexander *et al.* (2014)) 64
Figure 56: PIV Velocity vector field for a 20 *m/s*, 2500 RPM, J=1.054 condition (PIV measurement obtained in studies of Wisda *et al.* (2015) and Murray *et al.* (2015)..... 65
Figure 57: Phased average acoustic signature for a 20 *m/s*, 2500 RPM, J=1.05 condition..... 66
Figure 58: Diagram of turbulence as it is ingested by a heavily thrusting rotor with flow reversal 66
Figure 59: Tuft flow visualization for a 12 *m/s* 2734 RPM, J=0.58 condition (Photo taken during study of Alexander *et al.* (2014)) 67
Figure 60: PIV Velocity vector field for a 20 *m/s*, 4500 RPM, J=0.58 condition (PIV measurement obtained in studies of Wisda *et al.* (2015) and Murray *et al.* (2015) 68
Figure 61: Diagram of arch vortex flow reversal found in Glegg *et al.* (2015)..... 69
Figure 62: Phased average acoustic signature for a 20 *m/s*, 4500 RPM, J=0.58 condition 69
Figure 63: Streamwise scales obtained directly from average eddy passage signatures for varying advance ratios and free stream velocities, compared to scales obtained in Alexander *et al*. (2013) 70

List of Tables

Table 1: Blade twist angle distribution 14
Table 2: Boundary layer characteristics measured by Alexander *et al.* (2013) 19
Table 3: Microphone measurement locations (Green: Chamber Mics, Blue: Inflow Mics)..... 22
Table 4: Sound measurements at a constant 2734 RPM..... 23
Table 5: Acoustic test matrix for 10, 15, 20, and 30 m/s flow speeds (Note advance ratios are shown)..... 24
Table 6: On-blade hotwire configurations 25
Table 7: On-blade hotwire test matrix for 10, 15, 20, and 30 m/s flow speeds (Note advance ratios are shown)..... 25

1 INTRODUCTION

1.1 MOTIVATION

Rotor turbulence interactions occur frequently and have many adverse effects; key amongst them being acoustic. When a rotor ingests turbulence, the inflow turbulence structures are distorted. The turbulent eddies are stretched into long thin elements, which are cut by successive rotor blades. This creates a distinct unsteady lift spectra which results in a dominant produced noise referred to as "haystacking." Turbulence ingestion can occur from ingestion of a wake created from a wing as well as ingestion of atmospheric turbulence. One of the most common cases of turbulence ingestion occurs when a rotor ingests a boundary layer. Jet engines ingest the boundary layer grown on the engine cowling, and any rear mounted propulsor such as a rear mounted aircraft engine or a conventionally placed marine propulsor, ingests turbulence generated from the vehicle body they provide thrust for. Many hybrid wing-body concept planes are being designed such that multiple engines are rear mounted on the top of the aircraft. This will result in the ingestion of a boundary layer grown over the entire top of the aircraft.

Every single vehicle that ingests turbulence can be improved upon by reducing noise generated by rotor-turbulence interactions. This can only be done by obtaining a more exact understanding behind the physics of the sound generated from these interactions.

1.2 LITERATURE REVIEW

Haystacking is broadband noise appearing at a rotor's blade passage frequency and its harmonics caused by coherent cutting of turbulence structures by multiple blades. Haystacking was first observed by Sevik (1971) when studying noise from the ingestion of turbulence created from an upstream grid in the four foot water tunnel of the Ordnance Research Laboratory at Pennsylvania State University. Sevik used a 10 bladed square tip rotor with a constant chord length of one inch and a diameter of eight inches. Two different turbulence grids were placed upstream of the rotor. They were constructed of 0.75 and 0.875 diameter rods with respective solidities of 0.34 and 0.27. A custom balance made from a piezo-electric crystal mounted at the end of the propeller shaft was used to measure the unsteady thrust. This balance was made to minimize error created by the bending distortions of the shaft. Thrust spectra predictions made assuming isotropic homogeneous turbulence were compared to measured thrust spectra. Sevik then presented predictions of the broadband noise produced by the rotor that depended on the turbulence integral length scale normalized on axial flow velocity, acoustic wavelength, rotor radius, and blade chord. These predictions somewhat matched measured sound levels but did not account for the blade-to-blade coherent response to the turbulence. His theory did not show the broadband spectral humps,

or haystacks, at the blade passage frequency and its harmonics, which dominate the spectra. These haystacks were found to be under predicted by about 15 dB at moderate advance ratios.

Predictions of rotor response to turbulence ingestion slowly started to account for turbulent scales large enough to cause blade to blade correlated responses. Blake (1984) further examined the haystacking phenomena by accounting for this. He allowed for an axial correlation lengths to exceed the blade spacing, allowing for multiple blades interacting with turbulent structures. His results seem to over predict the haystacking noise. Martinez (1997) attributes this to Blake (1984) deriving his blade loading in Cartesian coordinates and then applying it to a cylindrical geometry, which resulted in neglecting noise cancellation. Martinez (1997) further analyzed blade to blade interactions. He showed that the spectra of the random force acting on the rotor depends on the derivative of the inline correlation function. He showed resulting spectra for several correlation functions including standard semi-empirical and several Gaussian forms. The resulting spectra from the standard semi-empirical inline correlation function clearly showed a haystacking structure, and the haystacking feature becomes more pronounced on the wider Gaussian models. The wider correlation functions allowed for the prediction of correlated blade to blade interactions with the turbulence, resulting in a more distinct haystacking pattern.

The effect of modeling the turbulence as anisotropic was however, not incorporated into predictions yet. It was known from Hanson (1974) that incoming turbulence can exhibit extreme anisotropy. Hanson (1974) took cross wire measurements in an inlet turbulence test facility which consists of an inlet shroud and a centerbody. The flow distortion was achieved through a suction source connected to the inlet by an 18.3 m pipe. It was found that the inlet distorts the atmospheric turbulence to an integral length scale of up to 100 inlet diameters with anisotropy as high as 400:1.

Glegg & Walker (1999) investigated modeling the turbulence as anisotropic by analyzing the effects of stochastic incident gusts on rotating blades. A linear cascade model was used to approximate a fan in a cylindrical duct. This model corresponded to an unwrapped rotor and had hard wall boundary conditions. The rotor blades were modeled as flat plates. The main advantage to using a rectilinear model to approximate the cylindrical flow is the inclusion of all spanwise coupling effects. The incident turbulence was modeled as anisotropic, and it was shown that noise at blade frequency harmonics was more probable for eddies stretched in the streamwise direction. Using turbulence length scales based on measurements, as well as assumed anisotropy of 10:1 in the stream wise direction, predictions matched well with measured spectra. An important note is that spectral humps were visible even for small length scales as long as the turbulence was modeled with high anisotropy.

With the knowledge that haystacking noise is attributed to turbulence scales that are anisotropic and large enough to cause blade-to-blade correlated responses, studies started to obtain turbulence statistics directly using hot wire anemometry. This allowed for more accurate turbulent scales, instead of estimations, to be used. This was done in a study by Stephens and Morris (2008)

that studied the noise created by a fan ingesting a turbulent casing boundary layer. The rotor from Sevik's (1971) study was placed in a 1.4 m long, 0.206 m diameter PVC duct. This resulted in a tip gap of 5% rotor blade chord. The entire rotor-duct system was placed on a vibration isolation pad and in a chamber anechoic to 100 Hz. Self-noise measurements were taken with the rotor positioned near the entrance to the duct to minimize boundary layer effects and to make sure that the flow is steady and axisymmetric. To measure the acoustic response of the rotor boundary layer interactions, the rotor was moved further into the duct where the boundary layer was fully turbulent. Acoustic measurements were made and rotor self-noise was then subtracted to obtain the rotor-boundary layer acoustic response. The rotor was then removed and two–point cross correlation measurements were made of the axial velocity. The fully four-dimensional correlation function was extrapolated from these measurements by assuming an exponential decay in the autocorrelation in the cross-stream directions. Noise predictions were made using this extrapolated two-point turbulence correlation function. These predictions did not include rotor flow distortion, but were able to predict the haystacking response. They accurately predicted the haystacking shape and the peak magnitude decay. However, the actual peak magnitudes were under predicted. The authors attribute this to the inaccuracies created in extrapolating their four-dimensional correlation function from only axial velocity measurements, but it could also be due to under predicting the eddy length by neglecting distortion.

Another study by Catlett *et al.* (2012) also directly obtained turbulence statistics to improve rotor turbulence interaction predictions. Catlett *et al.* (2012) investigated the thrust and acoustic response to a rotor ingesting a spatially inhomogeneous, sheared, fully turbulent flow. A 292 mm diameter, 7 bladed propeller was attached to the trailing edge of an altered 3.05 m chord NACA 0029 airfoil spanning 2.44 m in the Naval Surface Warfare Center Carderock Division Anechoic Flow Facility. This facility is a closed circuit wind tunnel with a 2.44 m diameter, octagonal, closed test section. The test section opens to an anechoic chamber ideal for acoustic measurements. The rotor blades had rounded tips, had a maximum chord length of 4.3 cm at 65% blade radius, and pitched from 24.1 degrees at the root to 10.9 degrees at 95% of the blade radius. The rotor was positioned such that the rotor axis was in line with the airfoil chord line and in the middle of the test section. The airfoil was made by taking a NACA 0029 airfoil and separating the airfoil at the point of maximum thickness and putting in a long parallel section, increasing the chord to 3.05 m. The In order to make the boundary layer envelope the entire rotor plane, a 1.3 cm trip strip was placed on both sides of airfoil where the leading airfoil section meets the parallel extension. The end of the altered NACA 0029 airfoil extended into an anechoic chamber where far field acoustic measurements could be made. Acoustic measurements were made with an array of 9 microphones positioned both in and out of the flow. Background measurements were obtained using a "dummy hub" with no blades and then subtracted from the bladed runs. A clear haystacking pattern was shown from the measured acoustic spectra. The inflow turbulence was characterized by taking hot-

wire velocity measurements just upstream of the rotor position. Both single measurements, and two-point velocity measurements were taken. Single measurements were used to characterize the mean velocity field, and two-point measurements were used to quantify a subset of the incoming turbulence. A model of the correlation function was then used extrapolate the full correlation function interacting with the rotor. Turbulence characteristics were assumed to be symmetric about both sides of the NACA 0029 airfoil, due to symmetric static pressure measurements about the airfoil's top and bottom surfaces. Calculated thrust spectra were obtained by applying a coordinate transform to incorporate anisotropy effects. The lift fluctuations were then radiated to the far field using a compact dipole model to obtain acoustic spectra. The lift fluctuations were calculated with both anisotropic and isotropic turbulence models. The measured and predicted acoustic spectra were shown to agree well for the anisotropic predictions, while the isotropic turbulence assumed predictions showed worse agreement.

Morton (2012) also made noise predictions based on boundary layer measurements. He however studied the noise created by a 2.25 scale version of Sevik's rotor ingesting a thick, turbulent, two-dimensional boundary layer. He made two-point velocity measurements in the Virginia Tech Stability wind tunnel in the semi anechoic configuration to fully characterize the boundary layer's four-dimensional correlation function. He used that correlation function to predict the far field sound generated by the rotor using a strip theory approach developed in Glegg *et al*. (2012). His predictions show that the haystacking noise is dominant and that the sound source is dipole like, but does not have a null in the rotor plane. The absence of null is due to the alignment of the source dipoles with the blade lift vector. Blade twist causes the dipoles to be misaligned with the rotor plane, resulting in the lack of null in the directivity.

While directly measuring turbulence scales greatly improved upon predicting the haystacking response, all of these turbulence measurements were made with the rotor removed from the flow, effectively ignoring distortion of the turbulence as it interacts with the rotor. The inclusion of turbulence distortion had been studied earlier by Majumdar and Peake (1998). They made noise predictions of rotor turbulence interactions from the ingestion of atmospheric turbulence. They were able to model the haystacking phenomena using rapid distortion theory to model the distorted turbulent field at the fan face. Strip-theory was then used to calculate the unsteady loading on the fan blades. They predicted noise from inflight and static conditions and found haystacking noise especially prevalent in static conditions. It was shown that this is due to the fan causing a contraction of atmospheric turbulent eddies into long thin filaments that are cut many times by successive rotor blades.

Alexander *et al*. (2013) expanded upon Morton (2012) by taking acoustic data of the 2.25 scale version of Sevik's rotor ingesting a fully turbulent two-dimensional boundary layer in the Virginia Tech stability wind tunnel in its semi-anechoic configuration. This is the same facility used to obtain the undistorted fully four-dimensional correlation function in Morton (2012). Alexander *et al.* confirmed that the rotor source is not an axially aligned dipole due to a lack of a null from measured far field spectra at a plane 90° off of the rotor axis. Using the full four-dimensional velocity correlation matrix from Morton (2012) and accounting for distortion of the turbulence into the rotor face using a modified form of rapid distortion theory from Glegg *et al.* (2013), far field noise predictions were made and compared with measured spectra. They show very strong agreement in predicting the number of haystacks as well as the peak magnitudes of the first two haystacks. Alexander *et al*. also introduced an approach to inferring turbulence scales. A time-frequency approach was utilized to determine stream-wise scales, and a Gaussian was fit to the haystacking peak decay to determine lateral scales. It was found that lateral scales remained constant while the stream-wise scales increase with advance ratio.

Alexander et al. (2014) expanded upon this study by taking further data in the same tunnel-rotor configuration as Alexander et al. (2013). Alexander et al. utilized tuft visualization on the wall near the rotor, as well as took on blade hotwire measurements. Hotwire probes were mounted on the outer 20% of a rotor blade, and on the outer 10% of a trailing blade. Tuft visualization indicated separation and flow reversal on the wall for advance ratios less than 0.86. The phase-averaged upwash velocity was measured and shown to have its maximum upwash in the deepest part of the boundary layer, but slightly skewed towards the blade down-stroke side. Blade to blade unsteady upwash coherence spectra were calculated using Morton (2012)'s boundary layer measurements. These were compared with unsteady upwash coherence spectra measured by the on-blade hotwire instrumentation. For lightly thrusting conditions, measured upwash coherence spectra agree well with predictions. However, as the thrust increases and the rotor enters the regime with boundary layer flow reversal, the predictions deviate. A haystacking structure begins to appear in the coherence spectra that is not predicted at all. This is due to the fact that the response from interacting with flow reversal cannot be predicted by classical rapid distortion theory. A response at the shaft rate and its harmonics was also found in the coherence spectra. This is due to turbulent structures having large enough length scales for an individual blade to cut it multiple times.

In a study to be presented at the 2015 AIAA acoustics conference in Dallas, Glegg *et al.* (2015) applied a RANS simulation approach to predict the flow field near a rotor ingesting a turbulent boundary layer. The same setup from Alexander *et al.* (2013) was used in this simulation. It was shown that an arch vortex appears near the rotor disk plane for high thrusting conditions. This arch vortex will be ingested by the rotor, causing a change in generated noise. Glegg *et al.* (2015) believes this will result in an increase in measured far field noise. Glegg *et al.* (2015)

showed that the flow reversal will appear for advance ratios of less than 0.8, agreeing well with the flow visualization from Alexander *et al.* (2014). However, this implies that modified Rapid Distortion Theory developed in Glegg *et al.* (2013) cannot be used where flow reversal occurs.

This flow reversal due to rotor hull interactions was first noted by Huse (1971). He hypothesized that this was dominantly created by the pirouette effect. The pirouette effect is flow reversal created when the normal stream tube contraction into a rotor is significantly blocked by a hull or boundary. This causes part of the suction side of the rotor disk plane to not have enough fluid, resulting flow reversal near the tip gap. When this flow reversal results in a vortex, it is called the propeller hull vortex (PHV). Carlton (2007) notes that while the tip gap is the dominant geometric factor in the appearance of PHV, flat plate boundary geometries increase the likeliness of PHV over curved geometries.

Sato *et al*. (1986) investigated the nature of this flow reversal by placing flat plates in proximity to six different rotors immersed in water at the IHI Research Institute Circulating Water Tunnel. The rotors varied in diameter from 109 to 150 mm, and had five right handed, and one left handed rotor. Five of the rotors were modeled after conventional merchant ship rotors, and one was representative of a typical patrol ship rotor. The flat plate was systematically moved closer to the rotors, and bubble flow visualization was utilized to examine the nature of the flow separation. Sato *et al.* found that the nature of flow reversal was a function of the rotor tip gap to diameter ratio, c/D, and the load factor, K_T, which is related to the propeller thrust coefficient. It was shown that for low thrust, high tip gap conditions, no flow reversal was found. As the thrust was increased and the tip gap lowered, five distinct types of flow reversal were observed; reverse flow with no visible vortex, aft vortex flow reversal, double vortex flow reversal, fore vortex flow reversal, and for extremely small tip gaps, the splatter vortex. Martio (2011) created part of Sato's test matrix using the URANS solver, FINFLO. The propeller geometry was set to be the INSEAN E779a propeller, which is a 227 mm diameter, four-bladed propeller. The tip clearance-diameter ratio, c/D, was set to 0.157, and the load factor was varied from 2 to 531.7. The rotor rotational rate was kept at a constant 708 RPM, and the blade loading was varied through modifying the free stream velocity. They found that the vortex behavior was highly unstable and time dependent. Because of this, it was difficult to visualize through analyzing the pressure and velocity fields. Instead, vortex visualization was achieved through tracing of streamlines. The vortex interaction classifications observed from the simulations were found to match with reasonable agreement with those found experimentally. They were able to visualize the no reverse flow, no vortex reverse flow, aft vortex, double vortex, and fore vortex regions described in Sato *et al.* (1986). They also noted that for low advance ratios, the vortex flow reversal interacts with the blades. When this occurs, they found that the thrust coefficient oscillates strongly at the blade passage frequency. It was also found that for some flow reversal cases it was possible for PHV to not interact with the blades.

In two studies to be presented at the 2015 AIAA acoustics conference in Dallas, Wisda *et al.* (2015) and Murray *et al.* (2015), took PIV data in and near the tip gap for the rotor configuration used in the studies of Alexander *et al.* (2013 and 2014). They also modified the rotor mounting system such that the rotor could be yawed. Time averaged data shows agreement with RANS predictions from Glegg *et al*. (2015), revealing a distinct double vortex form flow reversal at low advance ratios. Conversely, instantaneous velocity vector fields show that locations of contra-rotating vortices are extremely unsteady. Their locations are sporadic, or at times, not even visible. Acoustic data taken revealed that yawing the rotor changed the effective angle of attack distribution of the rotor disk plane, resulting in far field acoustic effects. However not enough planes of PIV data were taken to verify the actual angle of attack distribution of the rotor disk plane, and no data were taken outside of the boundary layer.

1.3 STUDY GOALS

This study aims to gain a better fundamental understanding of the acoustic response to a rotor ingesting a thick fully turbulent anisotropic 2-dimensional boundary layer through further analyzing blade mounted hotwire probe data, acoustic measurements, and tuft analysis from Alexander *et al.* 2013 and 2014. From the above literature review, it can be seen that much progress has been made in the past 45 years in characterizing boundary layer turbulence interactions. It has been known that accounting for coherent blade to blade interactions with turbulence, as well as modeling stochastic anisotropic turbulent eddies is key in accurate acoustic predictions. However, rapid distortion theory is one of the few available simple tools that are able to model the distortion of the turbulent eddies as they get ingested into the rotor plane. As shown in Glegg *et al.* (2015) and Alexander *et al.* 2014, classical rapid distortion theory is not applicable to rotors ingesting two-dimensional boundary layers at low advance ratios. It was also noted that for low advance ratios, the haystacking response becomes tonal, and seems to correspond with wall boundary layer separation. This was shown in Martio (2011)'s simulations of reverse flow ingestion, but only the blade loading was simulated. No far field acoustic implications of flow reversal ingestion have been simulated or experimentally found. Further understanding of the blade response to ingesting separated flow is still needed. This studies aims to resolve these unknown phenomena through the following goals:

- Characterize distortion of the mean flow as it is ingested by the rotor to gain a better understanding of the true angle of attack seen by the rotor disk plane.
    - The theoretical undistorted angle of attack distribution seen by the blade chord line will be computed and compared with distributions computed from on-blade hotwire measurements in the outer 20% of the rotor disk plane.
- Expand upon Alexander *et al* 2013 and 2014's analysis of the rotor boundary layer interaction's far field acoustics to better understand RPM and inflow speed effects.

- Demonstrate the ability to reliably and objectively detect eddy passages through acoustic analysis.
    - This will be done through analyzing acoustic data by phase averaging multiple microphone signals together to reduce noise and, using a time frequency approach, discern eddy passages.
    - The mean blade response function from the phased average acoustic signals through further phase alignment of individual eddy passages. This will allow for more insight on the acoustics corresponding to separated wall boundary layer conditions.

2 THE EXPERIMENTAL SETUP OF ALEXANDER *ET AL.* 2013 AND 2014

This study is an expansion upon Alexander *et al.* (2013) and Alexander *et al.* (2014) and only used data obtained during those two studies. This section will describe the apparatus, instrumentation, and measuring techniques used for these two studies.

2.1 WIND TUNNEL

All measurements for this study were conducted in the Virginia Tech Stability Wind Tunnel. The stability tunnel is a continuous, single return facility with a 1.83 meter test section. The tunnel fan is 4.3 meters in diameter and consists of 8 Clark Y airfoil blades. It is powered by a 0.5 MW DC motor capable of generating flows up to 80 m/s in the test section. A schematic of the wind tunnel is shown below in Figure 1. Downstream of the fan is an air exchange tower followed by a 5.5 x 5.5 meter settling chamber and seven turbulence reducing screens. The settling chamber is also acoustically treated with a lining of 50mm foam. The flow then undergoes a 9:1 contraction into the test section. The test section is 7.3 meters long and easily removable. The measured turbulence levels in the test section are extremely low, varying from 0.02% at 20 m/s and 0.03% at 57 m/s. Downstream of the test section are 8 0.16 meter high vortex generators which prevent separation of the boundary layer as the flow moves through the diffuser.

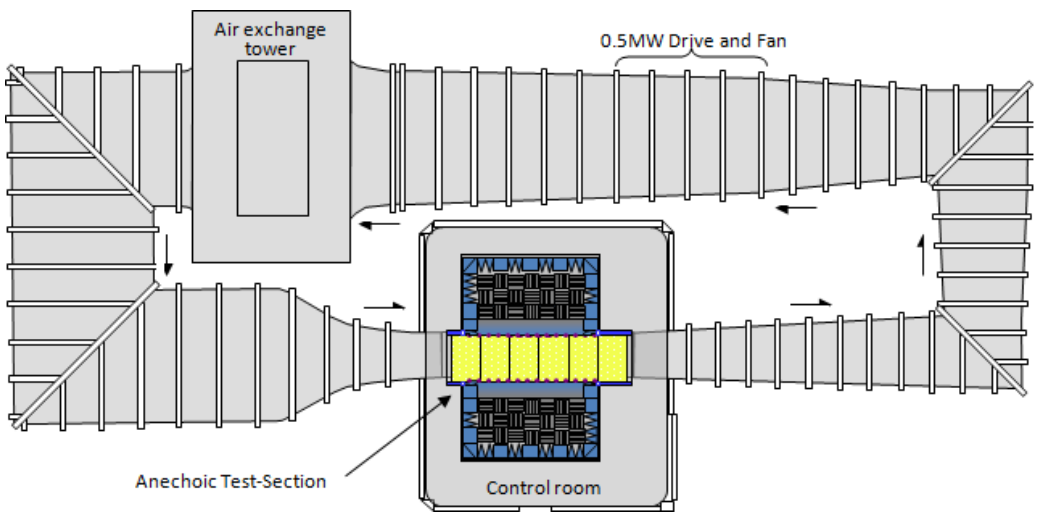

Figure 1: Virginia Tech Stability Wind Tunnel layout

The wind tunnel is also acoustically treated. The locations of acoustic treatment are shown in Figure 2 from Remillieux *et al.* (2008). The diffuser side walls are lined with 5 cm thick melamine foam to absorb high frequency noise created upstream of the fan. The fan was treated

with a machined Delrin liner around the blade tips to reduce the tip gap. The diffuser and fan adjustments contribute to a combined 6 dB reduction in noise in the test section across the entire frequency spectrum. The section of the circuit downstream of the air exchange tower was lined with 5 cm thick urethane foam, reducing noise under 1 kHz by 1dB. The settling chamber was similarly treated, reducing test section noise by 6 dB across the entire frequency spectrum.

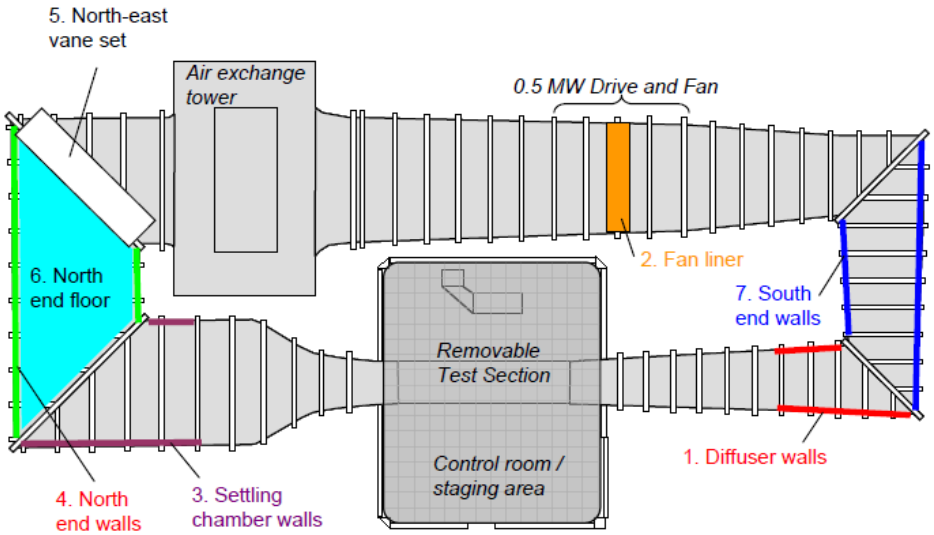

Figure 2: Virginia Tech Stability Wind Tunnel acoustic treatments

2.1.1 Anechoic Test Section Configuration

As previously stated, the Virginia Tech Stability Wind Tunnel's test section is easily removable, allowing for many different testing configurations including an anechoic configuration. This configuration is achieved by having test section floor and ceiling panels constructed of webbed aluminum wrapped in Kevlar and backed by foam padding and wedges. The wedges are 0.457 meters high and prevent reflections over 190 Hz. The test section side walls are also entirely replaced by 6 meter long windows made from Kevlar stretched onto an aluminum frame. Two chambers lined with acoustic foam wedges are attached to the sides of the test section. The chambers cover 6 meters in the streamwise direction, extend 2.8 meters from the Kevlar window and are 4.2 meters high. The chambers are lined with 0.61 meter high foam wedges which prevent acoustic reflections over 140 Hz. The chambers are anechoic down to 180 Hz, creating an ideal location for the placement of microphones.

This study was conducted in a semi-anechoic configuration in which the starboard side Kevlar wall is replaced with 6 Lexan sheets extending the length and height of the test section to create a smooth wall. The semi-anechoic configuration's test section is shown below in Figure 3. A diagram of the exact semi- anechoic configuration used for this study is shown below in Figure 4. As shown in Figure 4, the rotor was placed in close proximity to the Lexan wall and approximately midway along the length of the test section.

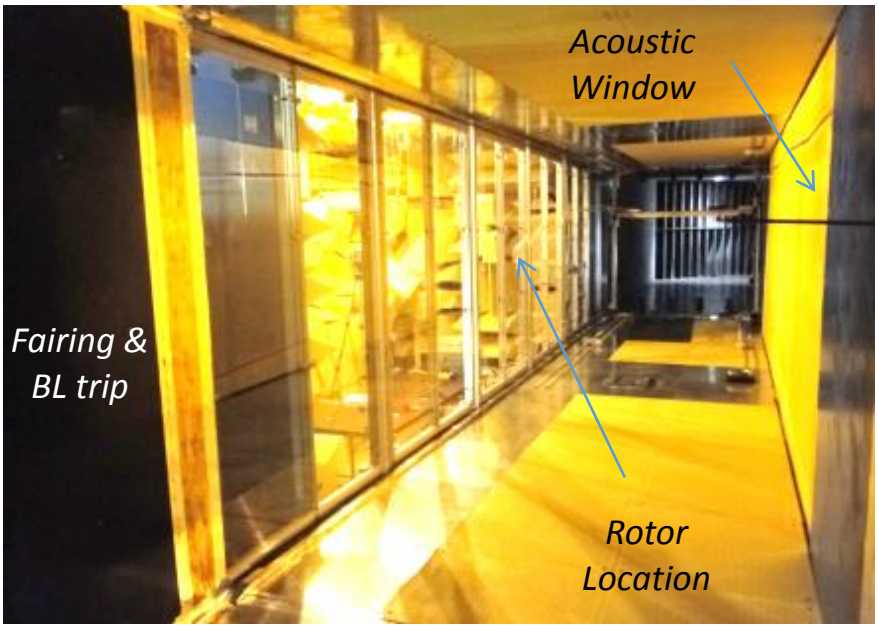

Figure 3: Semi-anechoic test section configuration

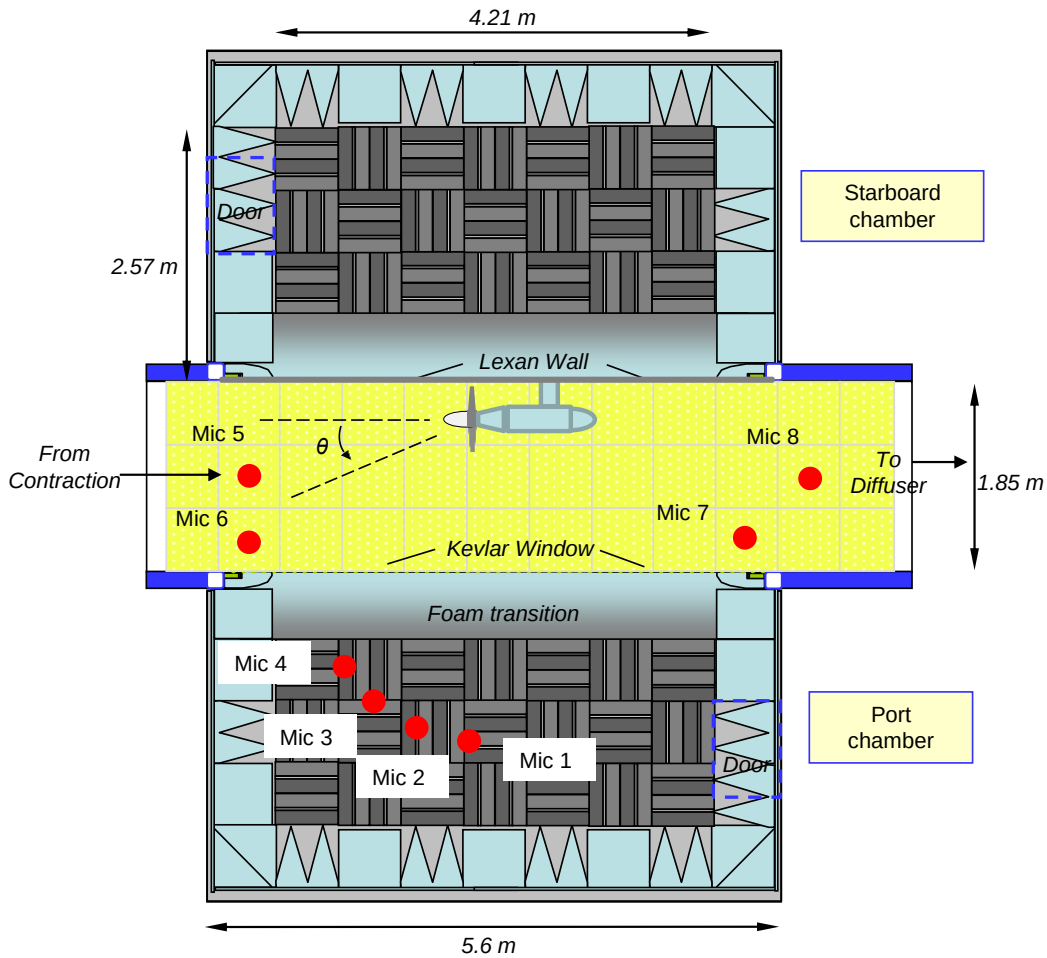

Figure 4: Diagram of the semi-anechoic test section configuration used for this study

The addition of the Lexan wall to the test section reduced the test section width by roughly 0.12 meters. As a consequence to this, the tunnel contraction from the settling chamber no longer smoothly attaches to the test chamber. A modified contraction was utilized upstream of the test section to smoothly transition from the settling chamber to the test section and is shown below in Figure 5. A diagram of the entire test section with the contraction piece is also shown below in Figure 6. The contraction was made from two large pieces of flexible ABS plastic attached to a wooden frame extending 2.4 m. To further smooth the transition from the contraction to the test section, the upstream edge of the sheet was screwed and foil taped to the tunnel wall, and the downstream edge was attached to the Lexan wall using shim sheet metal and foil tape. A trip strip was placed midway on the contraction piece to generate a fully turbulent boundary layer that is 101 mm thick at the rotor plane. The trip strip was 9.5 mm high and made from aluminum. Its exact location is 4.76 meters upstream of the rotor disk plane. This semi-anechoic configuration was used by several other studies including Morton (2012), Meyers *et al.* (2013), and Awasthi *et al*. (2014).

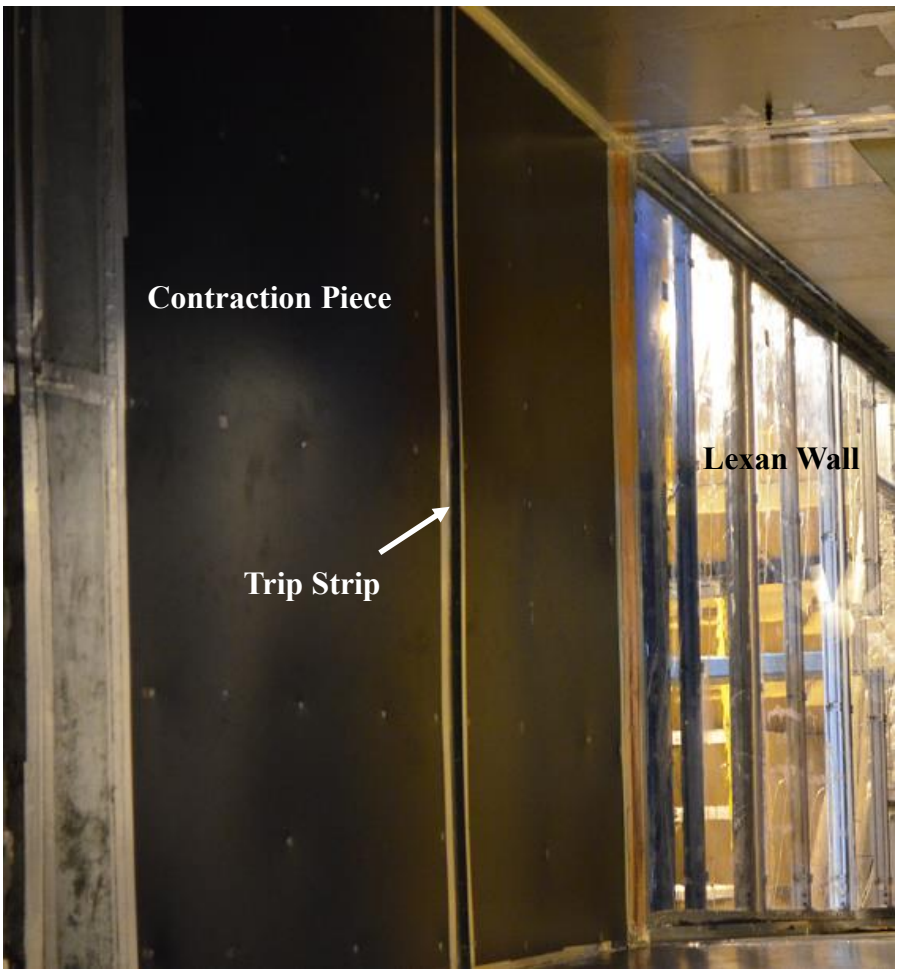

Figure 5: Semi-anechoic configuration modified contraction

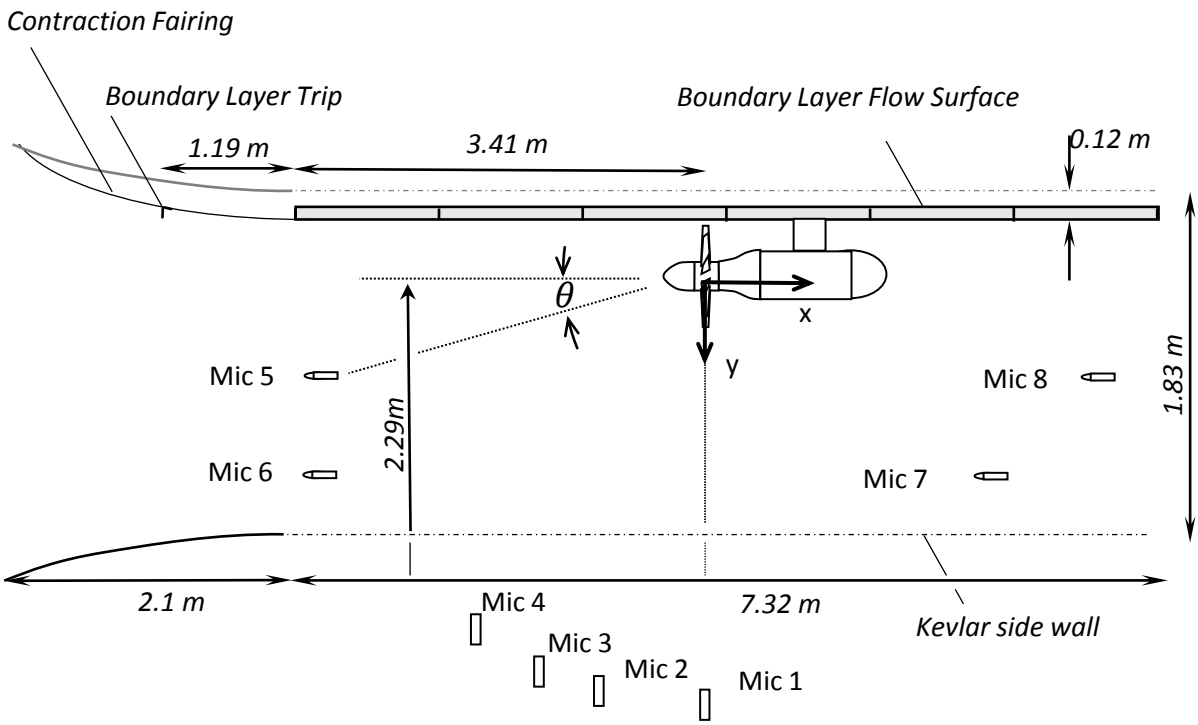

Figure 6: Top down view diagram of test section with contraction and trip strip modifications (Note coordinate system is defined centered on the rotor disk plane with +z being out of the page)

It is important to note that the coordinate system used is consistent with the axes shown in Figure 6. The x-direction is aligned with the streamwise direction. The y-direction is normal to the Lexan wall, and positive towards the Kevlar side wall. The z direction is normal to the floor and positive up, or out of the page in Figure 6. The coordinate system is centered on the tip of the rotor nosecone.

An Esterline 9816/98RK pressure scanner with a range of ±10 inches of water was used to take mean wall pressure data. The scanner has 96 ports and a rated accuracy of ±0.05%. Twenty four pressure taps were placed along the floor and ceiling panels near the Lexan wall to verify a zero pressure gradient. The Lexan panels were adjusted until a pressure coefficient gradient of less than 0.05 over the entire wall was achieved with reference to the most upstream pressure tap.

2.2 ROTOR SYSTEM

The rotor used in this experiment is a 457 mm diameter 10 bladed rotor, shown below in Figure 7. The blades have a 57.2 mm chord length with no taper or sweep. The twist is relatively uniform from 55.6^o from the rotor plane at the hub to 21.2^o at the blade tip. The blade twist angle was obtained directly from the rotor blade CAD file, and is shown below in Table 1. This blade geometry is a 2.25 times scaled replica of the rotor used by Sevik (1971). However, the hub

diameter was increased to 127 mm to allow for room for instrumentations, and each blade root was shortened by 6.4mm to maintain the 2.25 times scaling on the disk plane diameter. The design and advance ratio is 1.17 as stated by Sevik (1971). JavaProp also found the zero thrust condition for this rotor to be 1.44. This rotor is left handed, such that the rotor blade approaches the wall from the test section floor and leaves towards the ceiling when unyawed. This directionality is represented on Figure 7. The rotor was powered by an AKM-64P-ACCNDA00 Kollmorgen servomotor and a S61200 servo drive. The rotor was positioned with a 20.3 mm tip gap between the Lexan wall and the closest possible blade position. For this experiment, the rotor plane was placed 3.6 meters from the front of the test section. A 212 mm long, 127 mm diameter nose cone was attached to the front of the rotor disk plane. A 291 mm long smooth foam fairing is attached downstream of the rotor to provide a smooth transition to the 219 mm diameter motor housing. Air holes were machines into the housing to prevent overheating of the motor, and were covered with tape during acoustic measurements. Attached to the back of the rotor is a 219 mm diameter foam end piece to promote a smoother transition of flow from around the rotor housing to the wake.

Table 1: Blade twist angle distribution

r (m)	r/R	β (degrees)
0.06	0.28	55.6
0.08	0.36	48.4
0.10	0.44	43.6
0.12	0.52	39.2
0.14	0.60	35.2
0.16	0.68	31.6
0.17	0.76	28.5
0.19	0.84	25.6
0.23	1.00	21.2

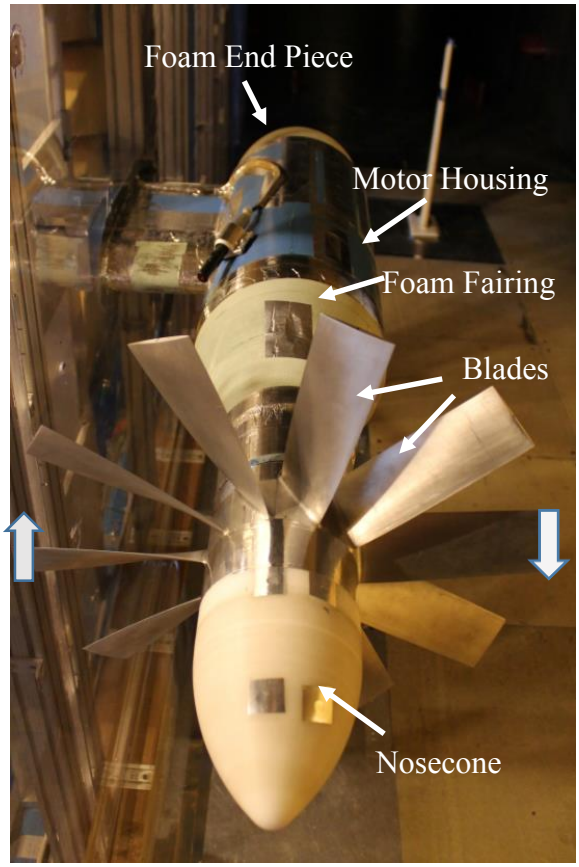

Figure 7: Rotor in its acoustic test configuration

The rotor was supported by a 154 mm by 76 mm hollow aluminum beam welded to the motor housing. The beam extended out of the test section through a hole in the Lexan wall and was mounted in a structure made up of two externally mounted aluminum I-beams. This is shown below in Figure 8. Two plates are attached to the beam structure with rectangular holes cut in them. Four rectangular plates extending normal to the test section were welded to the outside of the plates. These welded plates allowed for minor rotor positional adjustments through tightening screws tapped around them. The section of the rotor support beam located between the housing and the wall was covered with a smooth streamlined foam pieces to reduce effects of the support beam on the flow.

Figure 8: Rotor mounting system

To obtain background noise generated by the rotor and housing, the rotor was run with the blades removed and the motor on. This configuration is shown below in Figure 9. Spectra obtained from these measurements were subtracted from the blade-on runs in order to isolate the rotor-turbulence interaction noise from the noise generated from the tunnel facility and the rotor housing and strut.

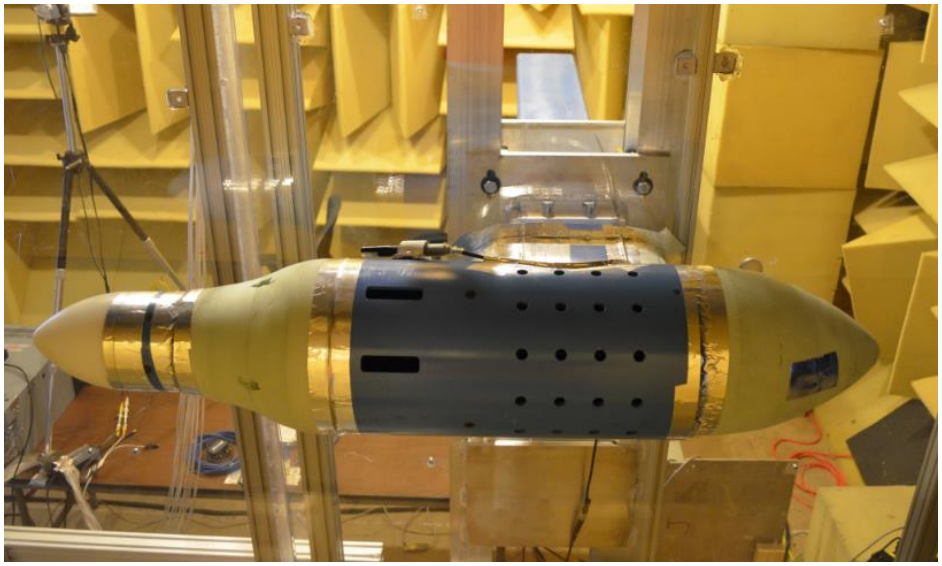

Figure 9: Rotor with blades removed in its background noise configuration

To record rotor blade position, a laser pointer was passed through the rotor disk plane to a photodiode on the wall. The laser was mounted on top of the rotor housing and passed through the rotor plane at 90% blade radius. The photodiode was then taped to the outside of the Lexan wall

such that the laser would hit it. The laser-photodiode setup is shown in Figure 10. The photodiode sensitivity was set so that a square wave signal was generated as the laser beam was cut by the passing blades. The photodiode output was measured simultaneously with the acoustic data using a 3050-A LXI DAQ sampled at 65536 Hz. This allows for determination of rotor position to within 0.41 degrees at 4500 RPM.

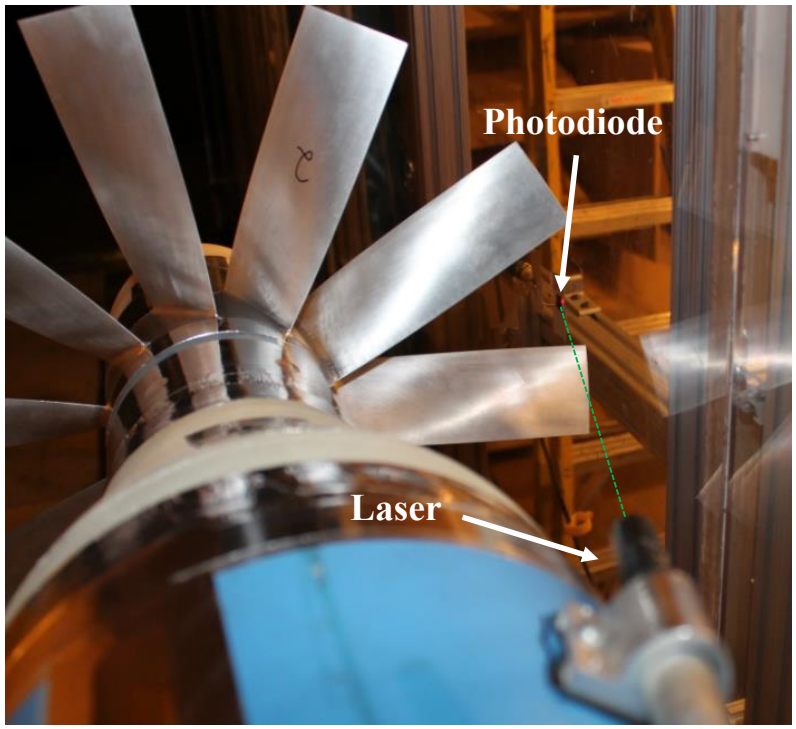

Figure 10: Laser-photodiode system

2.2.1 Rotor Performance Analysis with JavaProp

In order to estimate the thrust metrics of the rotor, JavaProp was utilized. JavaProp estimates rotor performance using blade element theory, which analyzes small spanwise elements of each blade and treats them independent of each other. The momentum change across each element is then integrated, along with cross flow and other corrections, to obtain full rotor performance metrics. The nose cone and hub are treated as a cylinder of undistorted flow. The lift and drag coefficient polars were computed at a Reynolds number range of roughly 230,000, which corresponds to the blade tip conditions at 2500 RPM, and an inflow velocity of 20 *m/s*. The thrust curve is shown below in Figure 11. The red data points indicate positive thrust coefficients, while the blue indicate negative thrust coefficients. This thrust curve was identical for tested free stream velocities of 10, 15, 20 and 30 *m/s*. Note that the thrust coefficient, C_T is defined as

$$C_T = \frac{T}{\rho \eta^2 D^4} \tag{1}$$

where T is thrust, ρ is the free stream density, n is the rotational rate in revolutions per second, and D is the rotor diameter.

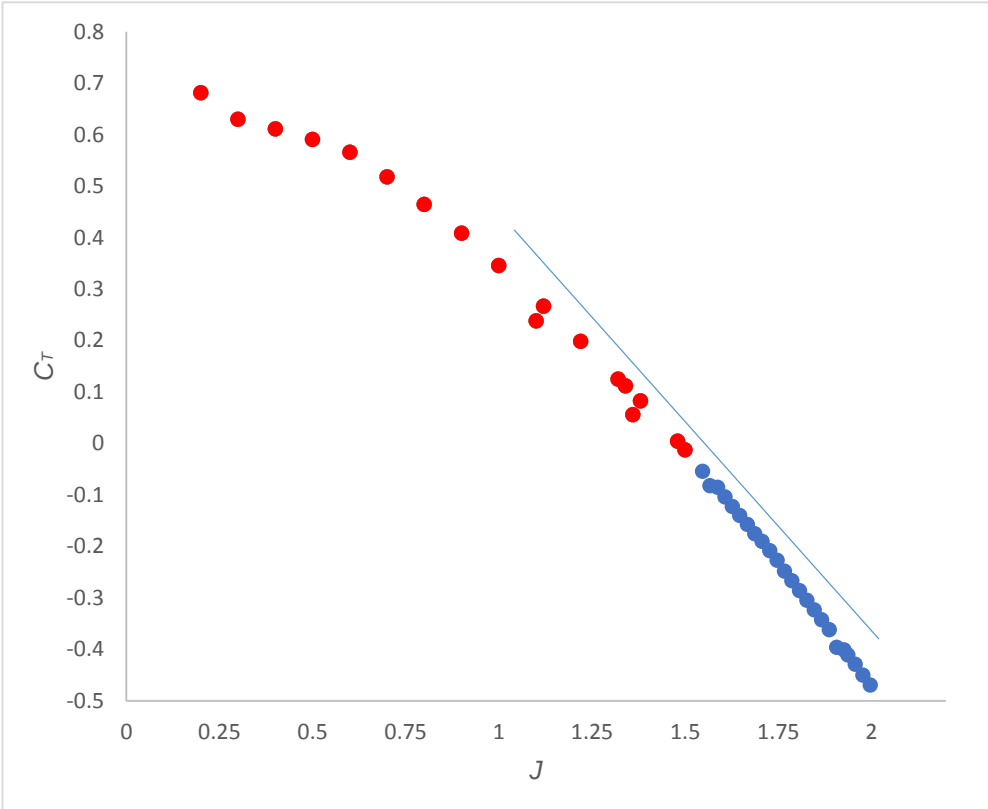

Figure 11: Rotor thrust coefficient curve

This thrust curve appears fairly normal for most propellers qualitatively, but has higher overall thrust coefficients than most conventional propeller design's thrust curves. However, this propeller is not a conventional design. It has a high number of blades which would increase the magnitude of the thrust coefficients. There is a linear region starting at a braking condition of J=2 that extends into lower advance ratios. As the advance ratio decreases, the gains in thrust start to decrease as stall becomes problematic. JavaProp predicts a maximum thrust for this rotor of about 240 N at a flow speed of 30 m/s and rotational rate of 5500 RPM.

2.3 Boundary Layer Characterization

The boundary layer velocity profile was measured using a 4 sensor hotwire probe operated by a Dantec Streamline anemometer. The hotwire probe and traverse are shown in Figure 12. The

data were sampled using an Agilent E1432 16-bit digitizer at 6400 Hz. The probe is made up of four 5µm diameter and 1.2 mm long tungsten wires positioned 45° from the streamwise direction in a square pattern. The four sensor hotwire gives redundant measurements of the velocity field, reducing uncertainty. The sensor angle calibration was carried out in a low turbulence jet, and velocity calibrations were carried out in the tunnel facility to account for temperature changes. The probe was located 789 mm upstream of the rotor disk plane, and was traversed vertically from 8.5mm to 152 mm from the wall in 30 logarithmically spaced measurements locations. The boundary layer characteristics are shown below in Table 2, where δ is the boundary layer thickness, δ* is the displacement thickness, and θ is the momentum thickness. It is important to note that due to a measurement error, the 15 m/s characteristics are interpolated from the 10 and 20 m/s cases.

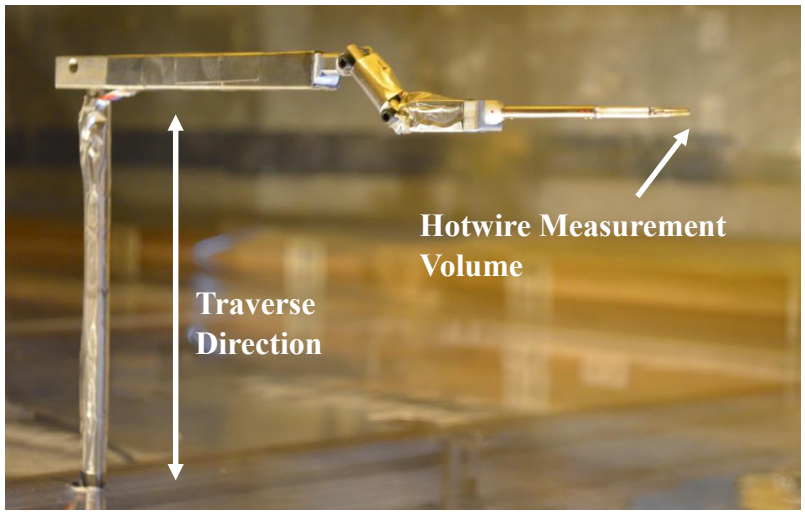

Figure 12: Close-up view of the quadwire used for boundary layer measurements

Table 2: Boundary layer characteristics measured by Alexander, W. N., Devenport, W., Morton, M. A., and Glegg, S. A. L., "Noise from a Rotor Ingesting a Planar Turbulent Boundary Layer", 19 AIAA/CEAS Aeroacoustics Conference, May 27-29, 2013, Berlin, DE, AIAA-2013-2285. Used under fair use, 2015

U_{ref} (m/s)	δ (mm)	δ* (mm)	Θ(mm)
10	102.2	15.2	10
15	101.2	15	10.1
20	100.1	14	9.3
30	99.7	13.3	8.9

2.4 On-Blade Hotwire Measurement System

Six cross-wire probes were attached to 2 successive rotor blades. The measurement volume of the probes were set to 19mm in front of the leading edge of their attached blade. The leading

rotor blade had 4 probes attached at 98.5%, 95%, 90%, and 80% of the blade radius. The trailing rotor blade had 2 probes attached at 98.5% and 90% of the blade radius. The probe positions are shown below in Figure 13. The probes were connected to a Tao Systems custom 4-channel constant voltage anemometer system which spun in the nosecone. The bridge voltage data was sent to a data acquisition system through a model AC6231 Moog high speed slip ring. The data acquisition system used was a model USB-6211 NI DAQ. Data were taken at 51200 Hz in 30 second intervals.

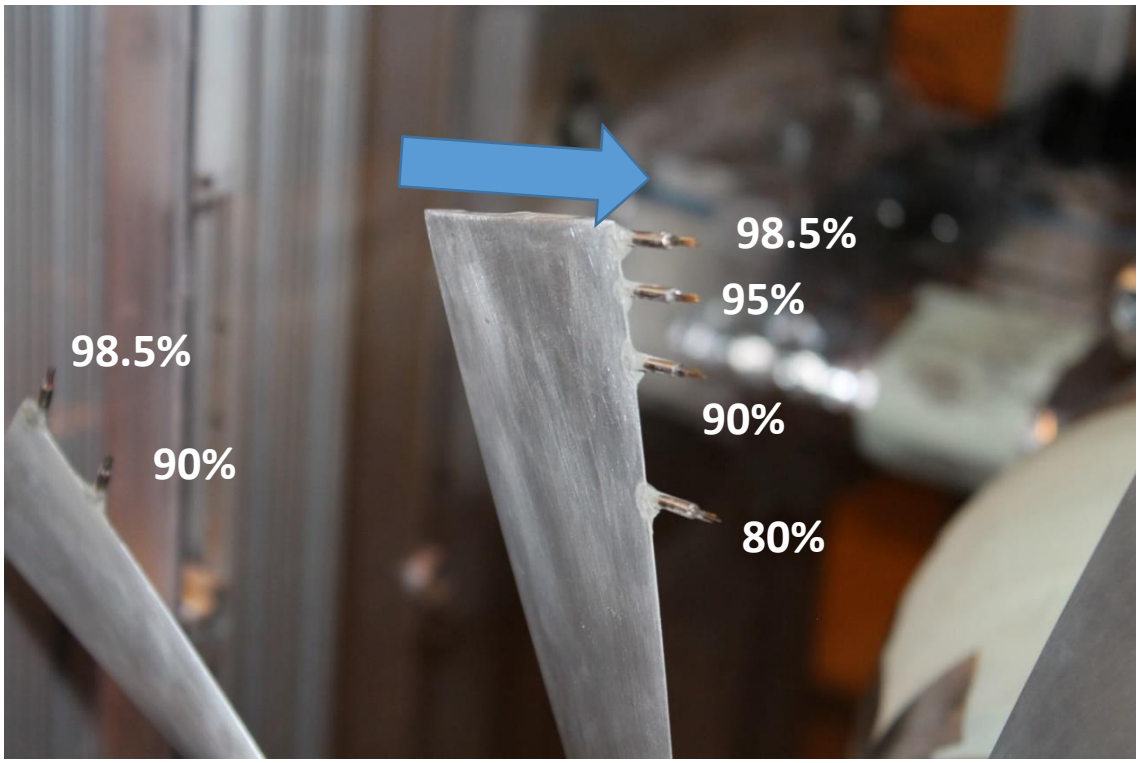

Figure 13: Blade-mounted hotwire probe locations

2.5 MICROPHONE MEASUREMENT SYSTEM

Eight Bruel & Kjaer 4190 ½ inch microphones were used for acoustic measurements. Four of the microphones were positioned in the test section, with two upstream and two downstream of the rotor. The inflow microphones are shown below in Figure 14. The inflow microphones were covered with UA-0386 bullet nose cones and mounted on thin streamlined stands. A close-up picture of the bullet nose cone is shown in Figure 15 below.

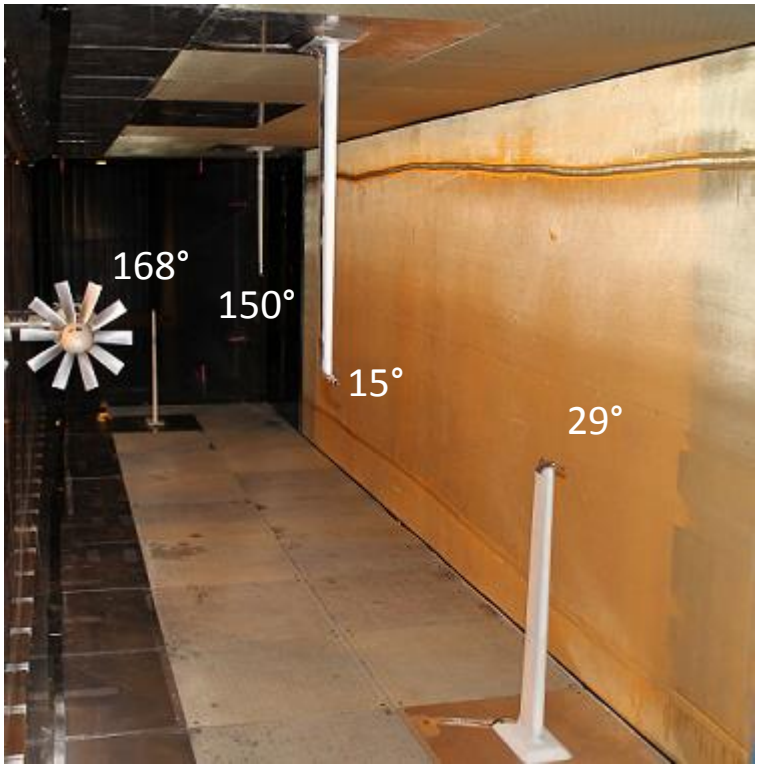

Figure 14: Test section with inflow microphone configuration

Figure 15: B&K inflow microphone with bullet nose cone

The remaining microphones were positioned in an array in the port acoustic chamber. The acoustic chamber and chamber microphones are shown in Figure 16. The microphones were sampled at 65536 Hz for 32 seconds using five synchronized 3050-A LXI DAQs using B&K Pulse

14 software. The microphone positions are shown below. There are 7 microphone positions that sweep from 15 degrees to 90 degrees, allowing for a directivity study of the far field noise. There are also 2 positions downstream at 142 and 168 degrees. The 90 degree position is especially important as an axially-aligned dipole should radiate no noise to this position. The microphone positions are summarized below in Table 3. Microphones in the anechoic chamber are highlighted in green, while inflow microphones are highlighted in blue.

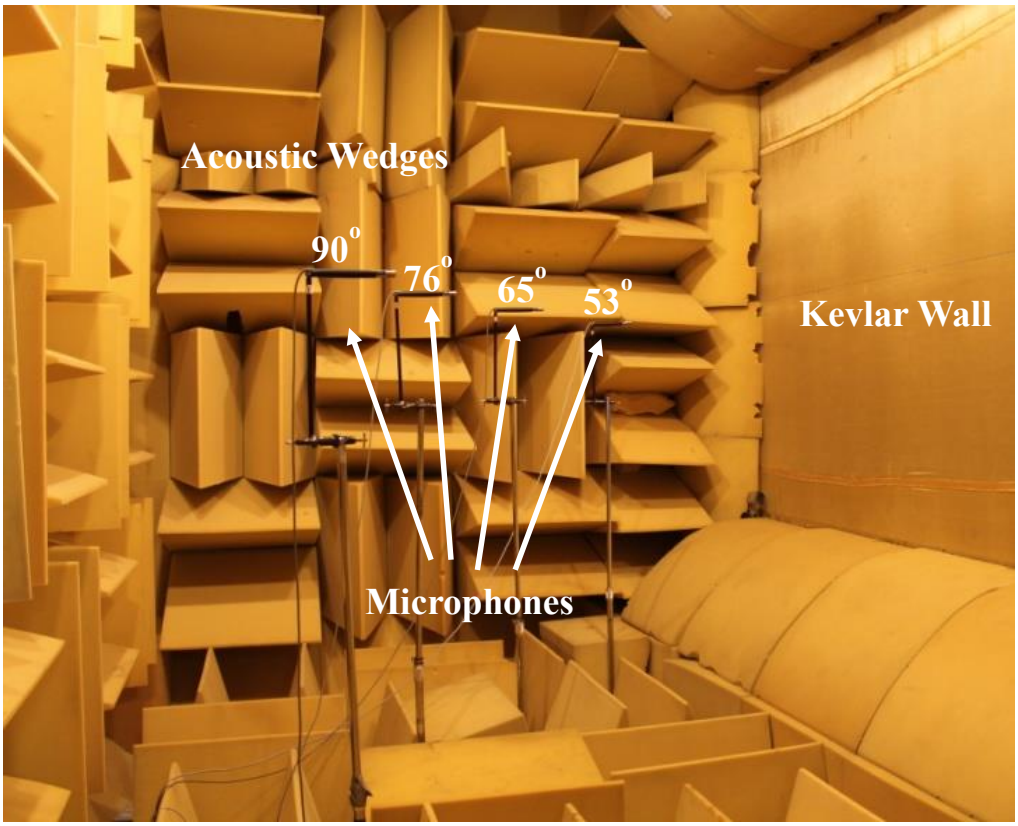

Figure 16: B&K port chamber microphones

Table 3: Microphone measurement locations (Green: Chamber Mics, Blue: Inflow Mics)

	Pos 1	Pos 2	Pos 3	Pos 4	Pos 5	Pos 6	Pos 7	Pos 8
θ, deg	**90**	**76**	**65**	**53**	**15**	**29**	**150**	**168**
x, mm	6	-730	-1251	-1715	-2161	-2108	2102	-2731
y, mm	3339	3129	2710	2253	554	1167	1180	554
z, mm	-159	-115	-121	-115	125	-121	133	-128

2.6 TEST MATRIXES

2.6.1 Acoustic Measurements

Acoustic measurements were made of the rotor interacting with boundary layers generated from both the single and double trip strip configurations. A total of 8 microphones sampled simultaneously at 65536 Hz for 32 seconds with positions described in Table 3 were utilized. In order to determine if there were any specific free stream or rotor RPM scaling unique from the advance ratio dependence, measurements were made that varied both RPM and free stream independently. The rotor was held at a constant 2734 RPM and the flow speed was varied from 10 m/s to 34 m/s in 2 m/s increments. This corresponds to advance ratios of 0.48 to 1.63. The tunnel was then held at a constant free stream velocity, and the RPM was varied. This was done for flow speeds of 10 m/s, 15 m/s, 20 m/s, and 30m/s. The test matrix also made sure to obtain measurements of advance ratios of 0.8, 1.1 and 1.44 for as many flow speeds as possible, so that advance ratio dependence could be compared directly for different flow speeds. The 0.8 and 1.1 advance ratio are moderate and low thrust conditions, respectively, and the 1.44 advance ratio is the zero thrust condition. This combined for a total of 85 acoustic runs with advance ratios spanning from 3.94 to 0.29. The test matrix is summarized below in Table 4 and Table 5 below.

Table 4: Sound measurements at a constant 2734 RPM

U_∞ *m/s*	*J*
10	0.48
12	0.58
14	0.67
16	0.77
18	0.86
20	0.96
22	1.06
24	1.15
26	1.25
28	1.34
30	1.44
32	1.54
34	1.63
Directivity angles from 15° to 168°	

Table 5: Acoustic test matrix for 10, 15, 20, and 30 m/s flow speeds (Note advance ratios are shown)

RPM	10m/s	15m/s	20m/s	30m/s
1000	1.31	1.97	2.62	3.94
1500	0.87	1.31	1.75	2.62
2000	0.66	0.98	1.31	1.97
2100	0.62	0.94	1.25	1.87
2200	0.6	0.89	1.19	1.79
2300	0.57	0.86	1.14	1.71
2400	0.55	0.82	1.09	1.64
2500	0.52	0.79	1.05	1.57
2750	0.48	0.72	0.95	1.43
3000	0.44	0.66	0.87	1.31
3250	0.4	0.61	0.81	1.21
3500	0.37	0.56	0.75	1.12
3750	0.35	0.52	0.7	1.05
4000	0.33	0.49	0.66	0.98
4250	0.31	0.46	0.62	0.93
4500	0.29	0.44	0.58	0.87
3282			0.8	
1194	1.1			
1790		1.1		
2387			1.1	
3581				1.1
1367		1.44		
1823			1.44	
2734				1.44
Directivity angles from 15° to 168°				

2.6.2 Hotwire Measurements

Due to slip ring limitations, only two cross-wire probes could be sampled simultaneously. To obtain a sufficiently large test matrix, 7 different configurations of measured hotwire probes were utilized. They are described below in Table 6. For each hotwire configuration, the rotor's advance ratio was varied by changing both the tunnel test section speed and the rotor RPM. Runs were made at flow tunnel flow speeds of 10, 15, 20 and 30 m/s. For each flow speed, the rotor rpm was varied from 1000 to 2500. The rotor RPM and inflow speed combinations, with corresponding advance ratios are summarized below in Table 7. Similarly to the acoustic measurements, care was

taken to obtain data at advance ratios of 1.44, 1.1, and 0.8 for as many flow speeds as possible. Also, this test matrix was carried out for both the single and double trip configurations, resulting in over 78 hotwire runs. The hotwire measurements highlighted in this study are identified in Table 7.

Table 6: On-blade hotwire configurations

Configuration	Blade Radius Location of Probe 1	Blade Radius Location of Probe 2
1	98.5% Leading	90% Trailing
2	95% Leading	98.5% Trailing
3	95% Leading	90% Trailing
4	90% Leading	90% Trailing
5	80% Leading	90% Trailing
6	95% Leading	80% Leading
7	98.5% Leading	90% Leading

Table 7: On-blade hotwire test matrix for 10, 15, 20, and 30 m/s flow speeds (Note advance ratios are shown)

RPM	10 m/s	15 m/s	20 m/s	30 m/s
1000	1.31	1.97	2.62	3.94
1500	0.87	1.31	1.75	2.62
2000	0.66	0.98	1.31	1.97
2100	0.62	0.94	1.25	1.87
2200	0.60	0.89	1.19	1.79
2300	0.57	0.86	1.14	1.71
2400	0.55	0.82	1.09	1.64
2500	0.52	0.79	1.05	1.57
1193	1.10			
1367		1.44		
1640	0.80			
1790		1.10		
1823			1.44	
2461		0.80		
2386			1.10	

3 RESULTS AND DISCUSSION

3.1 INFLOW DISTORTION AS SEEN BY THE ROTOR BLADES

In order to better understand the acoustic response of a rotor ingesting inhomogeneous turbulence, it is necessary to quantify the local blade flow conditions. Previous acoustic models such as Stephens and Morris (2008), used only the undistorted measured profile to obtain local blade flow conditions, while Alexander *et al.* (2013) estimated the inflow distortion using a modified form of rapid distortion theory from Glegg *et al.* (2013). However, for this study, 2-component hotwire data were taken in the outer 20% of the blade radius. With the undistorted upstream flow conditions known completely from Morton (2012), the actual extent of flow distortion can be quantified. Previous analysis on this has been done both experimentally by Alexander *et al.* (2014), who analyzed unsteady upwash seen by the blades, and theoretically by Glegg *et al.* (2013), who developed a modified rapid distortion theory based technique to estimate flow distortion into the rotor face. However, the effect of distortion on the angle of attack distribution of the rotor plane has not been explicitly examined.

Due to the alignment of the hotwires with the blade chord lines, it is easy to determine the angle of attack as seen by the blades. Determining how this is distorted is important as the angle of attack is directly proportional to the lift magnitude and can give insight as to where locally the rotor blades are stalling, thrusting, or braking. Readily available blade element theory models such as JavaProp do not account for the change in velocity profile due to the presence of the wall. This will cause deviations from predicted thrust values due to inflow conditions in the portion of the rotor disk plane immersed in the boundary layer differing from the rest of the rotor disk plane.

The rotor conditions highlighted in this section are shown in Table 7. The conditions were mostly at 2500 RPM, and had their advance ratios controlled by free stream velocity variance. A zero thrust condition was also obtained at 20 m/s and 1823 RPM. This was the highest RPM zero thrust case measured. These conditions correspond to advance ratios from 1.44 to 0.52, which are not thrusting and heavily thrusting, respectively. These conditions were chosen to have minimal RPM variance and still have a large advance ratio range.

3.1.1 Undistorted Angle of Attack Distribution Seen by the Rotor Blades

Using the rotor geometry and the complete inflow condition measured in Morton (2012) the undistorted angle of attack distribution seen by the rotor blades was calculated. The flow angle of attack, θ, at a given radius, r and blade angle, φ, was determined by

$$\theta(r,\varphi) = \tan^{-1}\frac{V_x(r,\varphi)}{V_\varphi(r)}, \tag{2}$$

where V_x is the streamwise component of velocity determined from boundary layer profile measurements and V_φ is the rotational velocity of the rotor blade given by

$$V_{\varphi}(r) = r\omega, \tag{3}$$

where ω is the rotational rate of the rotor in radians per second.

The final angle of attack distribution seen by the rotor blade chord line is given by the subtracting θ from the blade twist angle obtained from Table 1, β as shown by

$$\alpha(r, \varphi) = \beta(r) - \theta(r, \varphi). \tag{4}$$

Figure 17 shows the undistorted angle of attack distribution as seen by the blades for a free stream velocity of 20 m/s and a rotor RPM of 2500. This corresponds to an advance ratio of 1.05, which is a lightly thrusting condition. Shown below it in Figure 18 is the undistorted angle of attack distribution seen by the blades for a free stream velocity of 20 m/s, rotor RPM of 1823, and an advance ratio of 1.44. This is the zero thrust condition. The angle of attack distributions are shown facing the rotor face in line with the free stream with the rotor rotating clockwise. The hard wall is shown underneath the rotor. It is important to note that Figures 19 and 20 have the same colorscale, with extrema of -4 to 7 degrees angle of attack.

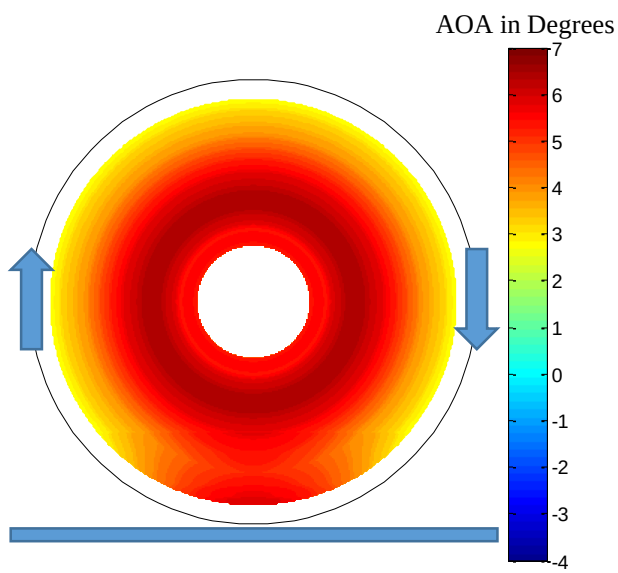

Figure 17: Undistorted angle of attack distribution as seen by the rotor chord line (20 m/s, 2500 RPM, J=1.05)

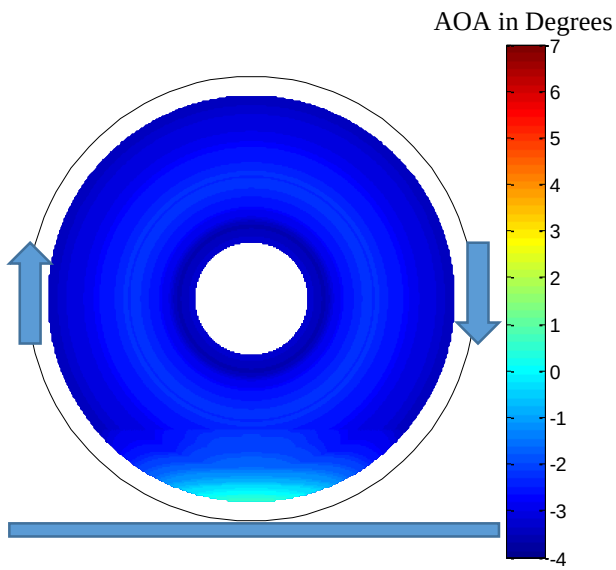

Figure 18: Undistorted angle of attack distribution as seen by the rotor chord line (20 m/s, 1823 RPM, J=1.44)

Figure 17 and Figure 18 show that the angle attack distributions for the thrusting and no thrust conditions have their highest value near the rotor hub and decrease in the radial direction. The thrusting angle of attack distribution in Figure 17 shows a 7 degree angle of attack near the hub that decreases to 3 degrees. The zero thrust angle of attack distribution in Figure 18 shows a -3 degree angle of attack near the hub that decreases to -3.5 degrees. The effect of the boundary layer is also shown, creating some angular non-uniformity. As the blades pass through the boundary layer, the streamwise velocity component decreases, resulting in an increase in angle of attack in the boundary layer. This can have significant acoustic implications. For example, Figure 18 shows that the rotor is has a local positive angle of attack in the outer 20% of the blade radius in the boundary layer, while the remaining outer 20% not immersed in the boundary layer has a negative angle of attack. This means that even for no thrust or braking conditions, there can be local thrusting in the boundary layer, which would result in the stretching and coherent cutting of turbulent structures. The far field acoustic response to this would be haystacking noise.

The increase in angle of attack distribution through the boundary layer is more distinct in Figure 18 for the zero thrusting, 1823 RPM case than shown in Figure 17 which is lightly thrusting and rotating at 2500 RPM. This is expected as the effect of the boundary layer is minimalized as the rotational rate of the blade increases. At high rotor RPMs the rotational component of the velocity vector dominates the streamwise component in the angle of attack computation. At infinitely high RPM, the undistorted angle of attack distribution would be identical to the blade

twist angle distribution, regardless of any realistic streamwise upstream conditions. This indicates boundary layer effects should have the highest impact on the angle of attack distribution of the rotor for lower rotor rotational rates.

3.1.2 Measured Angle of Attack Distributions Seen by the Rotor Blades

The angle of attack distribution as seen by the rotor blade chord line was much simpler to compute with the hotwire measurements, as the measurements were chord line aligned. The angle of attack distribution was simply calculated as

$$\alpha(r,\varphi) = \tan^{-1}\frac{V_N(r,\varphi)}{V_T(r,\varphi)}, \tag{5}$$

where V_N and V_T are the normal and tangent components of the velocity vector as seen by the chord line, respectively.

In order to obtain the measured velocity distribution measured by a single hotwire probe, $\vec{V}(\varphi)$, the laser clocking signal was used to phase lock the blades into 0.5 degree bins to allow for phase averaged velocity measurements. Because the radial test matrix was limited to the hotwire placement, the phase averaged velocity data was only obtained for blade radii of 80%, 90%, 95%, and 98.5% of the blade radius. This phase averaged data was further averaged over several measurements with the same inflow conditions. For example the 90% data from the 20 m/s, 2500 RPM condition was averaged from hotwire data from configurations 1, 3, and 4 in Table 6. This particular case includes four 90% hotwire measurements. Figure 19 and Figure 20 below show the measured angle of attack distributions (A) as well as their corresponding undistorted angle of attack distributions in the outer 20% of the blade radius (B). Figure19 shows the angle of attack distribution for the lightly thrusting case with a rotational rate of 2500 RPM, a flow speed of 20 m/s, and an advance ratio of 1.05. Figure 20 shows the angle of attack distribution for the zero thrust case with a rotational rate of 1823 RPM, a flow speed of 20 m/s, and an advance ratio of 1.44. It is important to note that the color scales in Figure 19 and Figure 20 are the same as those used in Figure 17 and Figure 18.

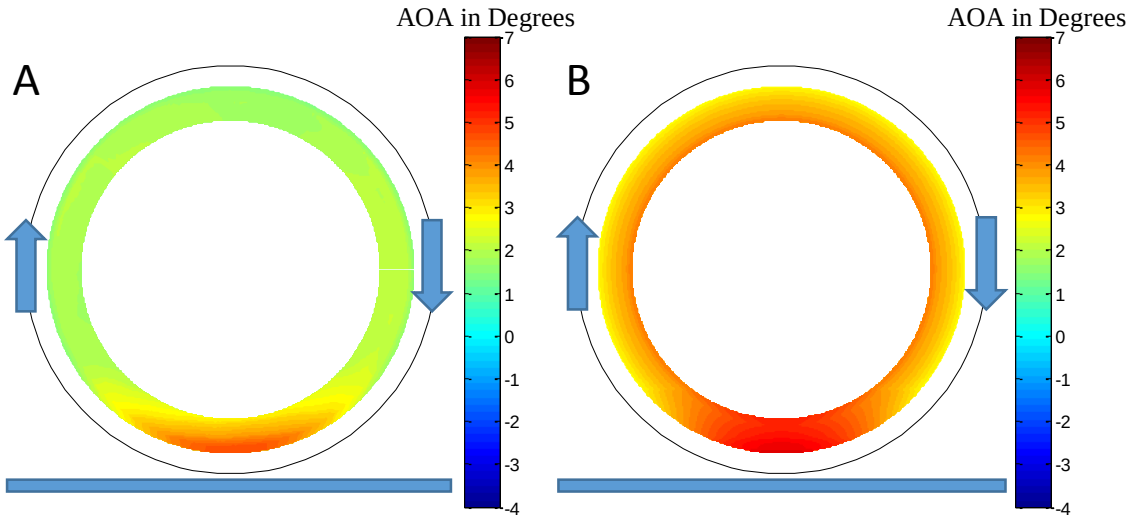

Figure 19: The angle of attack as seen by the rotor blade distribution in the outer 20% of the blade radius obtained from A) measured hotwire data, and B) undistorted flow analysis
(J = 1.05, 2500 RPM, U_∞ = 20 m/s)

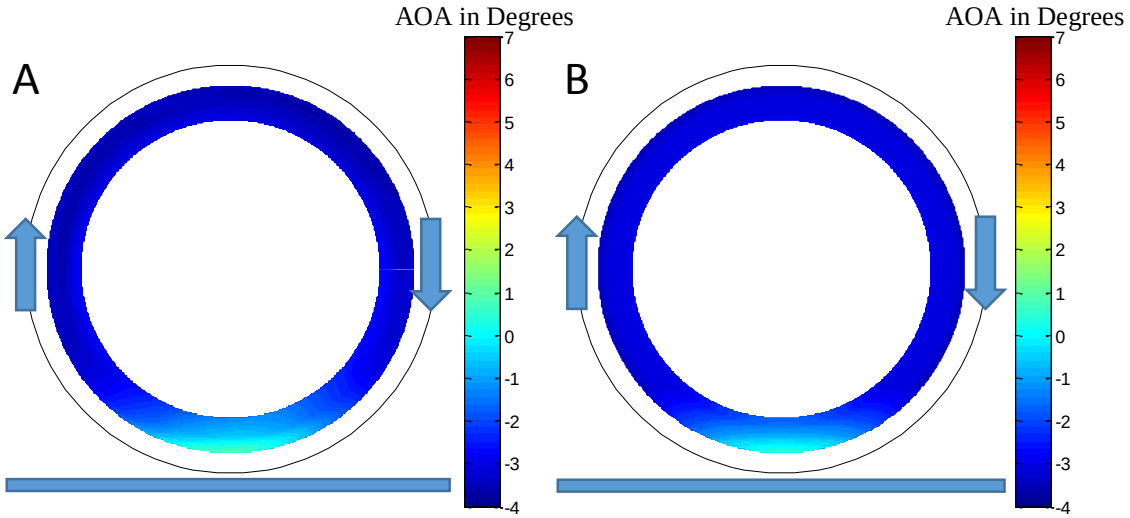

Figure 20: The angle of attack as seen by the rotor blade distribution in the outer 20% of the blade radius obtained from A) measured hotwire data, and B) undistorted flow analysis
(J = 1.44, 1823 RPM, U_∞ = 20 m/s)

The distortion of the flow is distinctly visible in Figure 19a and Figure 19b from looking at the extema of their angle of attack values outside of the boundary layer. The measured angles of attack range from one to two degrees in the outer 20% of the blade radius, while the undistorted

angles of attack range from three to four. This angle of attack reduction is due to the flow being accelerated into the rotor face, causing an increase in streamwise velocity. This reduction in extrema from the undistorted theory is not visible in the zero thrust case shown in Figure 20 A and B. The reduction in angle of attack from the undistorted theory is almost nonexistent in comparison to the lightly thrusting case shown in Figure 19. This is due a reduction in the flow distortion caused from a significant reduction in thrust. Intuitively, there should be no distortion at all in the zero thrust condition as there is no net thrust, and no net momentum change imparted onto the fluid. The measured angle of attack distributions in Figure 19 and Figure 20 both show strong angular uniformity, except when the rotor blades enter the boundary layer. For both the thrusting and zero thrust conditions, there is a sharp increase in measured angle of attack that is strongest at the blade tips. This contrasts with the theoretical angle of attack distributions, which have a more gradual increase in angle of attack in the boundary layer that has its maximum effect further away from the blade tips. Both the qualitative and quantitative effects of flow distortion on the out 20% of the angle of attack distribution of the rotor can be better determined by examining the angle of attack seen by a single radial position.

Figure 21 and Figure 22 both show angle of attack distributions seen by the rotor blade chord for both undistorted flow and measured distorted flow. These distributions were done at both 80% rotor radius in Figure 21a and Figure 22a, and at 98.5% rotor radius in Figure 21b and Figure 22b. The *x*-axis shows the angular position of the rotor blade, where 270 degrees corresponds to the bottom dead center rotor position closest to the wall shown in Figure 17. The direction in which the rotor blades move corresponds as right to left in Figures 21 and Figure 22. The rotor downstroke into the boundary layer is to the right of the bottom dead center line, and the rotor upstroke out of the boundary layer is to the left of the bottom dead center line.

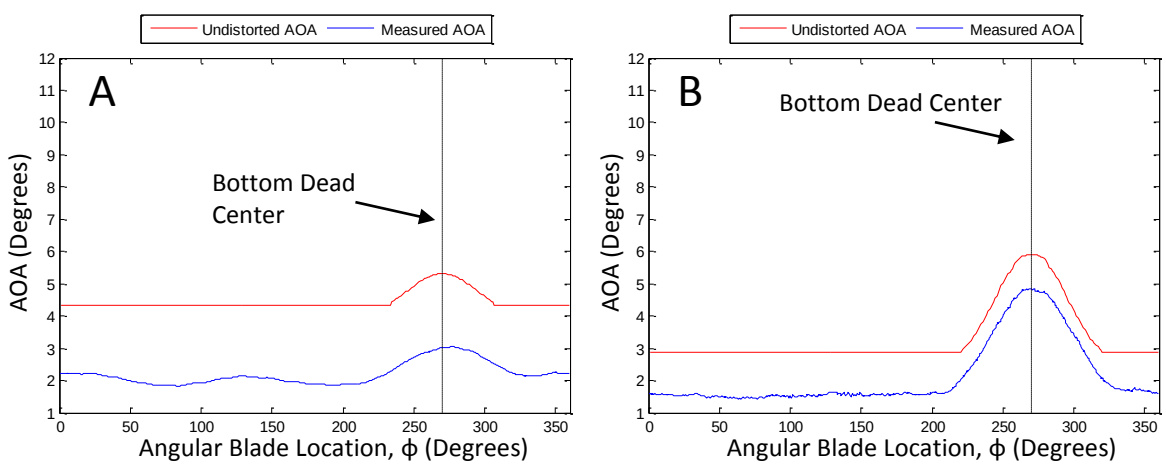

Figure 21: Angle of attack distributions for the rotor at 20 m/s, 2500 RPM, and J = 1.05 at A) 80% blade radius, and B) 98.5% blade radius

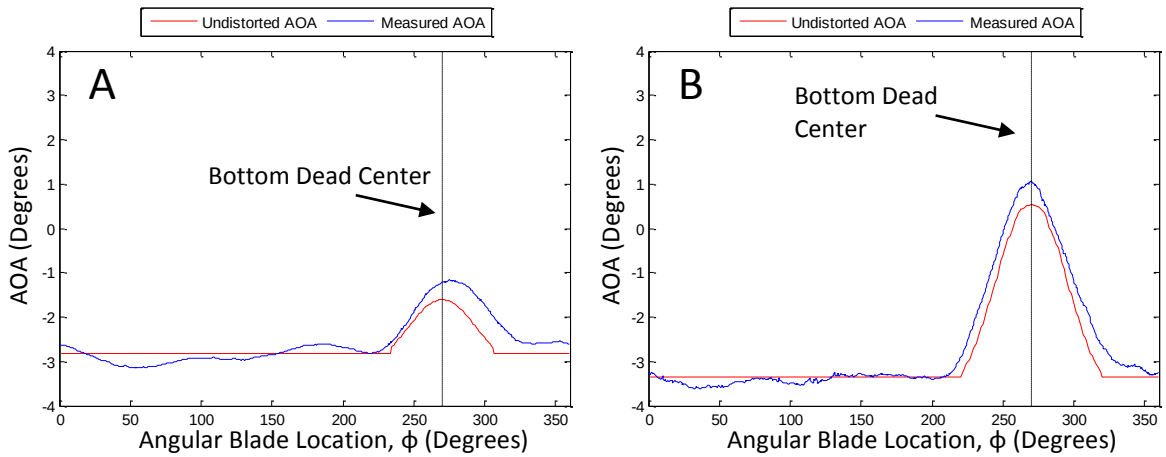

Figure 22: Angle of attack distributions for the rotor at 20 m/s, 1823 RPM, and J = 1.44 at A) 80% blade radius, and B) 98.5% blade radius

Figure 21 shows the angle of attack distributions at 80% radius and 98.5% radius for the lightly thrusting, J = 1.05 rotor condition. Both the 80% and 98.5% angle of attack distributions show strong qualitative agreement, having a sharp increase in angle of attack as the rotor enters the boundary layer, and a constant distribution around the rest of the rotor disk plane. Each of the radial positions seem to have a constant angle of attack offset due to flow distortion. The 80% measured angle of attack is roughly 2 degrees lower than predicted with undistorted flow. This is expected as flow acceleration due to the thrusting rotor will result in a decrease in angle of attack. The 98.5% angle of attack distribution also has a constant angle offset, but it is significantly less. The measured angle of attack distribution is roughly 1.5 degree lower than the predicted undistorted angle of attack distribution. This indicates the flow distortion is skewed away from the blade tips. This does not imply that the distortion will continue to increase as the radial position becomes close to the hub as the measurement volume was limited to the outer 20% of the rotor disk plane.

Figure 22 similarly shows angle of attack distributions at 80% radius and 98.5% radius for the zero thrusting, J = 1.44 rotor condition. The 80% and 98.5% angle of attack distributions also show strong qualitative agreement, having a sharp increase in angle of attack as the rotor enters the boundary layer, and a constant distribution around the rest of the rotor disk plane. The measured 80% radius angle of attack distribution is a barely varies from the undistorted angle of attack distribution. At most, it is half of a degree higher than the undistorted distribution. The measured 98.5% angle of attack distribution similarly shows quantitative agreement with the undistorted theory. This improved agreement with the undistorted theory is due to the reduction in distortion at the zero thrust condition. This condition by definition should minimally distort the flow, making undistorted predictions more accurate.

Both Figure 21a and Figure 22a show shifted measured angle of attack distribution about the bottom dead center towards the downstroke side. The lightly thrusting condition shows a 7 degree shift, and the zero thrust condition shows a 6 degree shift. This is similar to the results found in Alexander *et al.* (2014), where the upwash fluctuations were also found to be skewed towards the rotor blade downstroke. This would create asymmetry about the bottom dead center as a trailing blade in the downstroke side of the boundary layer would always have a leading blade interacting with the boundary layer, while a trailing blade in the upstroke side would not. This shift, interestingly, is not visible at the 98.5% radial location. This may be due to 3 dimensional effects mitigating the blade flow field interactions near the blade tips.

As the thrust increases, the same phenomena shown in the lightly thrusting case is visible. Shown below are the 80% and 98.5% radius angle of attack traces for a 15 m/s, 2500 RPM, J=0.79 rotor condition. Similar to Figure 21 and Figure 22, Figure 23 represents the blade motion as right to left, with the x-axis showing angular positon, and the y-axis showing the angle of attack seen by the rotor blades. The red line represents the calculated undistorted angle of attack, and the blue line represents the measured angle of attack distribution. Figure 23a shows the angle of attack distribution at 80% of the blade radius, and Figure 23b shows the angle of attack distribution at 98.5% of the blade radius. Just like in the lightly thrusting case, the J=0.79 condition at 80% blade radius shows that the angle of attack increases in the boundary layer, and then decreases to a somewhat constant level in the free stream. However, in this higher thrust case, the difference between the angle of attack seen in the boundary layer is closer to the distribution seen in the free stream. The rotor seems to be distorting the flow enough to alter the normal velocity gradient in the boundary layer. There is also a shift towards the downstroke side of about 8 degrees. Like the J=1.05 case, this J=0.79 condition shows qualitative agreement between measured angle of attack distribution and the calculated undistorted angle of attack distribution with a constant shift in angle of attack due to flow distortion. The measured 80% angle of attack distribution is roughly 3.5 degrees lower than predicted. This is 1.5 degrees more than the 2 degree offset found in the lightly thusting case shown in Figure 21a. The 98.5% angle of attack distribution is also lowered due to distortion, but by 2 degrees. Like the lightly thrusting case, there is also no visible shift in the angle of attack distribution about the bottom dead center line at 98.5% radius.

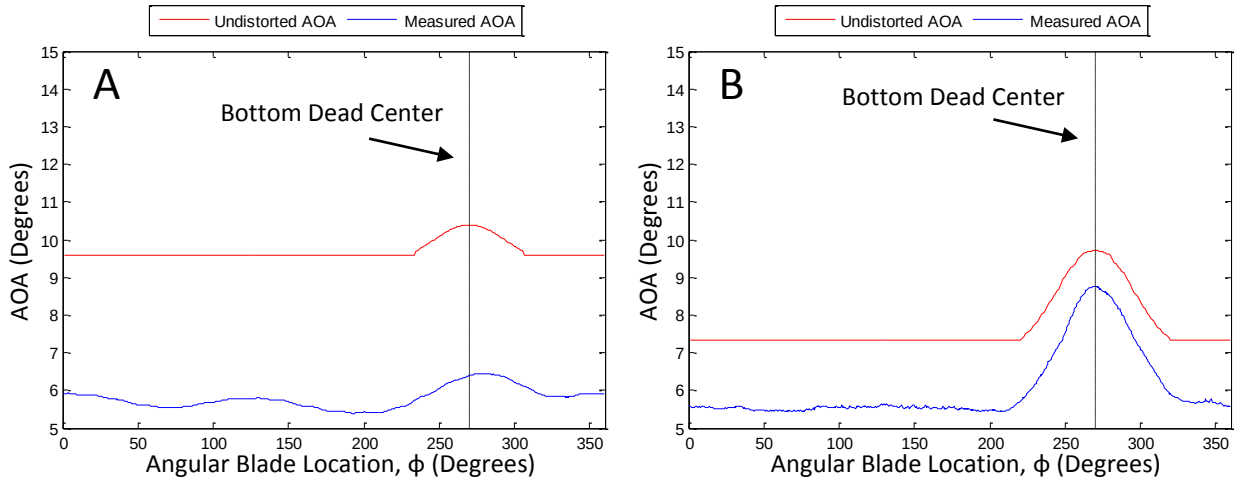

Figure 23: Angle of attack distributions for the rotor at 15 m/s, 2500 RPM, and J = 0.79 at A) 80% blade radius, and B) 98.5% blade radius

Altering the advance ratio from 1.44 to 0.79 produced qualitatively similar angle of attack distributions. The reduction in measured angle of attack from the predicted angle of attack distribution increased due to distortion as the thrust increased. However, this pattern does not continue as the advance ratio is lowered to regimes previously found to have strong flow reversal. Shown below is the 80% and 98.5% radius angle of attack traces for a 10 m/s, 2500 RPM, J=0.53 rotor condition known from Alexander *et al.* (2014) to have a strong region of flow reversal in the blade tip gap.

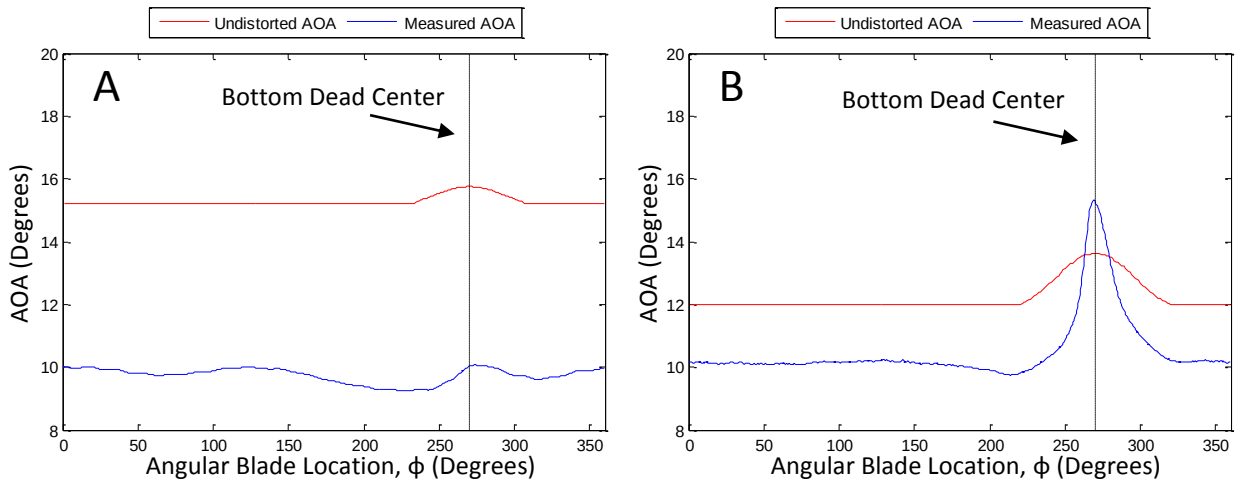

Figure 24: Angle of attack distributions for the rotor at 10 m/s, 2500 RPM, and J = 0.53 at A) 80% blade radius, and B) 98.5% blade radius

The highly thrusting, J=0.52 condition's measured angle of attack distribution at 80% radius shown in Figure 24 differs qualitatively from the higher advance ratio's 80% measured angle of attack distributions. There is no longer a visible difference as the blades enter the boundary layer, as the flow velocity at 80% radius in the boundary layer has been distorted to be equal to the rest of the rotor disk plane. The measured angle of attack distribution is also 5 degrees lower than predicted due to distortion. However, at 98.5% rotor radius, the measured angle of attack distribution changes completely from higher advance ratio 98.5% radius conditions. The angle of attack seen by the rotor still increases near the bottom dead center line, but the width of the response is very narrow, indicating it is not boundary layer driven. The measured angle of attack distribution also becomes higher than the predicted values near the bottom dead center line. This is due to a reduction in streamwise velocity that would not be caused by the normal streamtube contraction into a rotor face. This region of low velocity flow is most likely due to the interaction of the rotor blades with propeller hull flow reversal. A strong jet of flow reversal is present in the tip gap due to the "Pirouette Effect," causing a reduction of velocity at the blade tips.

3.2 TIME AVERAGED ROTOR SOUND FIELD

Figure 25 shows the noise spectra recorded at an inflow free-stream velocity of 20m/s for various rotor RPMs as measured by microphone 4 which has a directivity angle of 53º. This microphone was chosen because it is the microphone that is closest to the rotor axis that is in the anechoic chamber. The conditions in Figure 25 were chosen to give a variation from lightly thrusting rotor conditions to heavily thrusting rotor conditions. These heavily thrusting rotor conditions are known to experience flow reversal from Alexander *et al.* (2014). The flow speed was chosen to be 20 m/s as this velocity has the best range of lightly thrusting to heavily thrusting advance ratios. Rotor RPM is characterized in terms of advance ratio J, defined as the free stream velocity divided by the rotor rate of rotation in Hz multiplied by the rotor diameter. Figure 25a compares the background noise to the measured rotor noise, while Figure 25b compares the noise measured from each rotational velocity by normalizing the spectra on the tip velocity to the fifth power, which is a common propeller noise scaling, and the blade passage frequency (BPF). In Figure 25b, the background noise has been subtracted out for each case.

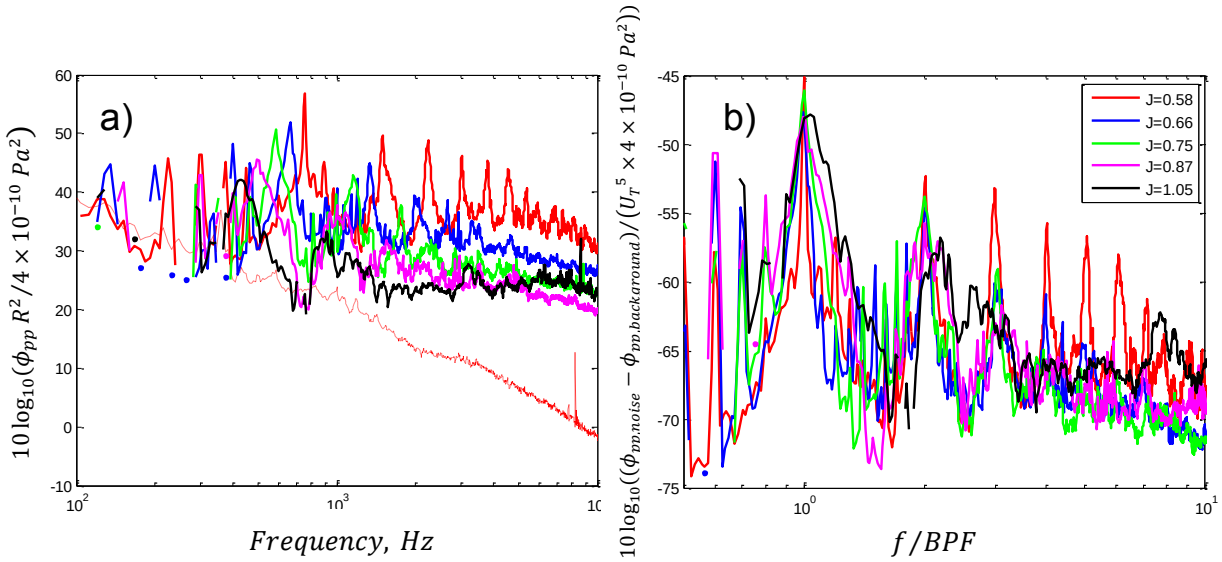

Figure 25: Rotor noise at U_∞ = 20m/s for various advance ratios J a) compared to background noise b) and normalized on the tip velocity and BPF

From these spectra, the effect of increasing the thrust is displayed as a narrowing of the haystacks around the BPF and an increased number of haystacks, but there are also some other phenomena present in these spectra. Below the BPF, noise spikes at multiples of the shaft rotational frequency exist. The peaks at f/BPF of 0.6, 0.7 and 0.8 are especially prominent. The high frequency lump in the J = 1.05 case near f/BPF of 8 appears to be due to vortex shedding from the blade trailing edges as discussed in the study by Hersh *et al.* (1974) for airfoils at low angles of attack. The calculated zero-thrust advance ratio for this rotor is 1.44. Therefore, at J = 1.05, the span of the rotor blade is at a slight angle of attack in the free stream. Of course, the angle of attack along the blade span varies as the rotor dips through the boundary layer. This is confirmed from examining the measured angle of attack for this condition shown in Figure 19 where the majority of the outer 20% of the disk plane is at a 2 degree angle of attack, and increases to 3 degrees in the boundary layer.

At advance ratios of 1.05 and 0.87, there are three distinct haystacking peaks at or above the blade passage frequency. This increases to four as the advance ratio is lowered to 0.75, and continues to increase to five at an advance ratio of 0.66. At an advance ratio of 0.58, there are nine distinctly visible haystacking peaks at or above the blade passage frequency. Because of the stochastic nature of the relatively short interactions of turbulent eddies with the rotor, only a few haystacking peaks at blade passage frequency harmonics should be visible. However, the increased number of visible peaks as the advance ratio is lowered indicates that the blade passage response may be becoming more correlated, or tonal.

The haystacks are also right weighted at higher advance ratios. This is made apparent by viewing the spectra on a linear *x*-axis and a closer view near the 1st blade passage frequency, as shown in Figure 26. This right shift is clearly visible in the lightly thrusting, *J*=1.05 condition denoted by the black line. The clear haystack narrowing with a reduction in advance ratio is also more apparent. The reason for this shift is diagramed in Figure 27. Haystacking noise is produced by the correlated loading of rotor blades as they slice through coherent structures. Consider two coherent structures of the same size that are inclined in different spanwise directions in relation to the rotor (red and blue) that exist in the boundary layer. These structures are then ingested by the rotor, and the blades slice them as a function of time and spanwise location. The response produced by the blue structure shown in Figure 27 will be at a frequency slightly higher than the BPF while the red is slightly lower than the BPF. However, the blue structure is cut more times. This increases the broadband noise produced by the blue structure as opposed to the red. This bias produces the right skewed haystacks at high advance ratio. As thrust is increased and the rotor begins to stretch the turbulence into its disk plane, the inclination angles of the coherent structures are reduced eliminating the right skew.

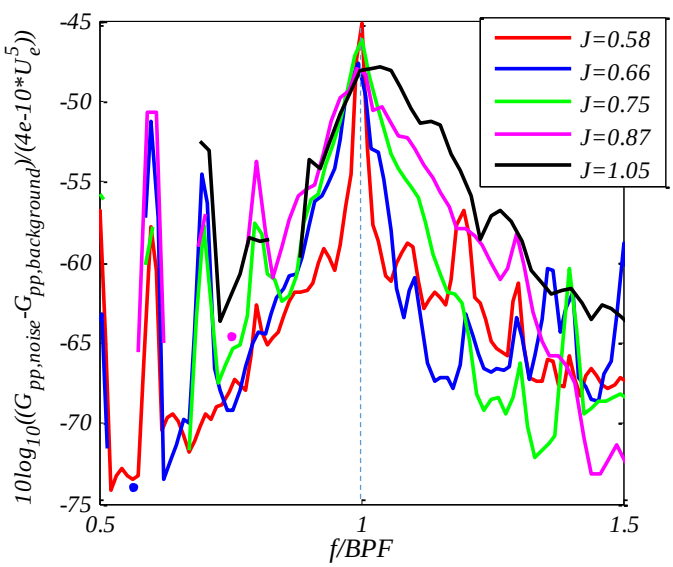

Figure 26: Rotor noise at U_∞ = 20m/s for various advance ratios *J* normalized on the tip velocity and BPF and plotted on a linear *x*-axis to better view asymmetry about the 1st BPF.

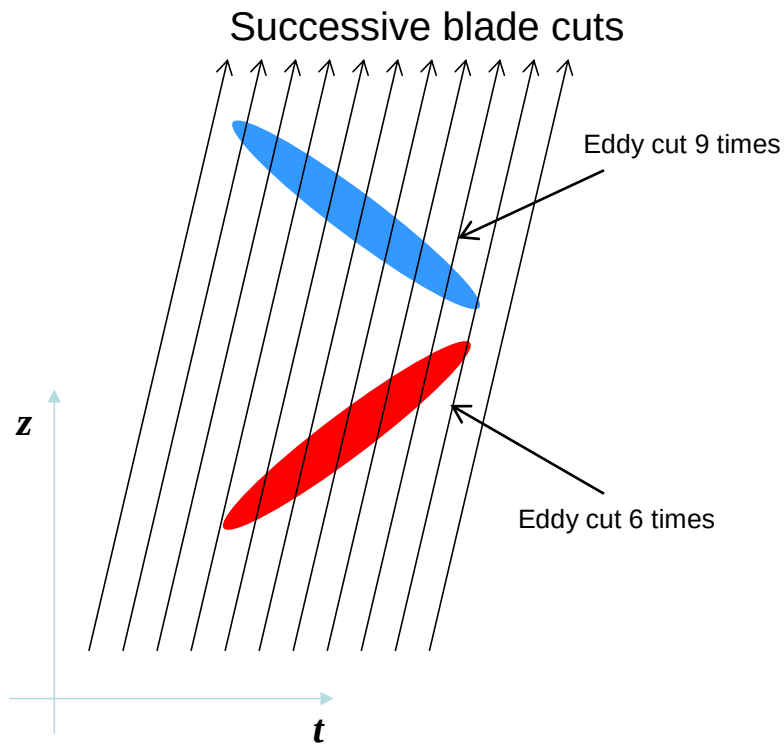

Figure 27: Diagram of explanation of right-skewed haystack at high advance ratios

Measurements were made at multiple receiving angles to the rotor axis to determine the directivity of the haystacking noise. Leading edge noise has dipole directivity which is shown below in Figure 28. It is cosine weighted towards the lift normal vector and has a null at 90 degrees. However, in this study, a wall is present. In order to predict the attenuations in the far field due to directivity, the haystacking sound source must be modeled to include an in phase reflected rotor across the hard wall. A diagram of this complex sound source is shown below in Figure 29. The observer location in line with the rotor source location is location 1, while any other observer location is location 2. The distance from the rotor source location to location 1 is r_1, and the distance from the reflected rotor source location to location 1 is r_1'. The distance from the rotor source location to location 2 is r_2, and the distance from the reflected rotor source location to location 2 is r_2'. The angle from the reflected rotor source to the observer at location 1 is θ_1'. The angle from the rotor source to location 2 is θ_2, and the angle from the reflected rotor source to location 2 is θ_2'. It is important to note that location 1 is at a zero degree angle from the rotor source location.

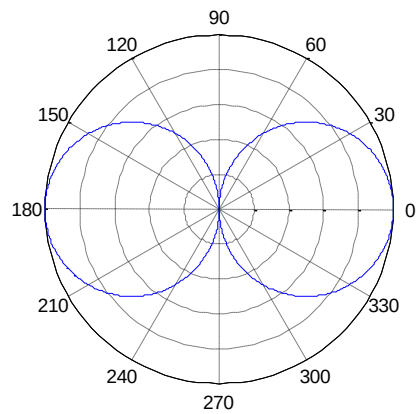

Figure 28: True dipole sound source directivity

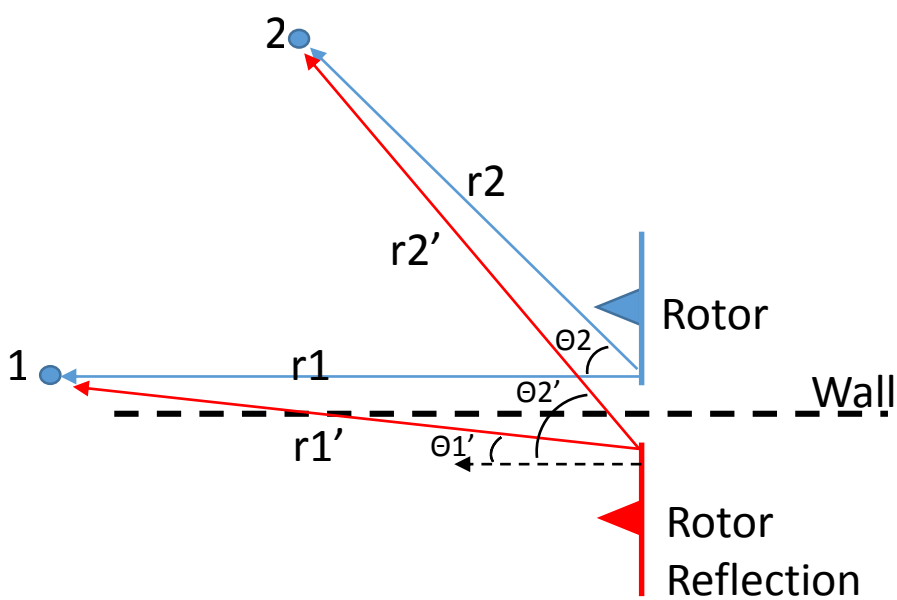

Figure 29: Complex reflected dipole sound propagation diagram

The equation for the far field pressure for a dipole takes the following form,

$$P = \frac{A*\cos\theta*k}{r} e^{i\omega t - ikr} \tag{6}$$

where A is determined from initial conditions, θ is the off axis directivity angle, k is the acoustic wavenumber, and ω is frequency. To combine two in–phase dipoles separated by a fixed distance, the far field pressure equation takes the following form.

$$P = \frac{A*\cos\theta*k}{r} e^{i\omega t - ikr} + \frac{A*\cos\theta\prime*k}{r\prime} e^{i\omega t - ikr\prime} \tag{7}$$

Simplifying, along with knowing $r' = r + \Delta r$ yields

$$P = Ake^{i\omega t - ikr}\left(\frac{\cos\theta}{r} + \frac{\cos\theta\prime}{r\prime}e^{-ik\Delta r}\right) \tag{8}$$

The root mean square of pressure now takes the form,

$$P_{rms} = \frac{Ak}{\sqrt{2}}\left(\frac{\cos\theta}{r} + \frac{\cos\theta\prime}{r\prime}\cos\left(\frac{2\pi\omega\Delta r}{c}\right)\right) \tag{9}$$

where c is the speed of sound. The attenuation relative to reference point 1 is simply

$$\Delta SPL = 20\log_{10}\left(\frac{\overline{r_2}P_{2rms}}{\overline{r_1}P_{1rms}}\right) \tag{10}$$

where $\bar{r}$ is the average of the observer distance from the source location and the observer distance from the reflected source location. This attenuation simplifies to

$$\Delta SPL = 20\log_{10}\left(\frac{\overline{r_2}\left(\frac{\cos\theta_2}{r_2} + \frac{\cos\theta_2'}{r_2'}\cos\left(\frac{2\pi\omega\Delta r_2}{c}\right)\right)}{\overline{r_1}\left(\frac{\cos\theta_1}{r_1} + \frac{\cos\theta_1'}{r_1'}\cos\left(\frac{2\pi\omega\Delta r_1}{c}\right)\right)}\right) \tag{11}$$

To more easily determine the effects of uncertainty in Δr, the observer distance to Δr ratio was assumed to be large, such that $r \approx r'$ and $\theta \approx \theta'$. However, Δr does not approach zero because it is in the term that determines the phase difference between the dipole and the reflected dipole. In this term, only the absolute difference in observer distance, not relative difference is relevant. This approximation, as well as noting $\theta_1 = 0$ yields

$$\Delta SPL = 20\log_{10}\left(\frac{\cos\theta_2\left(1+\cos\left(\frac{2\pi\omega\Delta r_2}{c}\right)\right)}{1+\cos\left(\frac{2\pi\omega\Delta r_1}{c}\right)}\right) \tag{12}$$

The uncertainty in ΔSPL due to Δr is now just

$$\delta\Delta SPL = \sqrt{\left(\frac{d\Delta SPL}{d\Delta r_2} * \delta\Delta r_2\right)^2 + \left(\frac{d\Delta SPL}{d\Delta r_1} * \delta\Delta r_1\right)^2} \tag{13}$$

where uncertainty in source location of half of an inch translates to a $\delta\Delta r$ value of 0.7 inches.

It is important to note that this uncertainty can become very large. However, it is easily seen from Equation 12 that the change in SPL cannot be greater than $20\log_{10}(2\cos\theta_2)$. This limits the upper bound of $\delta\Delta SPL$ to be $20\log_{10}(2\cos\theta_2)$- ΔSPL.

This analysis reveals that the true reflection affected directivity will strongly depend on the relationship between the acoustic wavelength and the difference in acoustic path lengths from the dipole source and reflected dipole source. As such, the expected attenuations due to a change in directivity are a function of frequency. The error also becomes increasingly large as frequency increases, quickly becoming many orders of magnitude higher than the directivity attenuations. Because of this, attenuation predictions are only reliable below 600 Hz. Shown below in Figure 30a, Figure 30b, and Figure 30c are the predicted attenuations with their uncertainties at 15º, 29º

and 53º, respectively. The 90º attenuation predictions are not shown because it is predicted to be -∞ dB for all frequencies. Shown on the *x*-axis is frequency in Hz, and shown on the *y*-axis is the predicted reduction in sound pressure level in decibels. For all directivity angles, the uncertainty becomes greater than 50 dB after 7000 Hz. However at 1000 Hz, the uncertainty is manageable at ±0.38 dB, ±0.61 dB, and ±0.92 dB at 15º, 29º, and 53º, respectively.

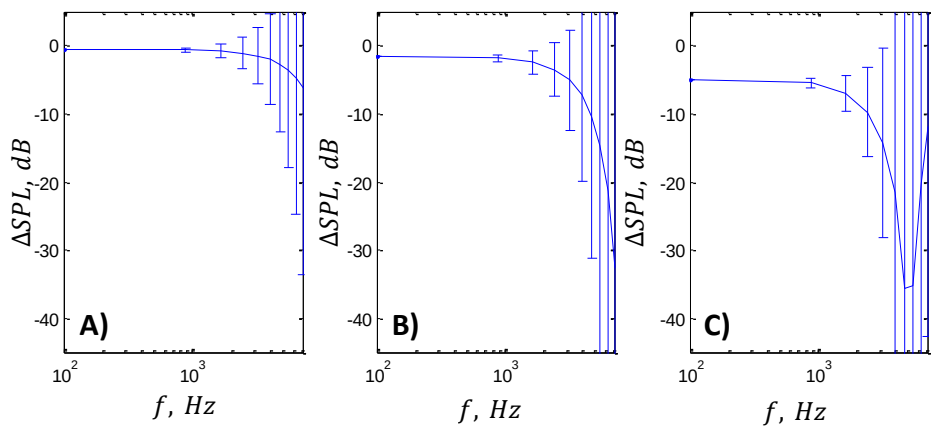

Figure 30: Predicted wall included attenuations due to directivity at A) 15º, B) 29º, and C) 53º

The measured directivity of the haystacking noise is shown in Figure 31 for different advance ratios. These conditions were chosen to show a variety of advance ratios. A zero thrust condition is shown in Figure 31a, a thrusting condition is shown in Figure 31b, and a heavily thrusting condition is shown in Figure 31c. Also, the conditions were chosen such that Figure 31a has the same RPM as Figure 31b, and Figure 31b has the same flow speed as Figure 31c. Shown on the *y*-axis is the sound pressure level normalized on the inverse of the observer distance as $10\,log_{10}(\phi_{pp}\,{r_m}^2/4 \times 10^{-10} Pa)$. In all cases, the broadband noise decreases towards the disk plane at 90º. Also shown below in Figure 32 are the expected attenuations from a constant 55 dB broadband source with dipole directivity and accounting for wall effects. The haystacking noise is not indicative of a true dipole source which would produce a null at 90º but has significant measured haystacking noise at this location due to blade twist. Because the noise source is a distributed dipole aligned normal to the chord line, this would prevent a directionality null. Besides the existence of noise at this position, the broadband noise also decays faster than would be expected by a dipole. Figure 32 predicts very small attenuations from zero degrees to 15 and 29 degrees that are less than 2 dB for frequencies less than 2 kHz. All thrust conditions in Figure 31 show more rapid attenuations across the spectrum. Figure 32 also shows a 53º attenuation of 5 dB. Measured attenuations show a 6-10 dB attenuation across the spectrum for all thrust conditions.

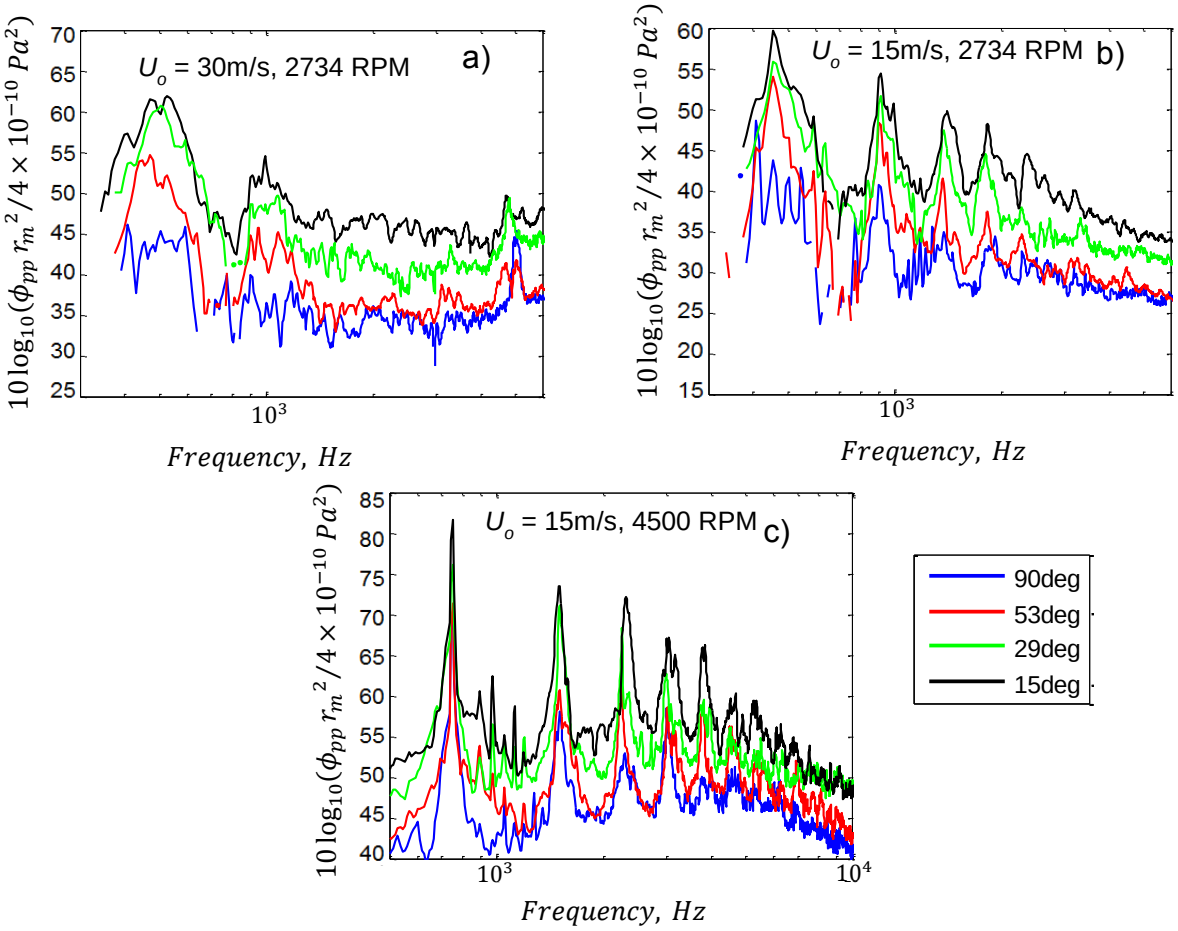

Figure 31: Directivity of noise at a) J=1.44, b) J=0.72, c) and J=0.44

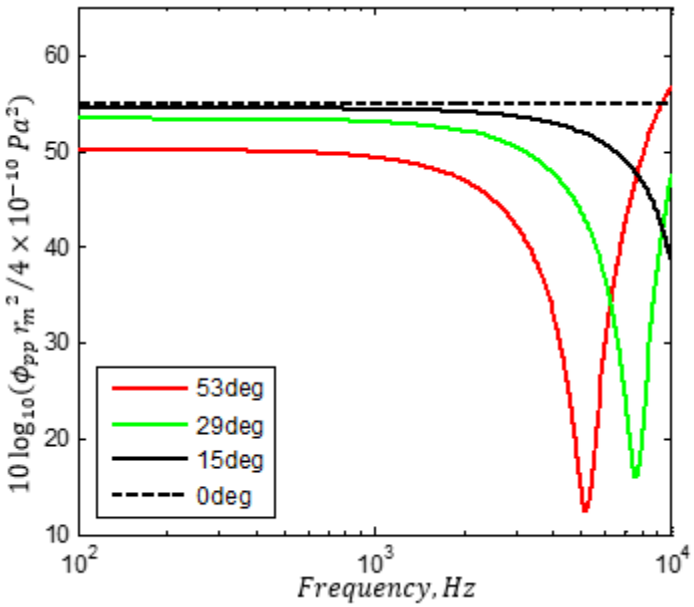

Figure 32: Expected directivity attenuation of from a broadband 55 dB dipole source with wall effects

To more precisely compare predictions to measurements, the BPF attenuations for the 2734 RPM, 15 m/s, J=0.72 will be directly compared to their predicted values. Accounting for the presence of the wall, predicted attenuations at 15º, 29º, 53º, and 90º at 456 Hz, or the BPF for a rotor operating at 2734 RPM, are -0.13 ± 0.08, -1.65 ± 0.13, -5.10 ± 0.19, and -∞ dB, respectively. With respect to 15º, the expected attenuations at 29º, 53º, and 90º are -1.52 ± 0.23, -4.97 ± 0.43, and -∞ dB, respectively. The measured 456 Hz attenuations with respect to 15º at 29º, 53º, and 90º on Figure 31a are -1, -7, and -17 dB, respectively. The 29º attenuation is close to predictions, but the 53º attenuation is larger, and the null at 90º was not measured. The measured 456 Hz attenuations with respect to 15º at 29º, 53º, and 90º on Figure 31B are -4, -6, and -15 dB, respectively. These attenuations are more rapid than predicted, except the null at 90º is not seen in measurements. This deviation from predicted attenuations and lack of a null at 90º is due to the blade twist in the rotor. This causes change in the direction of the lift vector along the rotor radius, causing the directivity to not be a true axially aligned dipole.

Figure 33 shows a contour plot of the frequency spectra measured at $\theta = 53º$ for a fixed rotational velocity and varying inflow velocity. Viewing the spectra and evolution of the noise this way helps to clearly identify the various sound sources and their features. Near advance ratios of 1 and 1.44, the trailing edge vortex shedding noise around 10kHz is at a maximum. Between these two advance ratios, the vortex shedding noise reduces creating a valley. The vortex shedding noise has a sharp cut-off below J = 0.9. As the advance ratio decreases, more haystacks gradually appear. At higher advance ratios, the right skew of the haystacks is clear particularly for the first and second harmonics which are present over the entire observed advance ratio range. In this figure,

the noise produced at multiples of the shaft frequency below the BPF are also easily observed and their peak strength decreases by 10dB from J=1 to J=0.5.

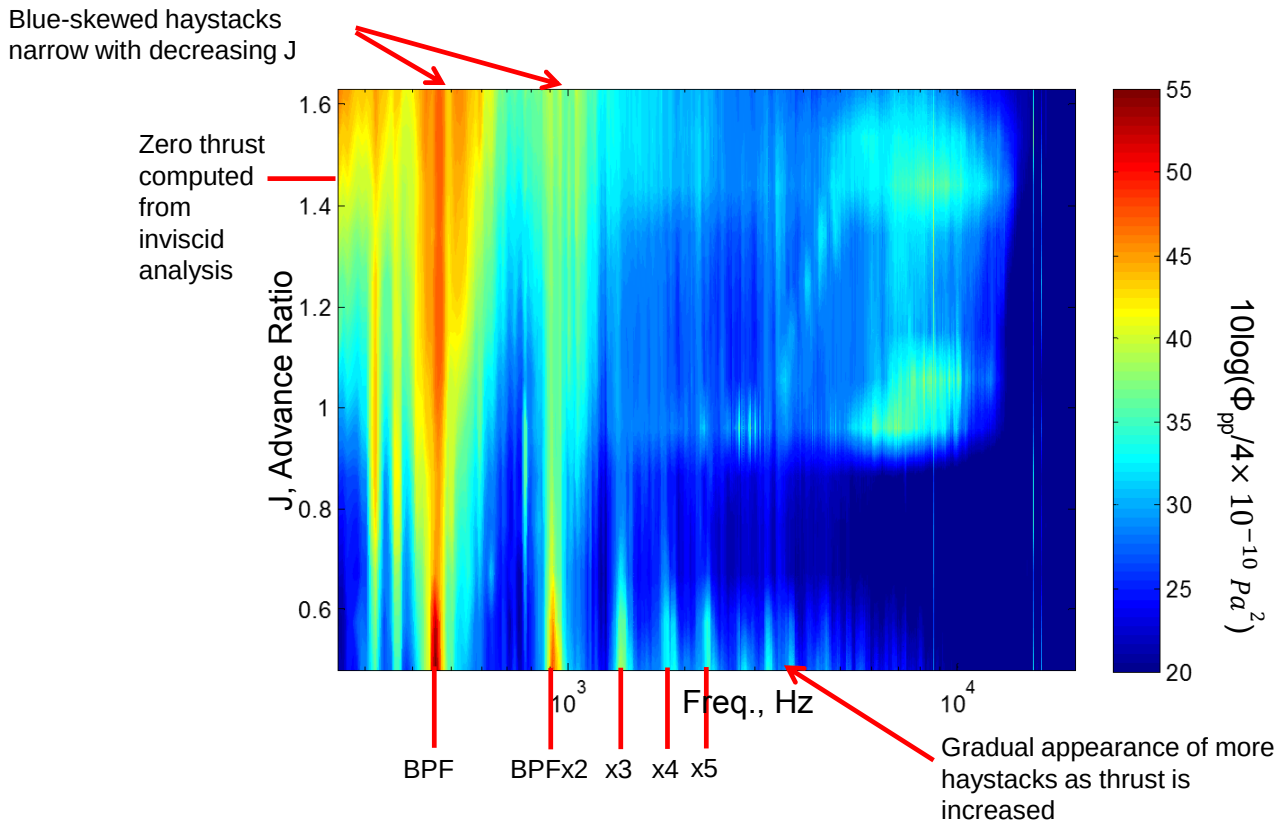

Figure 33: Contour of noise spectra over a range of advance ratios at fixed RPM of 2734 and varying inflow speed (measured at 53°)

Contours can also be plotted by holding the inflow velocity constant and varying RPM. Figure 34 shows fixed freestream velocity contours for as measured from microphone 4. The data from the four different inflow velocity conditions have been combined by normalizing the spectra on the tip velocity to the fifth power to produce single continuous contours. These contours extend from advance ratios of 0.3 to 1.9. The same features as observed in Figure 33 are observed here. The haystacks at multiples of the BPF appears as curved lines since they are no longer fixed frequencies and the vortex shedding noise around 10kHz appears again at higher J. Below an advance ratio of 0.5, the peaks at frequencies above the third BPF harmonic increase dramatically in intensity. Also, the low frequency humps at multiples of the shaft rotation frequency are again visible below the BPF.

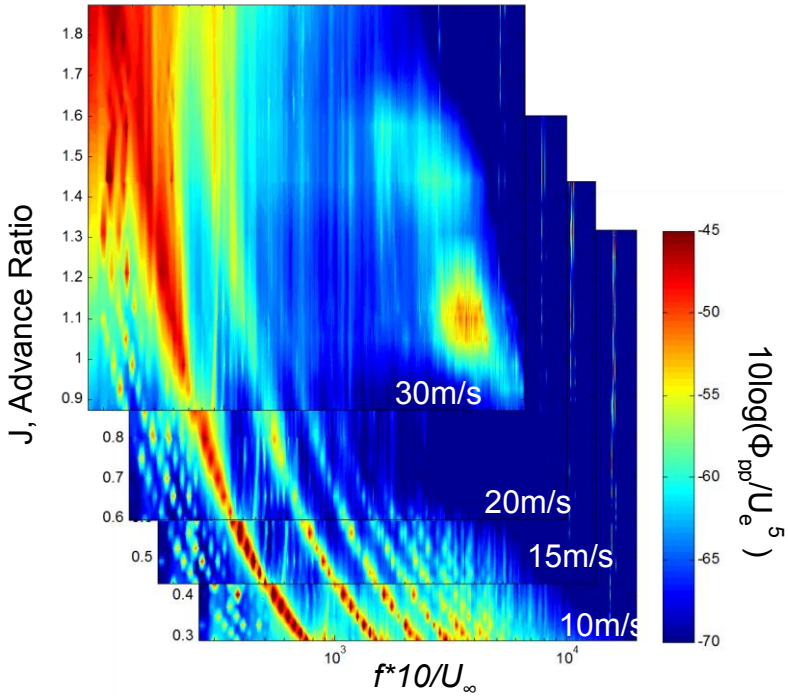

Figure 34: Combined contours of noise spectra over a range of advance ratios at fixed inflow velocities and varying RPM normalized on tip velocity for the 101 mm boundary layer (measured at 53°)

The noise associated with the haystacking peaks becomes partly tonal at low advance ratios. The coherence C_{Bp} of the blade clocking signal, B, with the acoustic pressure signal, p, for advance ratios of 0.32 to 1.57 was taken. This included flow speeds of 10, 20 and 30 m/s. The coherence is defined by Equation 14 below where ϕ_{Bp} is the cross-spectral density between the blade clocking and acoustic signals, ϕ_{BB} is the autospectral density of the blade clocking signal, and ϕ_{pp} is the autospectral density of the acoustic signal. The coherence at the blade passage frequency was taken and shown below in Figure 35.

$$C_{Bp} = \frac{|\phi_{Bp}|^2}{\phi_{BB}\phi_{pp}} \tag{14}$$

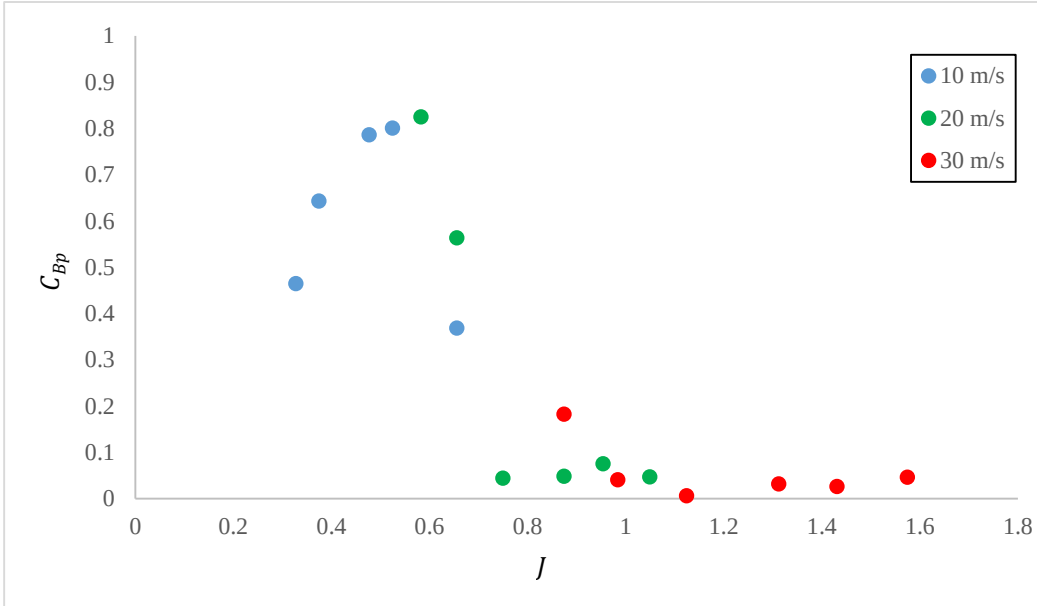

Figure 35: Coherence of acoustic signal at a 53° receiving angle with the blade clocking signal at the BPF

For advance ratios higher than 0.75, there was negligible coherence at the blade passage frequency. However, for lower advance ratios, the coherence at the blade passage frequency increases. The coherence reaches a maximum of 0.83 at an advance ratio of 0.58, indicating tonal noise contributed to 83% of the first BPF spectral hump. This suggests that the spectral humps at the first harmonic shown in Figure 34 and at low advance ratios have significant tonal contributions. As the advance ratio continues to decrease, the coherence also decreases to 0.45 at an advance ratio of 0.33. This is due to the rotor blades stalling, adding additional out of phase BPF contributions.

As stated previously Sato et al. (1986) characterized flow reversal due to rotor-hull interactions. They predicted that for the tip gap to rotor diameter ratio used in this configuration, 0.04, flow reversal would occur at a specific thrust parameter, K_T, greater than 2. This thrust parameter is related to the propeller thrust, T, rotor diameter, D, free stream density, ρ and free stream velocity, U according to Equation 15 below. The thrust was obtained from the non-dimensional thrust curve obtained using JavaProp shown in Figure 11. The coherence was re-plotted in Figure 36 below with an x-axis of K_T and the transition criteria emphasized with a dashed line.

$$K_T = \frac{8T}{\pi \rho D^2 U^2} \tag{15}$$

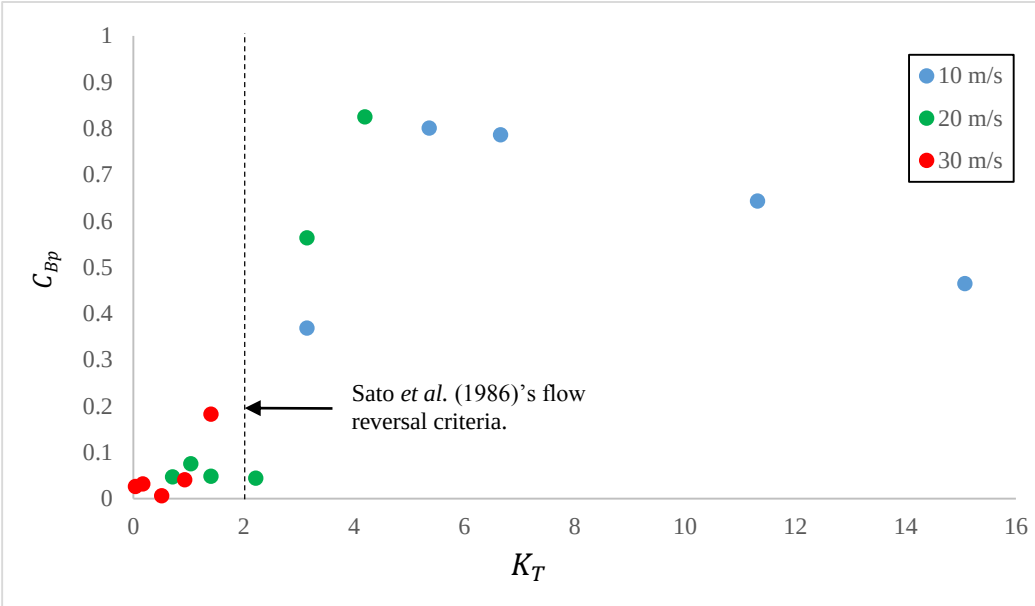

Figure 36: Coherence of acoustic signal at a 53º receiving angle with the blade clocking signal at the BPF plotted against Sato *et al.* (1986)'s thrust parameter.

3.3 Characteristics of the Turbulence as Revealed in the Sound Field

Subtle differences in the ingested turbulent structures responsible for the haystacking noise may be observed in the acoustic signals by using a detailed acoustic time signal analysis, extending that of Alexander *et al.* (2013). To better understand haystacking noise, the average acoustic response of an ingested eddy will be calculated. Eddies pass through the rotor disk plane at random intervals but produce a characteristic periodic response at the blade passage frequency. These eddy passages will be identified in the time series data and then averaged together.

A sample of the acoustic time series taken at a free stream velocity of 30 m/s and an RPM of 4000 recorded by microphone 5 at a receiver angle $\theta = 15^o$ is shown in Figure 37. The *y*-axis has units of Pascals and the *x*-axis is time normalized on the blade passage time. The *x*-axis shows fifteen units of time normalized on the blade passage frequency, corresponding to 0.0225 seconds. A smoothed line was fit to the signal using a local averaging filter about 20 points, and is shown in red. Indicated on Figure 37 is an area that has a clear response at the blade passage frequency. Note that the low frequency oscillation dominating the signal is due to tunnel fan noise. This looks similar to the burst signals observed in LDV measurements. Also indicated is an area believed to be indicative of more disorganized turbulence interaction. However, much of the time series is not labeled as it is unclear whether or not an acoustic response to an eddy passage is present. This demonstrates the importance of developing an objective method to determine the locations of significant eddy passages.

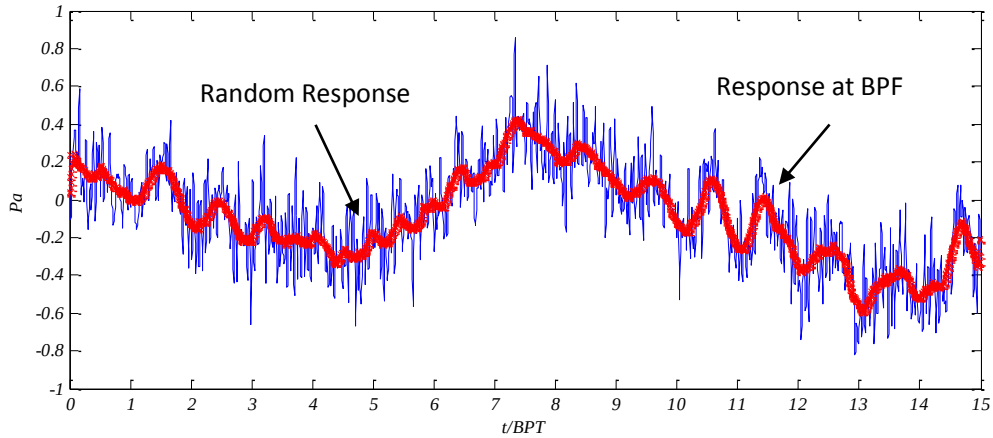

Figure 37: Time series of noise showing bursts as coherent structures are cut by successive blades (30 m/s, 4000 RPM, J = 0.98, $\theta_m = 14^o$)

A key goal of this study is to develop a method to determine the average acoustic response to an eddy passage. This was done by determining significant eddy locations in the time-frequency domain of the individual microphone signals, averaging this instantaneous signal across multiple microphones, and then time delay-averaging successive instantaneous signals to obtain a typical representation of the acoustic signal generated by eddy structures at a given rotor operating condition. These time delay averages were then used to estimate the typical timescales of the turbulent eddies. This analysis was performed for signals generated with the thin (101-mm thick) inflow turbulent boundary layer.

As a preliminary step, the relative time delays of the rotor acoustic signals received by each of the 8 measurement microphones shown in Figure 5 and Figure 6 were estimated. These time delays would be expected to be a function of the free stream velocity and microphone position, but not the rotor RPM. The time delays were determined relative to microphone 5's signal, since this had the highest signal to noise ratio and showed the clearest haystacking pattern at most conditions. In order to obtain more precise time delay signals relative microphone 5, the time-delay correlation coefficient function was computed with an initial time delay guess of the expected time delay. The correlation function is shown below in Equation 16, where p_i represents the acoustic pressure measured by the ith microphone.

$$corr = \frac{\overline{p_i(t)p_5(t+\tau)}}{\sqrt{\overline{p_i(t)^2}\,\overline{p_5(t)^2}}} \tag{16}$$

The time delay was determined to be the time to the largest peak on the correlation function, and compared with a convection model prediction. Amiet (1978) showed that refraction through a shear layer alters the affective acoustic path from the rotor to the microphone. This alteration is given by Equations 17 and 18 below where θ_m is the actual angle of the microphone to the rotor

axis consistent with Figure 5, Figure 6, and Table 3, r_m is the distance from the rotor to the microphone, h is the distance from the rotor to the shear layer, θ_c is the angle of the acoustic path from the rotor to the shear layer, and θ is the angle between the shear layer and the acoustic ray path after refraction. The only unknowns in Equations 17 and 18 are θ_c and θ. This is shown in Figure 38.

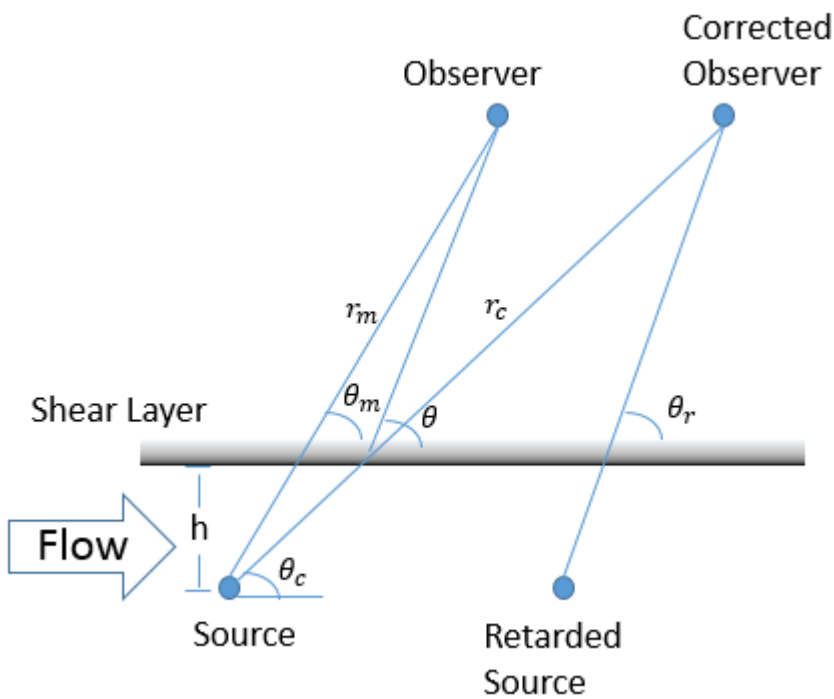

Figure 38: Diagram of acoustic path change through a shear layer (Notation from Amiet (1978))

The time delay calculation was carried out for assumed shear layer thicknesses of 10 and 20 cm in order to determine shear layer thickness effects. These time delays had values as high as 0.0026 seconds or 2 full blade passages as 4500 RPM. Note that

$$\tan\theta_c = \frac{\sqrt{(1-M\cos\theta)^2-(\cos\theta)^2}}{(1-M^2)\cos\theta+M} \tag{17}$$

$$r_m\cos\theta_m = h\cot\theta_c + (r_m\sin\theta_m - h)\cot\theta \tag{18}$$

These equations are simultaneously solved for the new acoustic path angle. Convection is then accounted for and the time delay with microphone 5 is determined. Figure 39 shows, as an example, the predicted and measured time delay for microphones 3 and 4 with microphone 5, in seconds assuming both 10 cm and 20 cm thick shear layers. The symbols represent time delay predicted utilizing the Amiet (1978) refraction model and accounting for convection, and the solid

lines represent the time delay measured using the autocorrelation function. For all cases, as flow speed increased, the time delay with microphone 5 decreased. The predicted and measured time delays agree to within 6%, validating the correlation function aided time delay alignment procedure.

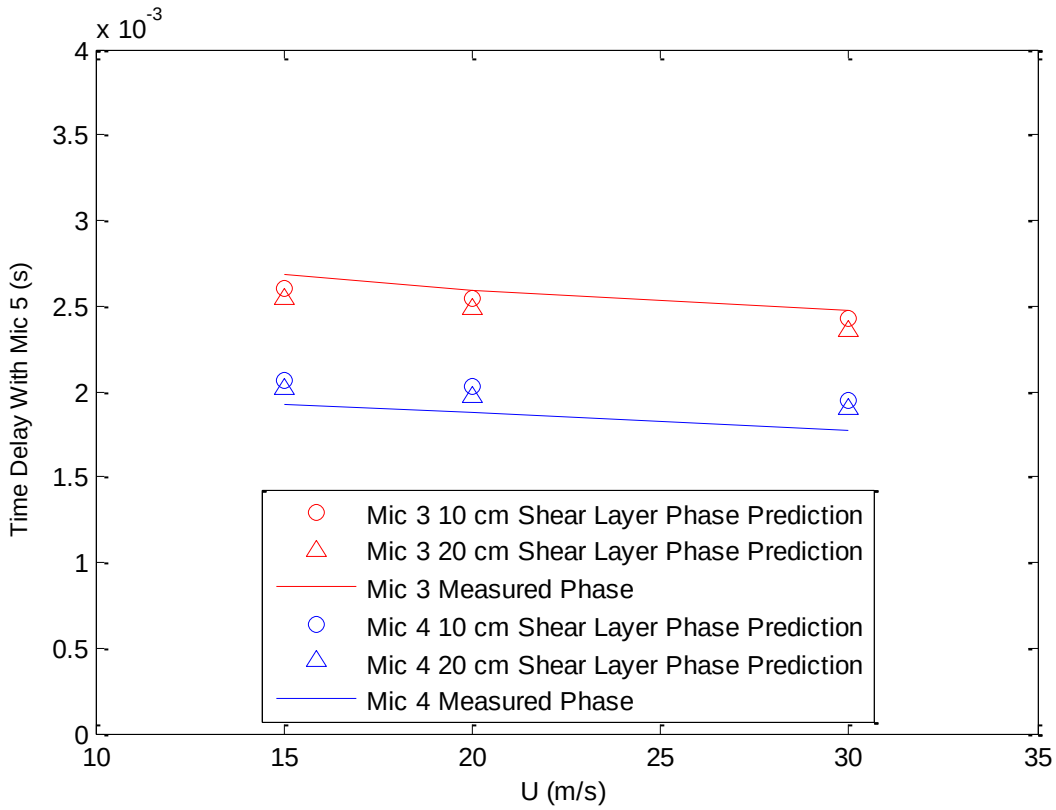

Figure 39: Measured and predicted full signal time delays of microphones 3 and 4 with microphone 5

3.3.1 Identifying eddy ingestion events in the acoustic signals

The microphone 5 signal was used for detection of eddy passages since this appeared to provide the best signal to noise ratio. First a 100 Hz high pass ideal filter was applied to filter out the tunnel fan noise. Note that the blade passage frequency was never less than 160Hz so this had no impact on the frequencies of interest in the signal. A short time Fourier transform was then computed for the signal and the value at the blade passage frequency was taken at every time to determine a the energy at the blade passage frequency as a function of time, with a 64Hz-bandwidth bin. The time window length of the STFT was thus 0.0156 seconds. This was chosen because it completely resolved the first two BPF haystacks for all analyzed rotor RPMs (2000-

4000). This time resolution corresponds to 5.2 and 10.4 blade passages for 2000 RPM and 4000 RPM, respectively.

Figure 40 shows a typical short-time Fourier transform sequence taken from one second of the 30 m/s 4000 RPM run. This run corresponds to an advance ratio *J* of 0.98 and a BPF of 667 Hz. Shown on the *x*-axis is the time in seconds and shown on the *y*-axis is the frequency normalized on the blade passage frequency. The short-time Fourier transform itself is in units of decibels normalized on 20μPa. Structure is visible in the time variation at the blade passage frequency that we believe is the result of the intermittent passage of coherent eddies through the rotor. The dark red structures indicate a higher amplitude acoustic response at the BPF, while the lighter yellow and green structures indicate lower amplitude, but still significant, acoustic responses at the BPF. One difficulty in interpreting this figure is that it is hard to distinguish individual eddies as they can be blurred together, perhaps due to simultaneous ingestion of multiple eddies.

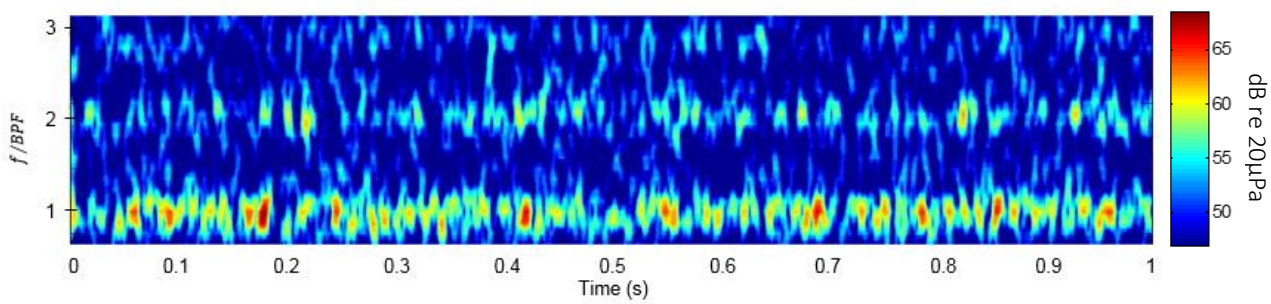

Figure 40: Short-Time Fourier Transform of acoustic signal ($U_\infty = 30m/s$, 4000 RPM, BPF = 667 Hz)

The wavelet transform $C(a,b)$ of the acoustic pressure signal was also used in an attempt to reveal the coherent structure content of the acoustic signals. The wavelet transform is defined by Equation 19 below where *p(t)* is the acoustic pressure, *a* is a scale and *b* is a time shift that alters the frequency and center time of a mother wavelet, φ. The real valued Morlet wavelet was determined to closely resemble the expected character of an eddy acoustic signature and was used as the mother wavelet. The real valued Morlet wavelet is a cosine wave localized by a Gaussian window and is shown below in Equation 20.

$$C(a,b) = \int_{-\infty}^{\infty} p(t) \frac{1}{\sqrt{a}} \varphi\left(\frac{t-b}{a}\right) dt \tag{19}$$

$$\varphi = \frac{1}{\sigma\sqrt{2\pi}} e^{\frac{-t^2}{2\sigma^2}} \cos(t) \tag{20}$$

Figure 41 shows the continuous wavelet transform for the time signal as Figure 40. The same period of time was used from the STFT, and the contour color map corresponds the wavelet transform coefficients, *C*, normalized to unity. Similar to Figure 40, Figure 41 shows visible structures at the blade passage frequency (667 Hz). However, it is less difficult to distinguish individual eddies. Visibly, the structures are narrower and have more distinct start and end times.

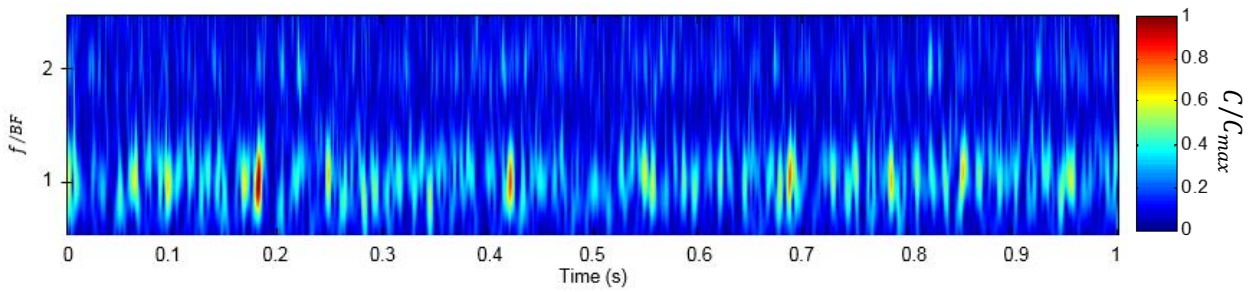

Figure 41: Continuous Wavelet Transform of acoustic signal $U_\infty = 30m/s$, 4000 RPM, BPF = 667 Hz)

Figure 42 shows the normalized traces of the short time Fourier transform and the continuous wavelet transform for Figure 40 and Figure 41, respectively, at the blade passing frequency. The STFT trace was converted back to a linear scale by obtaining the pressure auto spectral density, and then normalizing to unity. The trace obtained from the wavelet transform was normalized to match the scale on the STFT trace, and they were found to be almost identical. This indicates that the BPF trace obtained from either the short time Fourier transform and the continuous wavelet transform both provide an objective measure of the appearance of coherent bursts in the acoustic signal due to the ingestion of eddies. The continuous wavelet transform was used for the remaining analysis due to its prediction of more narrow peaks which allow for a more distinct eddy center. The wavelet transform's BPF trace also more frequently approaches zero, which will correspond to more distinct eddy passage start and end times.

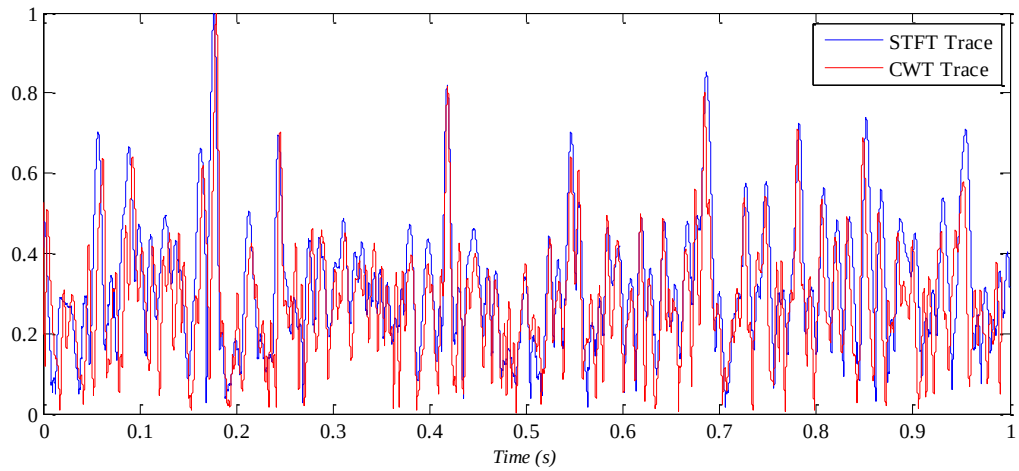

Figure 42: BPF traces of continuous wavelet transform and short time Fourier transform of acoustic signal ($U_\infty = 30m/s$ and 4000 RPM)

To obtain start and end times for eddy passages, the BPF traces of the continuous wavelet transform were analyzed. Traces were first smoothed by taking a local average of 0.008 seconds of data (512 samples) centered at each data point. This time was chosen such that it would cover at least 2.5 blade passages for the lowest RPM case analyzed. Every value below a discrimination level was then assumed to not contain a significant eddy acoustic signature. This discrimination level was set to a certain percentage of the mean trace value. Eddy passage start times were obtained from a trace's rise through the discrimination level and terminated by falling through the same level. The eddy center times were assumed to be halfway between the start and end times.

To determine the optimum discrimination level for the continuous wavelet transform analysis, the level was varied and the number of predicted eddy passages and total time in which an eddy passage occurs were plotted. Figure 44 shows the results of a typical discrimination level analysis performed on a single 10 second time record of data taken with a free stream velocity of 20 m/s and at a rotor RPM of 4000. Figure 44a shows the number of eddy passages detected as a function of the discrimination level. Discrimination level is plotted in terms of percentage of the mean spectral level at the blade passing frequency. Clearly, the higher the discrimination level is set, the fewer number of eddy passages is detected, but the variation is not smooth. This is because multiple eddies can pass through the rotor plane simultaneously, creating a local multiple hump shape in the BPF trace, which could actually increase the number of eddies detected as the discrimination level increased. This phenomena is shown in Figure 43 below. The wavelet transform BPF trace from Figure 42 is shown, with two discrimination levels. Three locations where raising the discrimination level will cause an increase in detected eddy passages are emphasized.

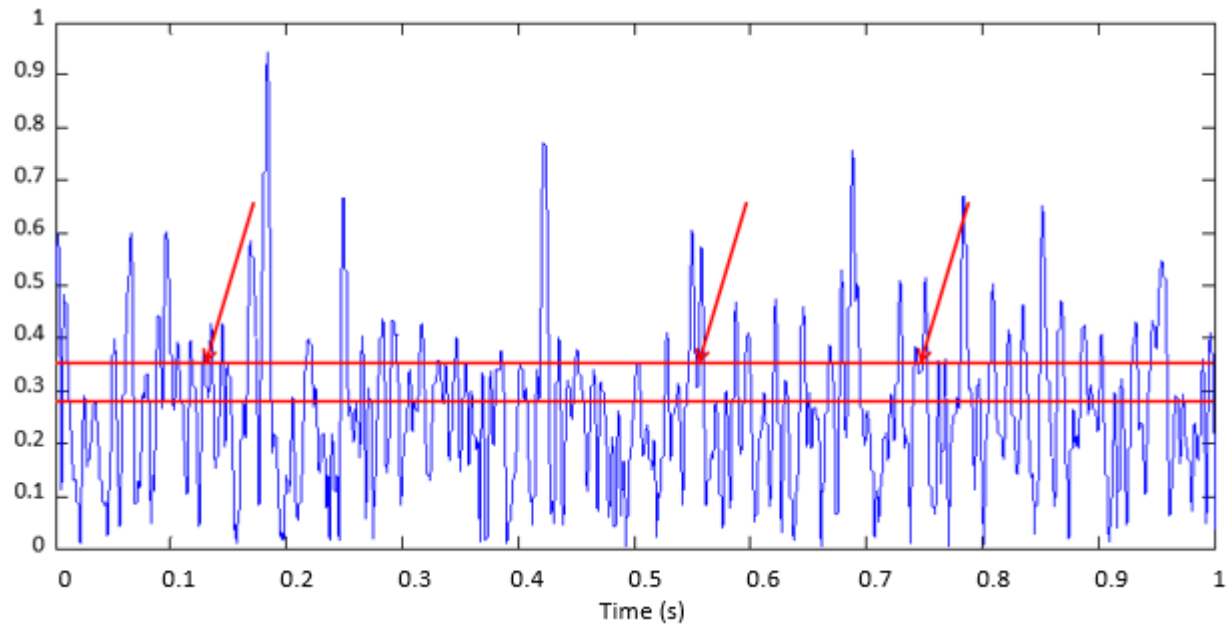

Figure 43: BPF trace of continuous wavelet transform and short time Fourier transform of acoustic signal with sources of non-smooth eddy quantification identified ($U_\infty = 30m/s$ and 4000 RPM)

Figure 44b shows the total time during which eddy passages are detected as a function of discrimination level. It is clear that the total eddy passage time smoothly decreases with increasing discrimination levels. The drop in eddy passage time is smooth because while a local double hump trace structure could increase the number of peaks with increasing discrimination level, the total time of eddy passage would still decrease. To determine the best discrimination level, the level was set at a local shelf point on the number of eddy passages plot. To objectively determine shelf points, the statistical elasticity of the number of passages with the total eddy passage time was computed. Equation 21 below shows the elasticity where T is the total eddy passage time, an N is the number of eddies detected. The statistical elasticity is a common parameter used in economic analysis. Hess (2002) describes it as the responsiveness of one variable to a change in a related variable. This is normally used to determine the response of demand to a change in price, but it was found that it also is useful for finding shelf points in the number of determined eddy plots. This corresponds to where a change in total number of eddies detected will be least affected by a change in total time of eddy passage.

$$E = \frac{dT}{dN}\frac{N}{T} \tag{21}$$

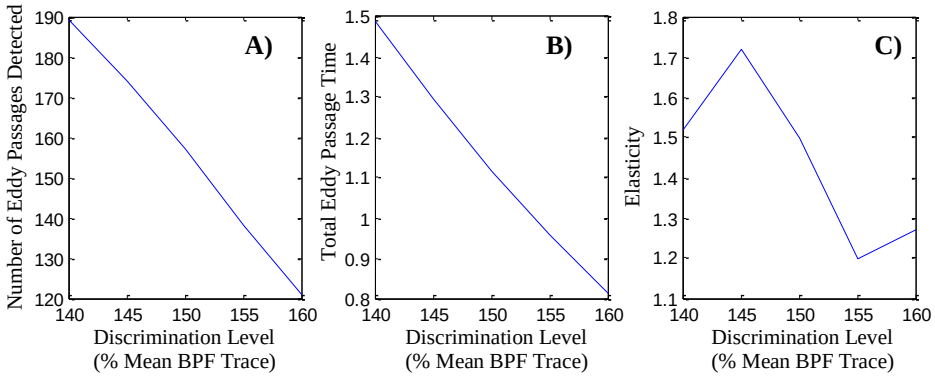

Figure 44: Effects of discrimination level on a) Number of eddies detected, b) Total time of eddy passage, and c) Elasticity of number of eddies detected with total time of eddy passage. (30 m/s, 4000 RPM)

Figure 44c shows the elasticity for each discrimination level. This result is not typical, in that the number of eddy passage signatures detected varied relatively smoothly with discrimination level. A local shelf point on Figure 44a cannot be visually identified. However, and elasticity peak of 1.7 was found at a discrimination level of 145% of the mean BPF trace, shown in Figure 44c. A more typical discrimination analysis for a 20 m/s, 4500 RPM condition is shown below in Figure 45.

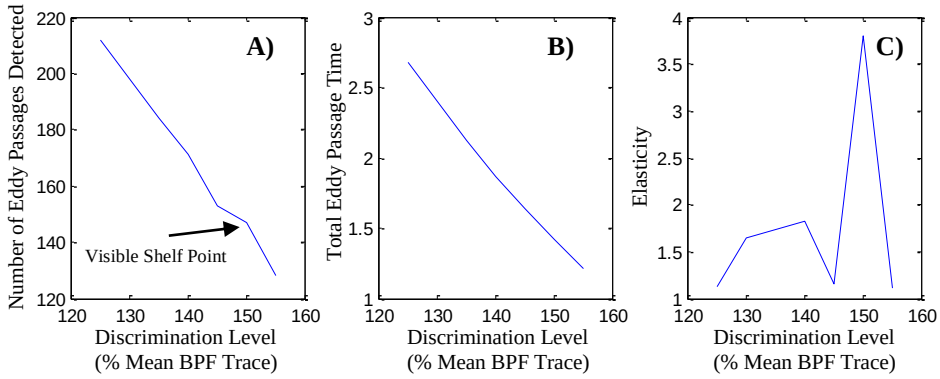

Figure 45: Effects of discrimination level on a) Number of eddies detected, b) Total time of eddy passage, and c) Elasticity of number of eddies detected with total time of eddy passage. (20 m/s, 3500 RPM)

A clear shelf point at a discrimination level of 150% is visible in Figure 45a. This corresponds to a clearly visible elasticity peak of 3.75 on Figure 45c. A similar procedure was used to determine the discrimination level for all other conditions.

3.3.2 Averaging the ingestion event acoustic signals

With the average time delay from each microphone relative to microphone 5, as well as the eddy passage center times from microphone 5, one should be able to locate the center times in the other microphones by simple time delay adjustments if every eddy passed through the rotor at the same location. However, turbulent eddies can pass through any part of the rotor disk plane immersed in the boundary layer and there will be small time delay differences. Thus, further time delay alignment is necessary. The short time local correlation function was computed for each eddy passage signal detected in the microphone 5 acoustic trace, with the corresponding signals in the other measurement microphones to determine the time delay for each eddy passage. The signal bounds on the short time local correlation function was set to 0.022 seconds. This was chosen because it is an order of magnitude higher than the highest expected time delay difference with microphone 5. It also corresponds to 7.3 blade passages for 2000 RPM cases and 14.7 blade passages for 4000 RPM cases. These bounds were large enough to encompass the majority of an eddy structure, but not so large that multiple eddies would be encompassed. This data was used to create histograms of the time delay between eddy detection events in different microphones. Figure 46 shows a typical histogram, showing the time delay between eddy passage events in microphone 5 and microphone 8 for a rotor RPM of 4000 and flow speed of 20 m/s. The histogram is assembled from a single 4 second-long time record. Shown on the *x*-axis is the deviation of the individual eddy time delay from the average time delay. The y-axis shows the number of eddies that had a particular time delay. It can be seen that a majority of the eddy passage time delays were equal to the average time delay, but some could vary by as much as 0.28 milliseconds or by 0.18 blade passages. Some attempt was made to use the time differences between the microphone signals determined in this way to locate in space the location of the eddy impact on the rotor disc. It was found that while the range of time delays observed was consistent with the eddy impacts in different positions on the rotor, the uncertainty of the position determination was too large to be useful. However, this could be done in the future with a larger array of microphones including microphones located well out of the *x-z* plane containing the rotor.

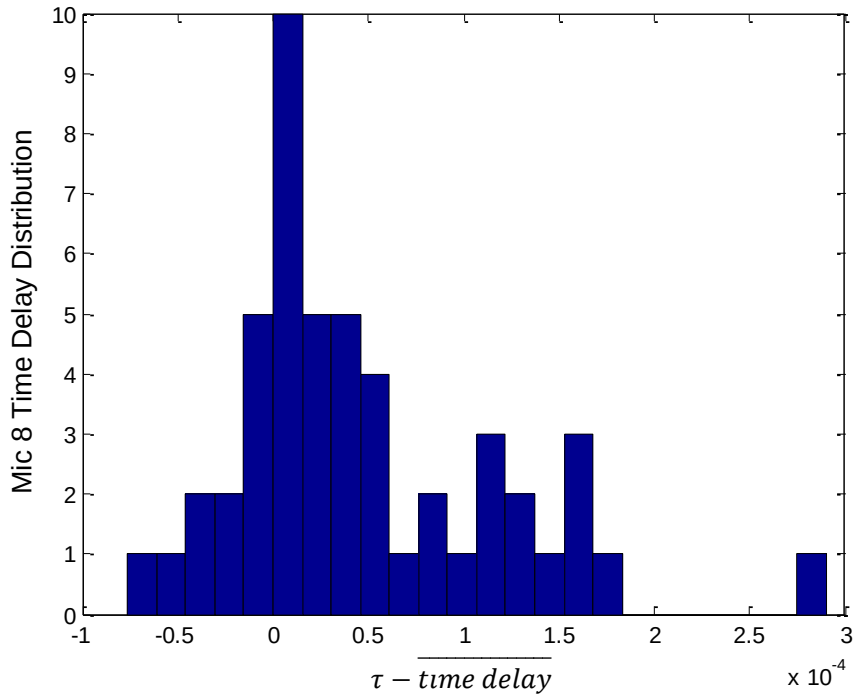

Figure 46: Typical deviation of differences in individual eddy arrival times of microphone 5 and microphone 8 for U=20 m/s and RPM = 4000 over a 4 second interval.

With the time signals representing eddy ingestion events identified and time delay aligned in all the microphone signals, these signals could finally be averaged. A weighted average towards microphones with the highest SNR would benefit the clarity of the average shape, but as the acoustic directivity is dipole-like, the magnitude of the blade passage trace is already effectively cosine weighted. It was found that restricting the averaging only to signals from the in-flow microphones (mics 5 through 8) provided the cleanest time delayed averages. These time delayed average eddy passage signatures are plotted as a function of advance ratio and flow speed in Figure 47. The eddy passage signature flow conditions were chosen to give a large range of advance ratios that smoothly transitioned from lightly braking to heavily thrusting. Advance ratios from the highest RPM 30 m/s condition were matched as closely as possible to the advance ratio for the lowest RPM 20 m/s condition. This was similarly done for the 20 m/s to 10 m/s conditions.

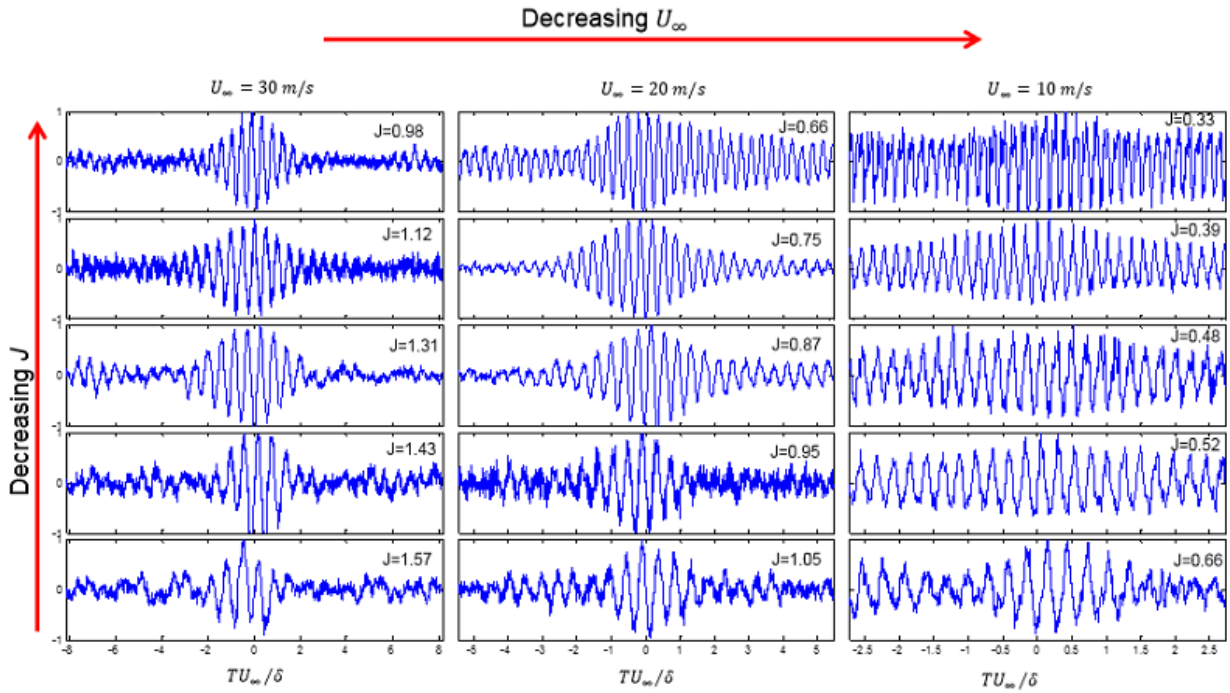

Figure 47: Phase averaged eddy passage acoustic signatures for 30, 20 and 10 m/s at advance ratios of 1.57 to 0.33.

Figure 47 shows eddy passage signatures for J values of 0.33-1.57 and flow speeds of 10-30 m/s. The x-axes show time normalized by multiplying by U_∞/δ. The y-axes show the time delayed average acoustic pressure normalized such that the maximum is 1. The eddy passage signature corresponding to a free steam velocity of 30 m/s and a J value of 0.98 seems to have a Gaussian like decay on its amplitude, shown by a comparison to a cosine wave with a Gaussian window in Figure 48. This perhaps retrospectively validates the choice of the real-valued Morlet wavelet used for the continuous wavelet transform. Note that the left and right of this signature does not go to zero due to random noise. Eddy passage signatures for other conditions, corresponding to J values between 0.95 and 1.4, also display a wavelet-like form and their timewise extent appears roughly constant.

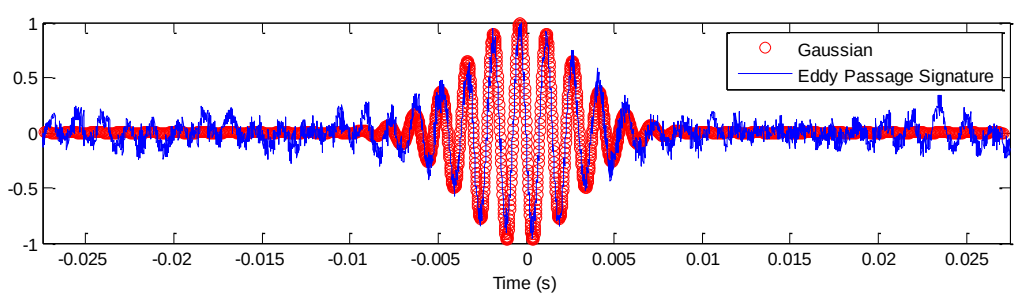

Figure 48: Comparison of a cosine wave with a Gaussian decay to the average eddy passage signature for $U_\infty = 30\ m/s$, $RPM = 4000$, and $J = 0.98$

As J is reduced below 0.95, a tail like structure begins to form on the right side of the eddy passage signature, starting at an advance ratio of 0.87 for a flow speed of 20 m/s. This grows in length as the advance ratio decreases and turns into a large tonal component at an advance ratio of 0.66. Note that this tonal component is not just an increase in streamwise timescale. It extends well past the axes limits in Figure 47, and for J values less than 0.6, the tonal component dominates the entire eddy passage signature. This is confirmed to be tonal from analyzing the coherence of the blade clocking signal with the acoustic signal discussed earlier, as well as from examining Figure 49.

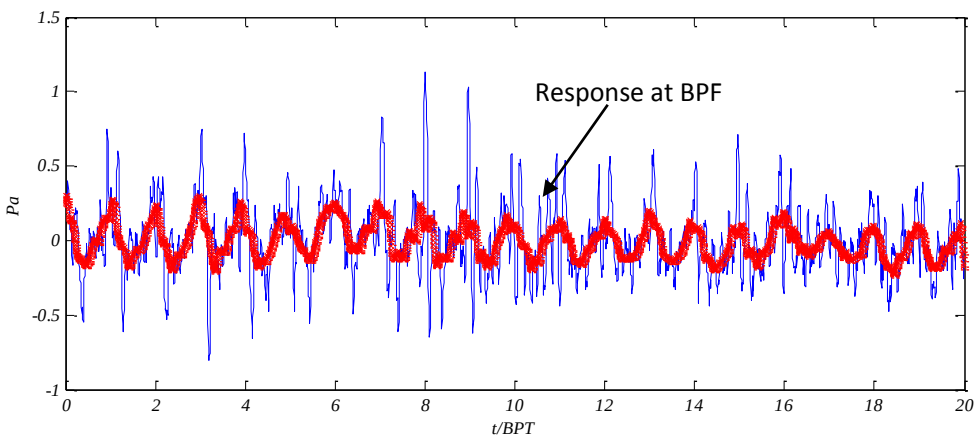

Figure 49: Acoustic pressure time series for $U_\infty = 10\ m/s$, $RPM = 2750$, J = 0.48, showing a dominant signal component at the BPF. (Taken at $\theta_m = 14^o$)

Figure 49 shows the time series for a low advance ratio measurement (10 m/s, 2750 RPM, J = 0.48). Shown on the y-axis is pressure in Pascals, and shown on the x-axis is time normalize on the blade passage time. The x-axis shows fifteen units of time normalized on the blade passage frequency, corresponding to 0.0436 seconds. A smoothed line was fit to the signal using a 20 data point local averaging filter, and is shown in red. It is clear that the majority of the data is dominated by a component at the blade passage frequency. This is caused by both broadband and tonal components. Earlier analysis showed that for an advance ratio of 0.48, the BPF had a 79% tonal component. This differs from the time series in Figure 31 which could distinguish locations of random noise. The signal in Figure 37 has negligible tonal component, which is confirmed by earlier coherence analysis.

The 10 m/s eddy signatures in Figure 47 agree with the trend from the 20 m/s signatures in that a tonal component becomes dominant for advance ratios of about 0.6 and lower. This tonal component may be due to the blade passing through a boundary layer separation region at the wall

at low advance ratios. As stated before, Alexander *et al.* (2014) found that the boundary layer separates from the wall around the blade tips at advance ratios below 0.86. Note that this is where the visible tonal component on the eddy passage signatures started to form. This separation will create a mean flow variation that the rotor will ingest, resulting in tonal noise. As the advance ratio decreases, this effect would increase up to the next eddy passage, which may explain the tonal component on the left side of the eddy passage signature at lower advance ratios.

This switch to a tonal blade passage response from a clear eddy interaction can better be examined by looking in more detail about what physically is occurring in the flow. At the zero thrust condition, eddies in the boundary layer approach the rotor undisturbed, and are cut at the blade passage frequency. This is shown below in Figure 50. Note that the dotted black lines represent the streamtube entering the rotor disk plane.

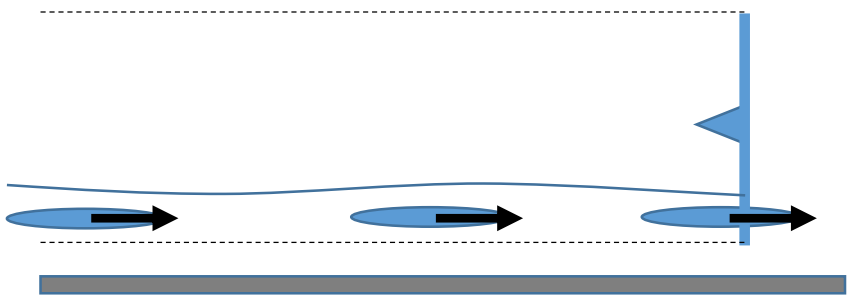

Figure 50: Diagram of turbulence as it is ingested by a non-thrusting rotor

It can be seen in Figure 50 that as an eddy approaches the rotor, a lack of streamtube contraction results in the eddy structures remaining undistorted. They do not increase in velocity as they approach and pass through the rotor disk plane. Alexander *et al.* (2014) obtained tuft flow visualization measurements near the rotor tip gap, and Wisda *et al.* (2015) and Murray *et al.* (2015) obtained tip gap PIV measurements at the zero thrust condition. These are shown below in Figure 51 and Figure 52. In both figures, the flow is moving from left to right, and they are both occurring with an advance ratio of 1.44. The rotor is visible in Figure 51 and two vertical black lines in Figure 52 represent the rotor disk plane location. The *x*-axis on the PIV measurement vector field is *X*' in mm, corresponding to the distance in the streamwise direction away from the rotor disk plane, where –*X*' is upstream of the rotor. The *y*-axis is *Z*' in mm, or the floor normal distance away from the bottom dead center of the rotor tip gap.

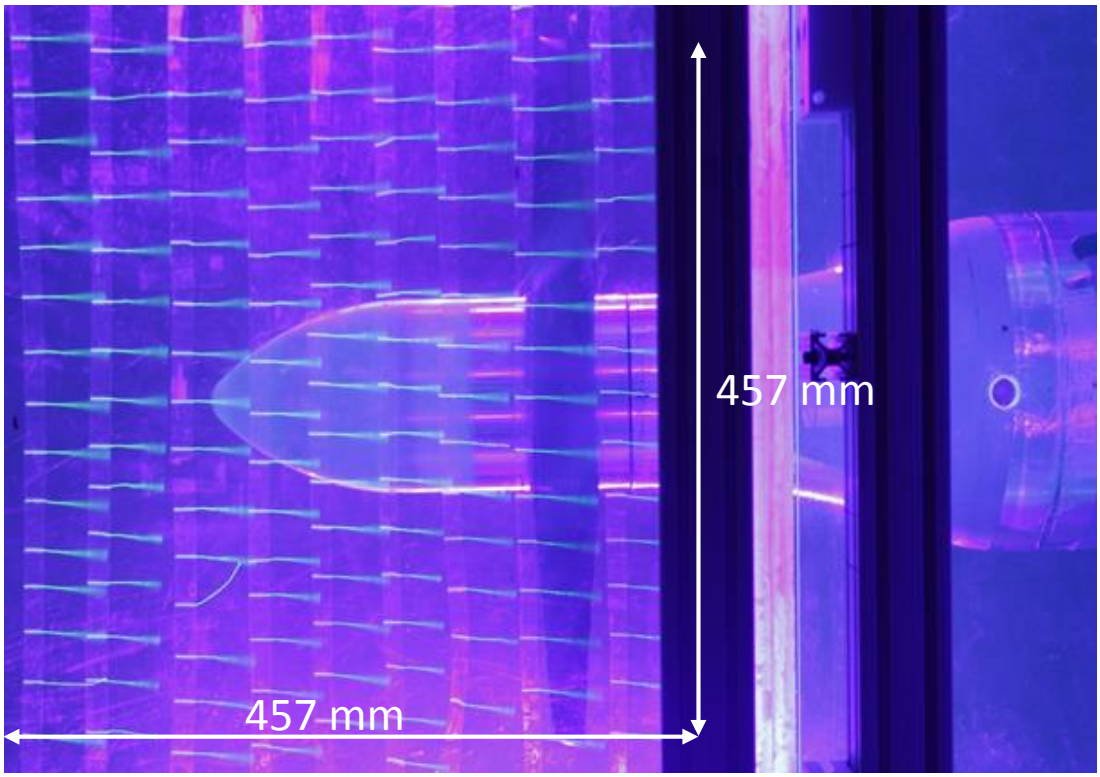

Figure 51: Tuft flow visualization for a 30 *m/s* 2734 RPM, *J*=1.44 condition (Photo taken during study of Alexander *et al.* (2014)). Used with permission of W. Nathan Alexander, 20 AIAA/CEAS Aeroacoustics Conference, 2015. Alexander, W. N., Devenport, W., Wisda, D., Morton, M., and Glegg, S. A. L., "Sound Radiated from a Rotor and Its Relation to Rotating Frame Measurements of Ingested Turbulence", 20 AIAA/CEAS Aeroacoustics Conference, Atlanta, GA, July 16-20, 2014, AIAA-2014-2746.

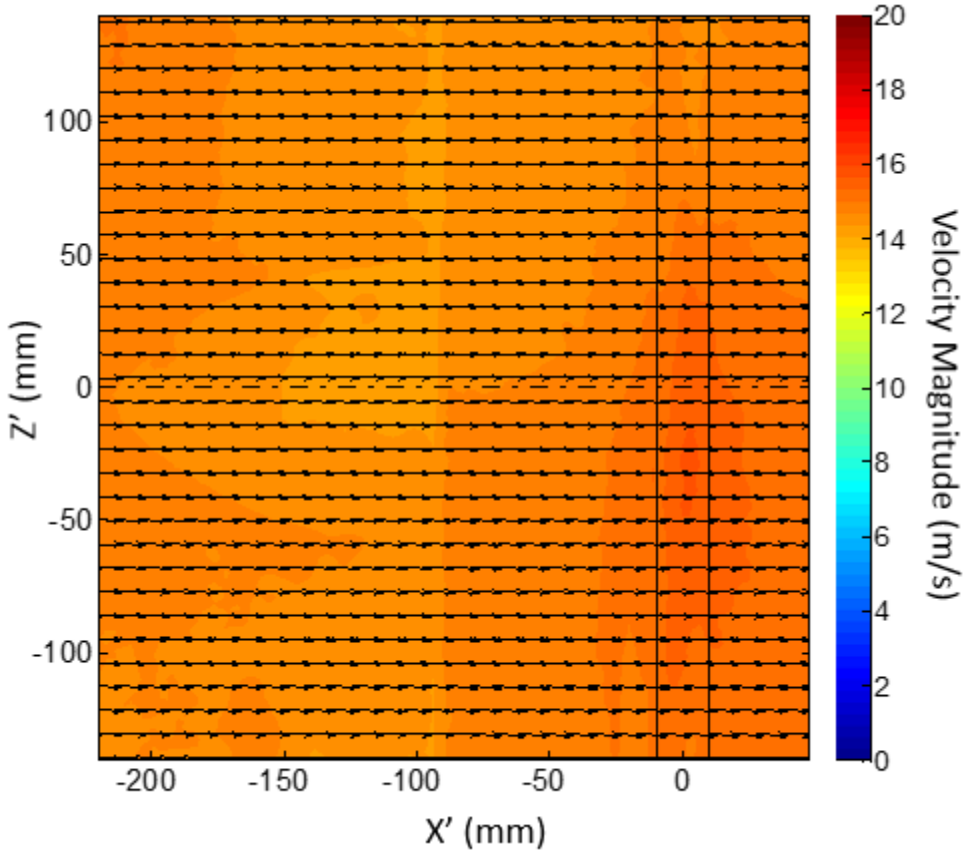

Figure 52: PIV Velocity vector field for a 20 *m/s*, 1823 RPM, *J*=1.44 condition (PIV measurement obtained in studies of Wisda *et al.* (2015) and Murray *et al.* (2015))

The overall lack of distortion is clearly visible in both Figure 51 and Figure 52. The tufts remain horizontal in Figure 51 and the velocity vectors in Figure 52 remain mostly unchanged as they enter the rotor disk plane. The acoustic implication to this is noted in the phased average eddy passage signature. The phased average acoustic signature for the 30 m/s, 2750 RPM, and *J*=1.44 case in Figure 47 is shown below in Figure 53. It is clear that an eddy approaches the rotor, is cut at the blade passage frequency as it passes through.

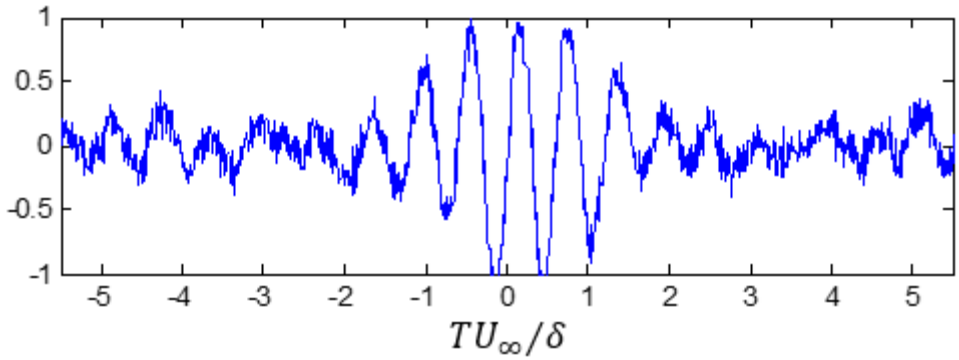

Figure 53: Phased average acoustic signature for a 30 *m/s*, 2734 RPM, *J*=1.44 condition

As the rotor begins to thrust, an upstream streamtube contraction occurs, accelerating the flow towards the rotor face. A diagram of this is shown below in Figure 54. Note that the dotted black lines represent the streamtube contraction.

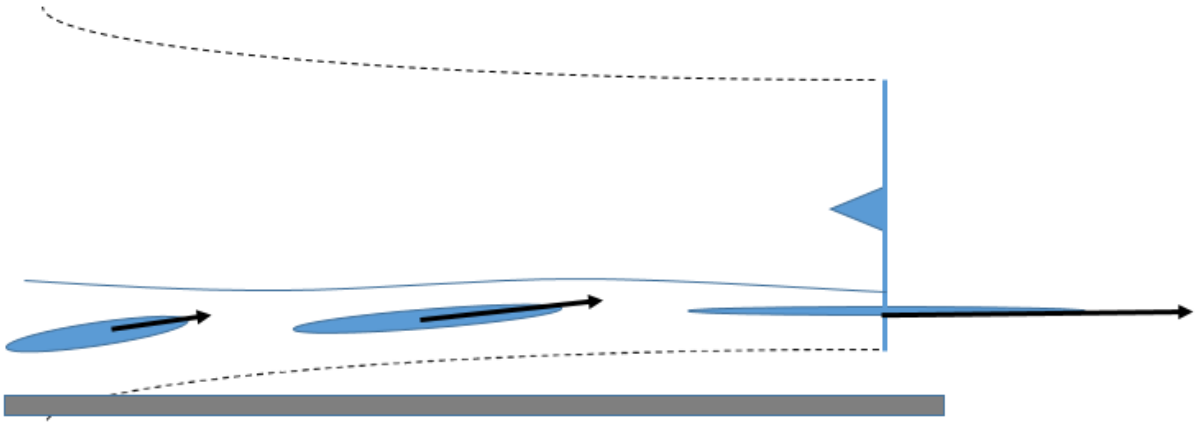

Figure 54: Diagram of turbulence as it is ingested by a lightly thrusting rotor

The eddies shown in Figure 54 are effected by the streamtube contraction, increasing in length and velocity as they pass through the rotor disk plane and are cut at the blade passage frequency. The tuft flow visualization from Alexander *et al.* (2013) for a *J*=1.05 condition is shown below in Figure 55. The tufts are placed roughly in a 457 x 457 mm square, vertically centered on the rotor axis. Also shown below in Figure 56 are tip gap PIV measurements from Wisda *et al.* (2015) at an advance ratio of 1.05.

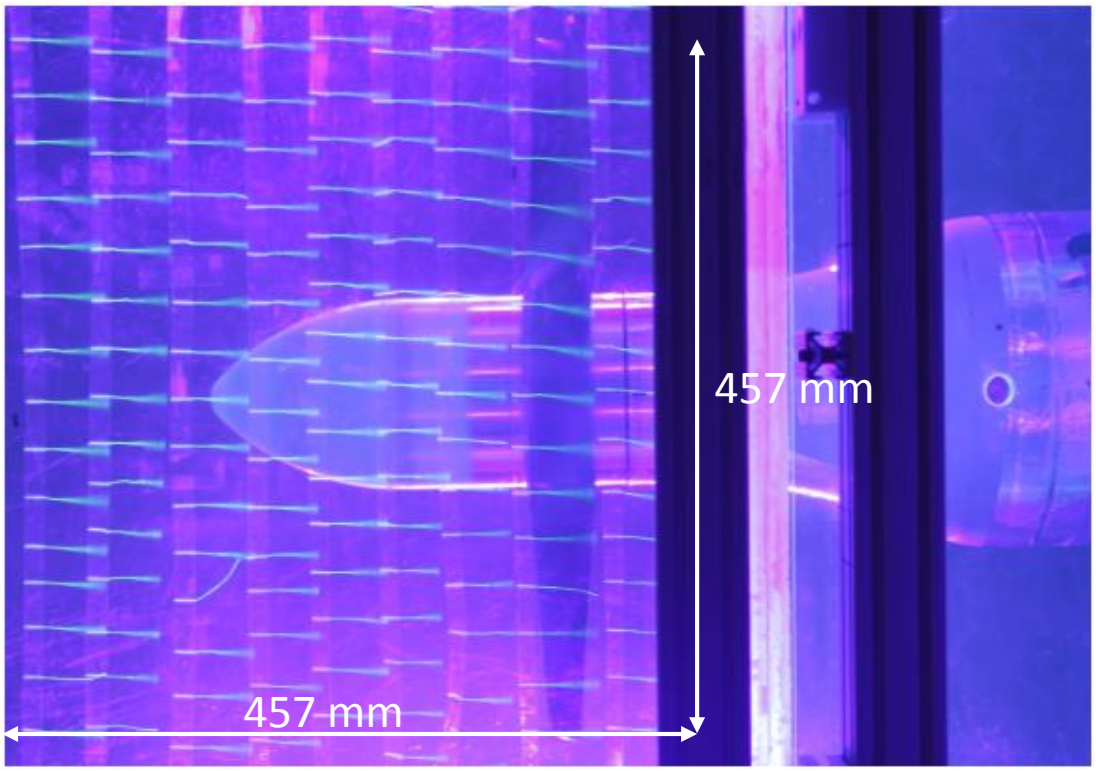

Figure 55: Tuft flow visualization for a 22 *m/s* 2734 RPM, *J*=1.05 condition (Photo taken during study of Alexander *et al.* (2014)). Used with permission of W. Nathan Alexander, 20 AIAA/CEAS Aeroacoustics Conference, 2015. Alexander, W. N., Devenport, W., Wisda, D., Morton, M., and Glegg, S. A. L., "Sound Radiated from a Rotor and Its Relation to Rotating Frame Measurements of Ingested Turbulence", 20 AIAA/CEAS Aeroacoustics Conference, Atlanta, GA, July 16-20, 2014, AIAA-2014-2746.

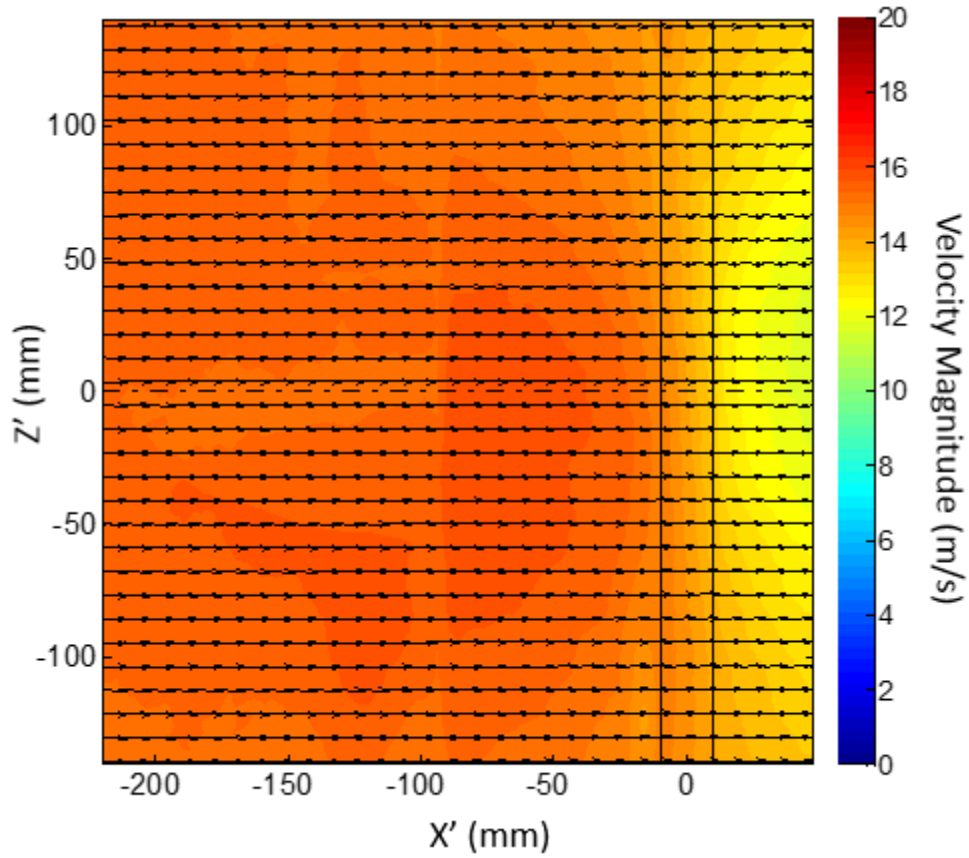

Figure 56: PIV Velocity vector field for a 20 *m/s*, 2500 RPM, *J*=1.05 condition (PIV measurement obtained in studies of Wisda *et al.* (2015) and Murray *et al.* (2015))

Slight distortion is visible in Figure 55 as noted by the upper half of the tufts beginning to face towards the rotor hub. The flow distortion is difficult to see in the PIV measurements in Figure 56, due to the limited window size. However, a clear velocity gradient occurs over the rotor disk plane, indicating that the rotor is interacting with the flow. These PIV measurements are also in the tip gap, and would be unable to view the downstream accelerated flow. Again, the acoustic implication to this can be seen in the phased average eddy passage signature. The phased average acoustic signature for the 20 m/s, 2500 RPM, and *J*=1.05 case in Figure 47 is shown below in Figure 57. It is clear that an eddy approaches the rotor and is cut at the blade passage frequency as it passes through. The similarity between signatures in Figure 57 and Figure 53, indicates that the turbulence interacting with the lightly thrusting rotor increases in velocity close to the same rate at which it is elongated in the streamwise direction.

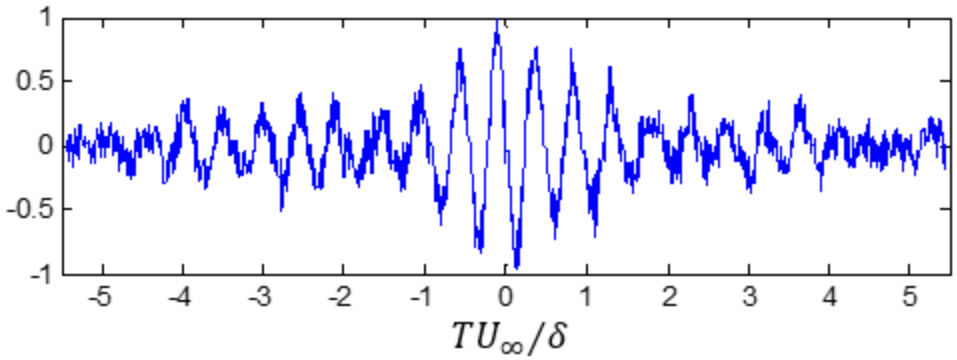

Figure 57: Phased average acoustic signature for a 20 *m/s*, 2500 RPM, J=1.05 condition

As the rotor continues to increase in thrust, or decrease in advance ratio, the upstream streamtube contraction starts to affect a wider area in order to obtain the needed mass flow rate through the rotor disk plane. If the contraction is interrupted by the wall, the rotor becomes starved for fluid and must obtain it from downstream. This results in flow reversal near the blade tip gap, which can push incoming turbulence away towards the hub. This flow reversal can form into a vortex and can interact with the blades. This will result in a tonal blade response as the blades cut through this reversal at the blade passage frequency. A diagram of this is shown below in Figure 58.

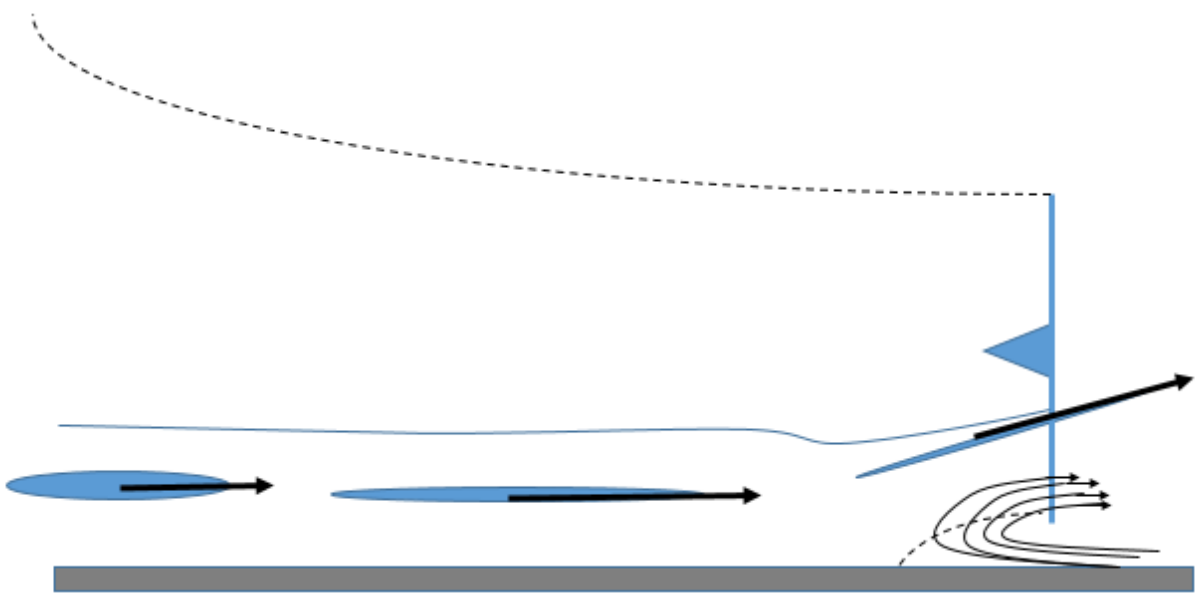

Figure 58: Diagram of turbulence as it is ingested by a heavily thrusting rotor with flow reversal

It can be seen that the eddies are being distorted in the streamwise direction as they move along the streamtube contraction, but the interaction of the rotor with flow reversal in the tip gap becomes an important factor that cannot be ignored. As this flow reversal becomes stronger it can completely overshadow the upstream turbulence interactions. This flow reversal is visible from Alexander *et al.* (2013)'s tuft flow visualization for an advance ratio of 0.58 below in Figure 59. Also shown below in Figure 60 are tip gap PIV measurements from Wisda *et al.* (2015) at an advance ratio of 0.58.

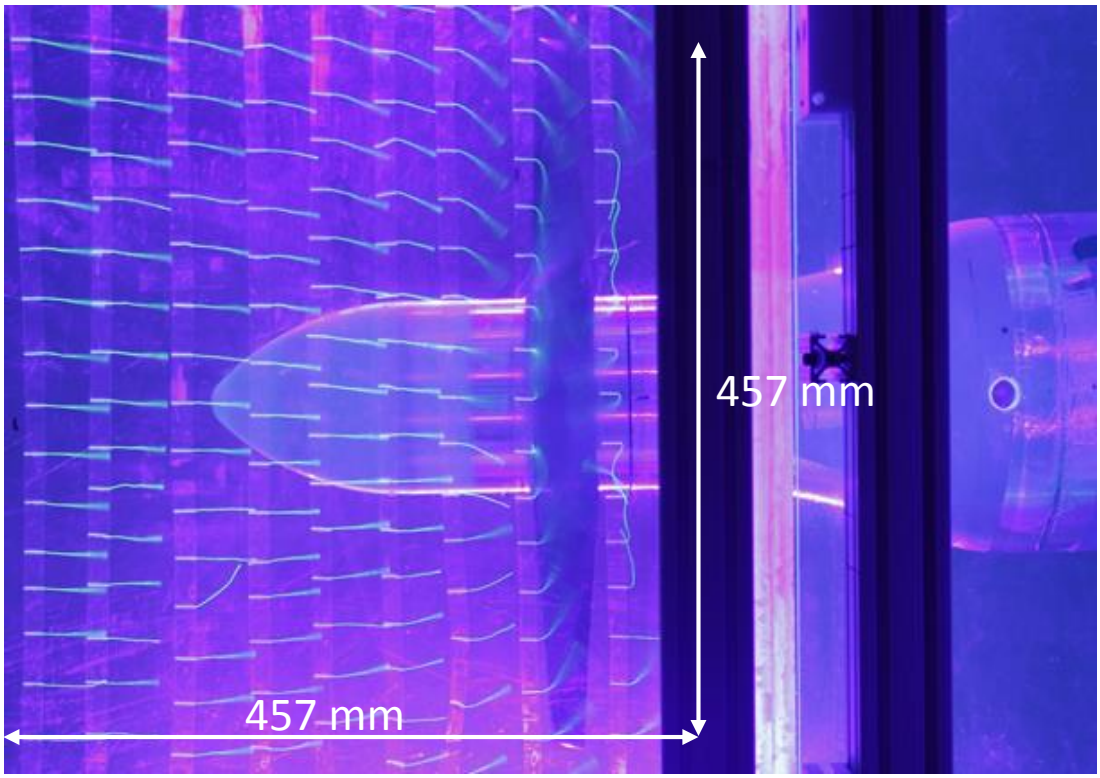

Figure 59: Tuft flow visualization for a 12 *m/s* 2734 RPM, *J*=0.58 condition (Photo taken during study of Alexander *et al.* (2014)). Used with permission of W. Nathan Alexander, 20 AIAA/CEAS Aeroacoustics Conference, 2015. Alexander, W. N., Devenport, W., Wisda, D., Morton, M., and Glegg, S. A. L., "Sound Radiated from a Rotor and Its Relation to Rotating Frame Measurements of Ingested Turbulence", 20 AIAA/CEAS Aeroacoustics Conference, Atlanta, GA, July 16-20, 2014, AIAA-2014-2746.

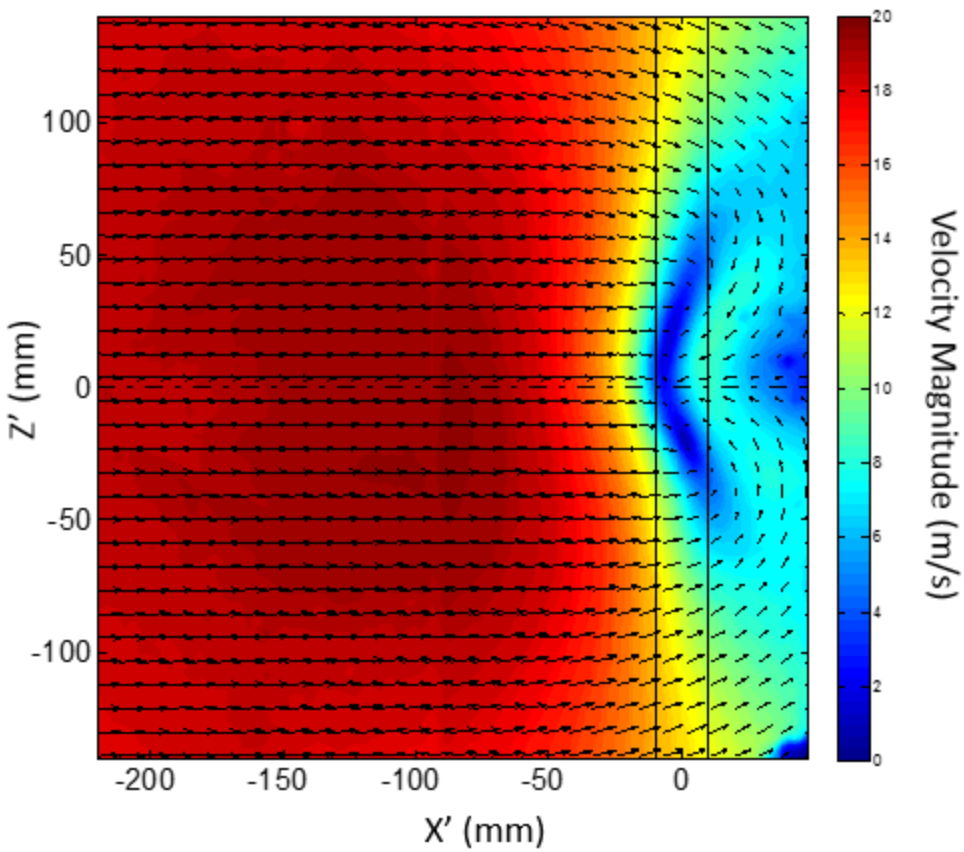

Figure 60: PIV Velocity vector field for a 20 *m/s*, 4500 RPM, *J*=0.58 condition (PIV measurement obtained in studies of Wisda *et al.* (2015) and Murray *et al.* (2015))

The distortion is distinctly visible in Figure 59 as noted by all of the upstream tufts turning to face the rotor hub. A distinct double vortex flow reversal patter is also visible near the rotor plane. The flow distortion is also easily visible in the PIV vector field in Figure 60. The upstream mean flow at 10 mm from the wall has accelerated from 14 m/s to 20 m/s, and the vectors turn towards the rotor axis near the rotor disk plane. A double vortex flow reversal pattern is also visible in the vector field. This flow reversal is also seen in RANS predictions from Glegg *et al.* (2015). They were able to make velocity field predictions at not only the tip gap, but also in the rotor disk plane. They found that the double vortex structure narrowed as the measurement plane moved away from the wall, indicating that the double vortex shown in Figure 60 is just a slice of an arch vortex. This arch vortex is shown below in Figure 61. The rotor interaction with this reversed flow will create a tonal response which is visible in the phase averaged acoustic signature in Figure 62 below.

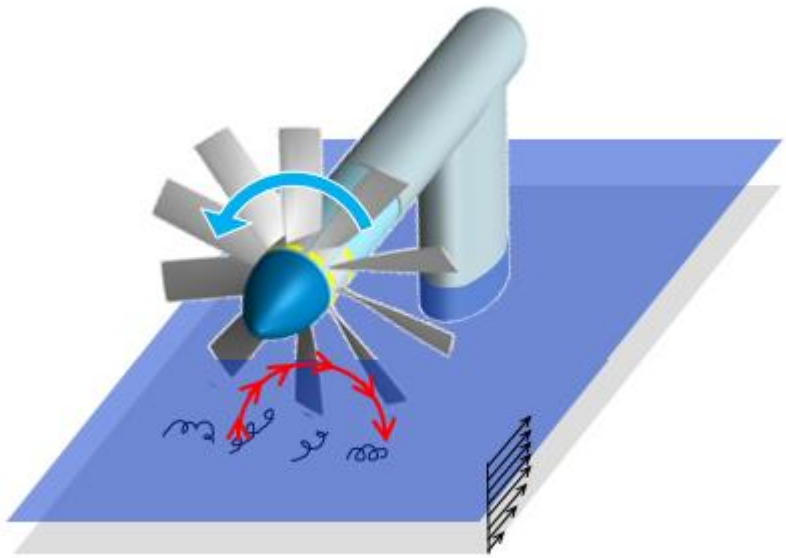

Figure 61: Diagram of arch vortex flow reversal found in Glegg, S., Bruono, A., Grant, J., Lachowski, F., Devenport, W., " Sound Radiation from a Rotor Partially Immersed in a Turbulent Boundary Layer." *to be presented at the 21st AIAA/CEAS Aeroacoustics meeting in Dallas, Texas June 22-26, 2015.* Used under fair use, 2015

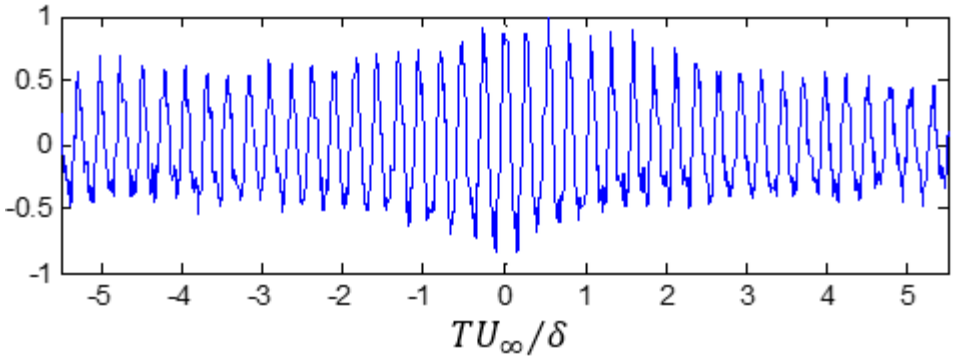

Figure 62: Phased average acoustic signature for a 20 *m/s*, 4500 RPM, *J*=0.58 condition

Figure 62 shows a distinctly tonal response at the blade passage frequency. Because each blade is interacting with the flow reversal as it passes through the boundary layer, each blade response will be in phase with each other, creating a coherent response. This is different from haystacking noise, which is due to stochastic eddies are cut by the rotor blades. While blade to blade responses for an individual eddy are correlated, cuts between different eddies are not,

creating wide spectral lumps at the blade passage frequency and its harmonics. This flow reversal interaction however, is correlated across the entire measurement, resulting in a narrowband response at the blade passage frequency and its harmonics.

3.3.3 Determination of average eddy scales

Characteristic eddy time scales were estimated directly from the eddy passage signatures. A Gaussian weighted cosine wave was fit to each signature using a least square's method. This was shown previously in Figure 48. The full width at half amplitude was computed for each Gaussian to be representative of the streamwise timescales. The timescales were normalized by multiplying the eddy passage time by the free stream velocity and dividing by the boundary layer thickness. The timescales are shown for varying advance ratios and flow speeds in Figure 63. No eddy passage signatures with significant tonal components were used in this analysis because the length scales would be on the order of the measurement time. Timescales obtained in this study are represented as solid dots. Timescales obtained from Alexander *et al*. (2013) are represented as circles. From Figure 63, it can be seen that the normalized timescales are fairly constant at around $TU_\infty/\delta = 2.5$ and seem to increase slightly with increasing RPM at a given free stream velocity. This means that at a given free stream velocity as thrust is increased, the eddies are stretched at a slightly higher rate than their increase in velocity.

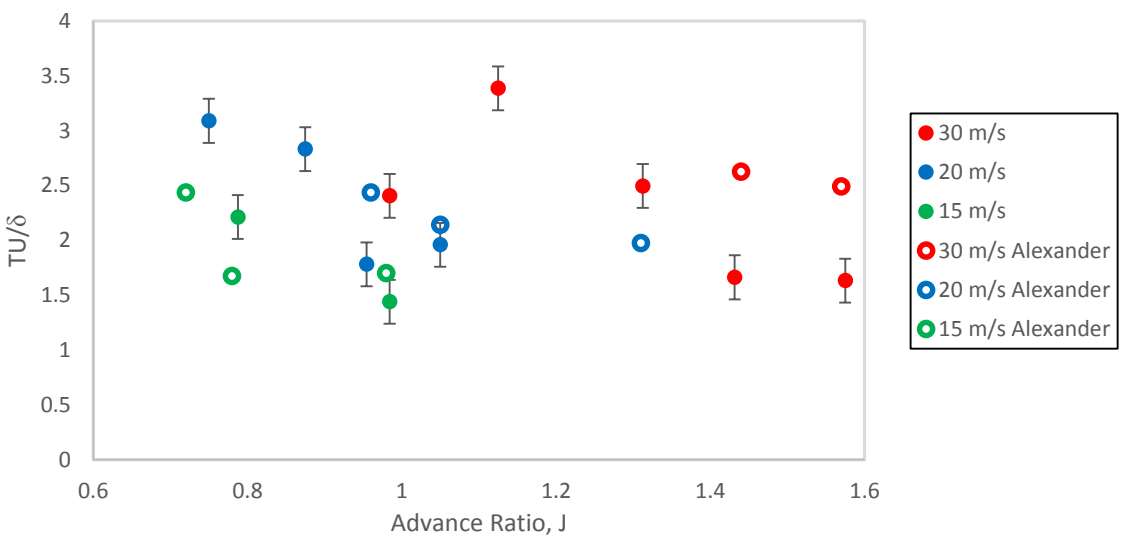

Figure 63: Streamwise scales obtained directly from average eddy passage signatures for varying advance ratios and free stream velocities, compared to scales obtained in Alexander *et al*. (2013) Used with permission of W. Nathan Alexander, 19th AIAA/CEAS Aeroacoustics Conference, 2015. Alexander, W. N., Devenport, W., Morton, M. A., and Glegg, S. A. L., "Noise from a Rotor Ingesting a Planar Turbulent Boundary Layer", 19 AIAA/CEAS Aeroacoustics Conference, May 27-29, 2013, Berlin, DE, AIAA-2013-2285.

An error bound for the streamwise scales was determined to account for the uncertainty in the discrimination level. While the elasticity plots in the discrimination level analysis show a distinct discrimination level, the actual shelf point location is not easy to identify. Also, depending on how the elasticity was computed itself, the peak can vary to an adjacent tested discrimination level. This creates an uncertainty of about 10% in the discrimination level. The discrimination level was varied by ± 10% and lengthscales were obtained for the new average acoustic signatures. The standard deviation of these lengthscales is roughly $\sigma(TU_\infty/\delta)$=0.1. The error bound was estimated by 2 standard deviations or TU_∞/δ=0.2.

These lengthscales are similar to those found in Alexander *et al*. (2013). Alexander *et al*. (2013) also found streamwise lengthscales to increase with increasing RPM for a set flow speed. However, Alexander *et al.* also noted an overall increase in lengthscale with increasing free stream flow speed that was not found in this study's analysis. This may be due to the nature of the methods used to obtain lengthscales. This study obtains a blade passage response from a time-frequency approach and uses a discrimination level type analysis to determine a significant eddy. No such assumptions were used in Alexander *et al*., who obtained lengthscales from auto-correlating the blade passage response. Alexander *et al.* did not omit any eddies that would have been ignored due to a reduction in their far field response or size.

4 CONCLUSIONS

Data obtained from measurements in the studies of Alexander *et al.* (2013 and 2014) have been further analyzed to study rotor turbulence interactions from a rotor immersed in a fully turbulent, two-dimensional boundary layer. On-blade hotwire measurements were used to analyze the extent the inflow distortion effected the rotor disk angle of attack distribution. In addition, far field acoustic data was used to determine rotor RPM and inflow speed effects, as well measure rotor's acoustic directivity. An objective approach was also developed that detected eddy passages through the rotor plane in the acoustic signal. This was used to determine the average acoustic response to an eddy passage.

The angle of attack distribution of the 2.25 scale Sevik rotor used for this project has been calculated with undistorted flow theory and accounting for the nonhomogeneous boundary layer. It was found that a sharp increase in angle of attack occurs as the rotor blades enter the boundary layer, and was also found that this can cause local thrusting to occur in the rotor plane, resulting in the potential for flow distortion in a zero thrust configuration. These angle of attack distributions were compared with measured angles of attack from on blade hotwire data. They were found to have strong qualitative agreement, with a constant offset in the rotational direction due to flow acceleration. Interestingly, it was found that the distortion effects on the angle of attack distribution were more pronounced away from the rotor tips. Asymmetry was also noted in the angle of attack distribution towards the downstroke side of the boundary layer-rotor interaction region, agreeing with unsteady upwash measurements from Alexander *et al.* (2014). This is hypothesized to be due to the interaction with a leading blade's flow field that was caused by it cutting through the boundary layer. It was also found that for low enough advance ratios, the blade tips see a sharp increase in angle of attack as they approach the wall that is narrower than the angle of attack increase associated with boundary layer interactions. This narrow response is due to the blades interacting with a region of flow that has a much lower streamwise velocity component. This is indicative of interactions with flow reversal in the blade tip gap known as the "Pirouette Effect."

The noise from a rotor ingesting a planar turbulent boundary layer has been documented over a large range of operating advance ratios. Distinct features were observed in the spectra at different advance ratios. At higher advance ratios near zero-thrust, vortex shedding was observed. Below $J = 0.9$, the shedding noise was absent. The right skewing of the haystacks at low-thrust was also observed and attributed to the preferential cutting of coherent structures turned so as to be more perpendicular to the rotor path. As the advance ratio was lowered, an increased number of haystacks were observed. These haystacks became narrower and more symmetric about the BPF. Because the broadband nature of the haystacks is attributed to the stochastic interaction of

eddies with the rotor, a narrowing of the haystacks indicates that the interaction is becoming more correlated between eddies, and that the acoustic response should be tonal.

Both angle of attack and acoustic analysis has found evidence of rotor interactions with flow reversal. These interactions will create a highly correlated blade response across the entire measurement. To determine what conditions result in this interaction, the coherence of the blade clocking and far field acoustic signals were taken. Sato (1986) had previously characterized where flow reversal will occur as a function of a thrust parameter. Sato predicted that for the tip gap used in this study, flow reversal will occur for thrust parameters greater than two. This flow reversal region roughly corresponds to advance ratios less than 0.8. When the operating conditions in this study were converted to Sato's thrust parameter, the coherence at the blade passage frequency was negligible when less than two, and quickly increased up to 79% afterwards, indicating a strong tonal response at the blade passage frequency.

A method of detecting eddy passages from the acoustic signal was also developed using the continuous wavelet transform. By time delay aligning the acoustic signatures from multiple microphones, time delayed average eddy passage acoustic signatures were determined for a range of advance ratios. It was found that for advance ratios between 0.75 and 1.5, the eddy passage signatures are of the form of a Gaussian weighted sinusoid. It was also found that a tonal component was dominant for lower advance ratios. This tonal component is due the rotor ingesting mean flow variations created by boundary layer separation at low advance ratios. It was found that tonal acoustic signatures corresponded to rotor parameters predicted by Sato (1986) to have flow reversal in the blade tip gap. It was also found that these tonal signatures corresponded to conditions where flow reversal was directly shown by tuft flow visualization and PIV measurements. This separation or flow reversal is again, evident of the "Pirouette Effect". The rotor blades cut through a vortex caused by flow reversal, resulting in a highly tonal blade response.

Lengthscales obtained from the average acoustic signatures reveal normalized streamwise scales of roughly TU_∞/δ=2.5. For set freestream velocities, it was found that lengthscales slightly increased with increasing rotor RPM. This implies that as the thrust is increased, the turbulence is stretched at a slightly higher rate than it is increasing in velocity. This trend, however was not as clear as shown previously in Alexander *et al.* (2013). This is due to the nature of a discrimination type analysis effectively ignoring certain eddy passages that did not meet the discrimination criteria.

Both measured angle of attack distributions and acoustic measurements indicate rotor interactions with flow reversal for low advance ratios. When the normal streamtube contraction upstream of the rotor is interrupted by the wall, the rotor becomes stalled for air and must obtain the needed fluid from downstream, resulting in flow reversal in the blade tip gap. The direct implication of this is shown in a drastic increase in the angle of attack seen by the rotor blade tips near the wall. This increase in angle of attack will fluctuate at the blade passage frequency, causing

a tonal response that can dominate the normal blade interactions with turbulent eddies in the boundary layer. The acoustic response to this is a narrowing of haystacks, and an increased number of visible haystacks at blade passage frequency harmonics. The average acoustic response reveals that this causes a tonal response, as opposed to a Gaussian weighted sinusoidal response indicative of upstream turbulent eddy interaction.

REFERENCES

Alexander, W. N., Devenport, W., Morton, M. A., and Glegg, S. A. L., "Noise from a Rotor Ingesting a Planar Turbulent Boundary Layer", 19 AIAA/CEAS Aeroacoustics Conference, May 27-29, 2013, Berlin, DE, AIAA-2013-2285.

Alexander, W. N., Devenport, W., Wisda, D., Morton, M., and Glegg, S. A. L., "Sound Radiated from a Rotor and Its Relation to Rotating Frame Measurements of Ingested Turbulence", 20 AIAA/CEAS Aeroacoustics Conference, Atlanta, GA, July 16-20, 2014, AIAA-2014-2746.

Amiet, R.K., 1978, "Refraction of Sound by a Shear Layer" *Journal of Sound and Vibration*, vol. 58, Issue 4, pp. 467-482

Blake, W. *Mechanics of Flow Induced Sound and Vibration.* Academic Press, New York, 1986.

Carlton, J. (2007). Marine Propellers and Propulsion. 2nd ed.

Catlett M R, Anderson, J M, and Stewart D O, "Aeroacoustic Response of Propellers to Sheared Turbulent Inflows", 18th AIAA/CEAS Aeroacoustics Conference, Colorado Springs, CO, June 4-6, 2012, AIAA-2012-2137.

Glegg, S., and N. Walker. "Fan Noise from Blades Moving Through Boundary Layer Turbulence." *5th AIAA/CEAS Aeroacoustics Conference.* Bellevue, WA, 1999.

Glegg, S., Morton, M., and Devenport, W., "Rotor Inflow Noise Caused by a Boundary Layer: Theory and Examples", 18th AIAA/CEAS Aeroacoustics Conference, Colorado Springs, CO, June 4-6, 2012, AIAA-2012-2263.

Glegg, S A L, Kawashima, E, Lachowski, F, Devenport, W, and Alexander, N, "Inflow Distortion Noise in a Non Axisymmetric Flow", 19th AIAA/CEAS Aeroacoustics Conference, Berlin, DE, May 27-29, 2013.

Glegg, S., Bruono, A., Grant, J., Lachowski, F., Devenport, W., " Sound Radiation from a Rotor Partially Immersed in a Turbulent Boundary Layer." *to be presented at the 21st AIAA/CEAS Aeroacoustics meeting in Dallas, Texas June 22-26, 2015.*

Hanson, D. "Spectrum of Rotor Noise Caused by Atmospheric Turbulence." *Journal of the Acoustical Society of America*, 1974: 110-126.

Hersh, A S, Soderman, P T, and Hayden R E, 1974, "Investigation of Acoustic Effects of Leading-Edge Serrations on Airfoils", *Journal of Aircraft*, vol. 11(4), pp. 197-202.

Hess, Peter. *Using Mathematics In Economic Analysis*. Upper Saddle River: Prentice Hall, 2002. Print.

Huse. (1971) ‘Propeller-Hull Vortex Cavitations’. Norw. Ship Model Exp. Tank Publ. 106, May 1971.

Majumdar, S., and N. Peake. "Noise Generation by the Interaction Between Ingested Turbulence and a Rotating Fan." *Journal of Fluid Mechanics*, 1998: 181-216.

Martinez, R. "Broadband Sources of Structure-Borne Noise for Propulsors in "Haystacked" Turbulence." *Computers and Structures*, 1997: 475-490.

Martio, J., Sipila, T., Sachez-Caja, A., Saisto, I., Siikonen, T., 2011, “Evaluation of the Propeller Hull Vortex Using a RANS Solver,” Second International Symposium on Marine Propulsors smp’11, Hamburg, Germany, June 2011

Murray, H., Wisda, D., Alexander, W., Nelson, M., Devenport, W., Glegg, S., ”Sound and Distortion Produced by a Braking Rotor Operating in a Planar Boundary Layer; with Application to Wind Turbines” *to be presented at the 21st AIAA/CEAS Aeroacoustics meeting in Dallas, Texas June 22-26, 2015.*

Meyers, T., Alexander, W. N., Devenport, W., and Glegg, S. A. L., “High Reynolds Number Turbulent Boundary Layer Flow over Rough Walls: Wall Pressure Spectrum and Noise”, 19th AIAA/CEAS Aeroacoustics Conference, Berlin, DE, May 2013, AIAA-2013-2249.

Morton, M A, 2012, “Rotor Inflow Noise Caused by a Boundary Layer: Inflow Measurements and Noise Predictions”, Master’s Thesis, AOE Department, Virginia Tech, Avail: http://scholar.lib.vt.edu/theses/available/etd-08102012-103032/.

Paterson, R W, Vogt, P G, Fink, M R, and Munch C L, 1973, “Vortex Noise of Isolated Airfoils”, *Journal of Aircraft*, vol. 10(5), pp. 296-302.

Remillieux, M., Crede, E., Camargo, H., Burdisso, R., Devenport, W., Rasnick, M., Van Seeters, P., and Chou, A.,“Calibration and Demonstration of the New Virginia Tech Anechoic Wind Tunnel”, 14th AIAA CEAS Aeroacoustics Conference, Vancouver, Canada, May 2008

Sato, R., Tasaki, R., and Nishiyama, S., 1986. ‘Observation of Flow on a Horizontal Flat Plate above a Working Propeller and Physics of Propeller-Hull Vortex Cavitation’. Proceed. Internat. Symposium on Propeller and Cavitation, Wuxi, China.

Sevik, M, “Sound Radiation from a Subsonic Rotor Subjected to Turbulence”, 1971, NASA SP 304.

Stephens, D., and C. Morris, 2009, "Sound Generation by a Rotor Interacting with a Casing Turbulent Boundary Layer." *AIAA Journal*, vol. 47, pp. 2698-2708.

Wisda, D., Murray, H., Alexander, W., Nelson, M., Devenport, W., Glegg, S., .”Flow Distortion and Noise Produced by a Thrusting Rotor Ingesting a Planar Turbulent Boundary Layer” *to be presented at the 21st AIAA/CEAS Aeroacoustics meeting in Dallas, Texas June 22-26, 2015.*